Copper Ion-Based Electron Spin Resonance Spectroscopic Rulers

by

Zhongyu Yang

B.E., University of Science and Technology of China, CHINA, 2004

Submitted to the Graduate Faculty of

School of Arts and Sciences in partial fulfillment

of the requirements for the degree of

Doctor of Philosophy

University of Pittsburgh

2010

UNIVERSITY OF PITTSBURGH

FACULTY OF ARTS AND SCIENCES

This dissertation was presented

by

Zhongyu Yang

It was defended on

May 18th, 2010

and approved by

David Waldeck, PhD., Professor, Department of Chemistry, Faculty of Arts and Sciences

David Pratt, PhD., Professor, Department of Chemistry, Faculty of Arts and Sciences

Angela Gronenborn, PhD., Professor, Department of Structural Biology, School of Medicine

Dissertation Advisor: Sunil Saxena, PhD., Associate Professor, Department of Chemistry, Faculty of Arts and Sciences

Copper Ion-Based Electron Spin Resonance Spectroscopic Rulers

Zhongyu Yang, PhD

University of Pittsburgh, 2010

This thesis describes the extension of the double electron electron resonance (DEER) technique to the case of Cu^{2+} and its application in biophysics. First, we demonstrate the possibility of Cu^{2+}–Cu^{2+} distance measurement using DEER on a proline-based peptide. The DEER spectra collected at four different magnetic fields do not change appreciably with magnetic field at X-band. Based on simulations, we show that the orientational effects are important in data analysis and that the proper Cu^{2+}-based DEER experimental procedure is to collect DEER data at many magnetic fields.

Next, we examine the cause of the weak field-dependence of Cu^{2+} DEER data at X-band. We improve the simulation procedure by including a distribution in relative orientation of the g-tensors of the two spins. The new model is tested on two polypeptides. Subtle but detectable orientational effects are observed from DEER spectra of both peptides. Distances obained from DEER are consistent with structural models and with earlier measurements. Constraints on the relative orientation between paramagnetic centers in these two polypeptides are determined by examinations of orientational effects and simulations. We discover that the orientational selectivity is effectively reduced when the relative orientations of the two spin g-tensors display a flexibility of ~5-10°.

We apply the methodology to the case of the EcoRI-DNA complex. Electron Spin Echo Envelope Modulation (ESEEM) experiments show that Cu^{2+} is coordinated to one of the five

histidine residues in EcoRI. Cu^{2+}-based distance constraints are then measured using DEER to reveal this histidine. Using a triangulation procedure based on the measurement of distance constraints we show that Cu^{2+} binds to histidine 114 in EcoRI. The data is novel because it reveals a second metal ion binding site in EcoRI, which has traditionally been classified as a one-metal endonuclease.

TABLE OF CONTENTS

LIST OF TABLES

LIST OF FIGURES

PREFACE

This thesis is dedicated to the people who have supported me in achieving one major goal of my life. First, I thank my research advisor, Professor Sunil Saxena. He directed me into a new world, electron spin resonance. He supported me throughout my thesis with his patience and knowledge. He taught me magnetic resonance spectroscopy and basic biophysics. He trained me in scientific thinking, efficient communication and leadership. He is a great scientist and a wonderful mentor. The best way I can think of thanking him is to succeed in the future and to make him proud of me.

I thank Professor David Waldeck, Professor David Pratt, and Professor Angela Gronenborn for being my dissertation committee. I am deeply grateful for their time and advice for my thesis. I want to thank Professor David Waldeck and Professor David Pratt for being my comprehensive exam committee. I really appreciate their help. I also thank Professor Megan Spence for all her help in my research proposal. She provided excellent suggestions in the experimental design of my proposal and went over my proposal with me many times to make it perfect. I thank Professor Adrian Michael and Professor Rena Robinson for being my proposal committee. Their time and advice was greatly appreciated.

In my daily work I have been blessed with a talented and cheerful group of friends. Dr. Katherine Stone walked me through the beginning stage in the Saxena group. She trained me in spectroscopy and molecular biology techniques, and taught me communication skills. I am

appreciative for everything she has done. Dr. Soraya Pornsuwan trained me in basic ESR theory and matlab programming techniques. She is the one who solved many of my problems on the spectrometer. Dr. Sangmi Jun trained me as well with the other senior graduate students and shared with me her experience in science as well as in life. She is the one who always encouraged me during hard times. I thank Dr. Sharon Ruthstein for all of her patient help in trouble shooting my theoretical and experimental problems and teaching me basic ESR theory. It is really an honor and a joy to work with Jessica Sarver and Byong-kyu Shin, two smart and hard working fellows. Jessica helped me correct my English, shared with me her delicious food, funny stories and her coffee. Most incredibly, she helped me fit into the American life. I really appreciate everything she has done. Byong-kyu is one of a kind. I really enjoyed our discussions in science as well as in general because they were educative to me. Ming Ji and I worked on the same projects for ~ 3 years (cf. Chapter 4 and 5). He is a talented graduate student, a very hard worker and a wonderful friend. Drew Kise is a very talented undergraduate student who worked with me on another project. He helped me perform numerous simulations which are all included in the published JPCB paper (cf. Chapter 3). I also want to thank the new group members, Ishara Silva, Tim Cunningham and Gayathri Rajapakse. It was very pleasant working with all of you.

I thank the technical support from the chemistry machine shop and electronic shop. I also want to thank the chemistry main office for all their help in making things easier for my thesis.

Finally, I thank my parents, my brother and my wife. For the past six years mostly I was separated from them but I can truly feel their support, patience and encouragement. I appreciate everything they did to make this thesis complete.

1.0 INTRODUCTION

Double electron electron resonance (DEER) is a pulsed electron spin resonance (ESR) technique that measures the magnetic dipolar interaction between paramagnetic centers (*1, 2*). The dipolar interaction is proportional to $1/r^3$, where r is the distance between paramagnetic centers. Therefore, the DEER technique provides sensitivity to distances. The most commonly employed paramagnetic center is the nitroxide spin label, which can be site-selectively attached to a protein by using site-directed spin-labeling (SDSL), a method invented by Hubbell and coworkers (*3, 4*). The spin label-to-spin label distance distributions can be precisely extracted from DEER signal by using an established data analysis procedure (*5, 6*). Using this approach, structural information on soluble protein structure and dynamics (*7-20*), DNA and RNA (*21-26*), oligomers (*27-34*) and even more complicated systems such as membrane proteins (*35-47*) and protein-protein/protein-DNA complexes (*12, 48, 49*) has been determined.

Recently, the paramagnetic center has been extended to metal ions and metal-ion clusters, with the motivation of determining structural constraints in metalloproteins (*7, 8, 50-57*). These measurements are challenging, however, due to the large g and hyperfine anisotropies of the paramagnetic metal ions and the complication to the data analysis procedure caused by the selective excitation of the ESR spectrum by microwave pulses. We overcome these challenges in this thesis. Specifically, in Chapter 2, we demonstrate the use of metal ions as the paramagnetic centers and analyze the role of orientational selectivity in Cu^{2+}–Cu^{2+} distance measurements. In

Chapter 3, we reveal the role of the relative orientation distribution in Cu^{2+}-based DEER measurements and develop a general data analysis procedure that is applicable to a general metal ion-system. In Chapter 4, we summarize the optimal experimental conditions to enable efficient Cu^{2+}-based DEER measurements. Furthermore, in Chapter 5, we apply the Cu^{2+}-based distance measurements to the restriction endonuclease EcoRI-DNA complex in order to understand the role of metal ions in the catalysis of the DNA cleavage. The following sections provide a general background of the theoretical and experimental methods that have been used in this thesis.

1.1 SITE-DIRECTED SPIN LABELING

The site-directed spin labeling technique was invented by Hubbell and coworkers in the 1990's (*4*, *58-60*), and has become a common approach to attach unpaired electron(s) to proteins, nucleic acids and macromolecules. Figure 1-1 shows the scheme of spin labeling. (1-oxyl-2,2,5,5,-tetramethylpyrroline-3-methyl)-methanethiosulfonate (MTSSL), which is often used as a spin label, contains an unpaired electron that is delocalized on the N-O bond. The MTSSL can react with a solvent-accessible cysteine residue of a protein, by forming a stable disulfide bond (cf. Figure 1-1). The MTSSL molecule is stable in solution and generally causes minimal perturbation to the structure of a protein, as proved by studies on rhodopsin (*61*), colicin (*62*), and bacteriorhodopsin (*63*). The natural occurrence of free cysteine residues in proteins, however, is relatively low. Therefore, if there is no free cysteine in a protein, or if the free cysteine of a protein is not at the desired site, one can replace a native amino acid with a cysteine residue, by using site-directed mutagenesis. The undesired, native free cysteine is often mutated

to a different residue. As demonstrated in T4 lysozyme (*64*) and colicin (*65*), site-specifically generated cysteine mutants cause little effect on the structure of the protein.

Electron Spin Resonance data on singly spin labeled proteins provides site-specific information on the reorientational motion and spin relaxation, which leads to insights in folding patterns and conformational dynamics of many globular and membrane proteins (*66-71*) and nucleic acids (*72-74*). For proteins or oligomers with two or more spin labels, ESR distance measurements are possible.

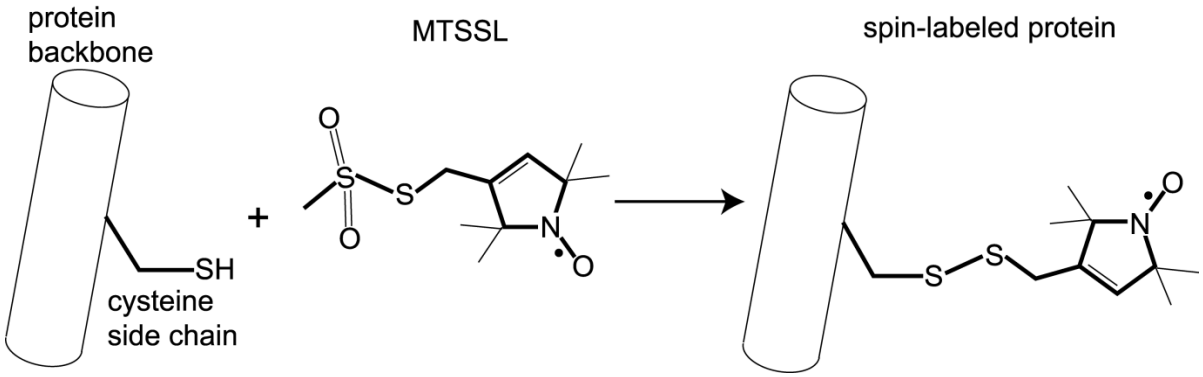

Figure 1-1. The spin-labeling scheme. The (1-oxyl-2,2,5,5,-tetramethylpyrroline-3-methyl)-methanethiosulfonate (MTSSL) spin label is chemical attached to the cysteine side chain of a protein.

1.2 ESR DISTANCE MEASUREMENTS

Since the focus of this thesis is spin-spin distance measurements, this section provides a brief overview of the established ESR distance measurement methodologies including Continuous-Wave ESR, Saturation Recovery, Inversion Recovery, Double Quantum Coherence and DEER. The principle, the pulse sequence, and the established data analysis procedure of the DEER technique are emphasized.

• *Continuous-Wave(CW) ESR measures short distances*

Continuous-wave ESR can determine spin-spin distances in the range of 8 to 25 Å, depending on the paramagnetic species and the experimental method. There are typically two methods to measure spin-spin distances. First, for a doubly labeled protein with a spin-spin distance of less than 25 Å, the ESR spectrum is often broader than the spectrum of a singly labeled protein, due to the presence of a second spin. By calibrating the excess ESR spectral linewidth of the doubly spin labeled protein, the spin-spin distance distribution can be determined (*52, 75, 76*). Second, in a doubly-labeled protein, the two coupled electrons form four electron states: αα, αβ, βα and ββ, as shown in Figure 1-2a. The energy transitions, namely transitions 1, 2, 3 and 4, are allowed by the ESR selection rule ($\Delta m_S = \pm 1$). Another energy transition between the αα state and the ββ state, namely transition 5, becomes weakly allowed when the dipolar interaction is large (i.e. at short spin-spin distances). As shown in Figure 1-2, the frequency of transition 5 is twice that of the allowed transition frequencies. Therefore, the ESR absorption peaks of the transition 5 occur at half the magnetic field of the allowed transitions (Figure 1-2 b). Eaton and coworkers demonstrated that the intensity ratio of the half field transition versus the allowed transition is inversely proportional to r^6, where r is the

interspin distance (*77*, *78*). Distance in the range of 4-12 Å can be measured by this method. Both approaches are sensitive to r^{-6} and this dictates the upper distance limit.

• *Pulsed ESR methods allow long range distance measurements*

Relaxation based ESR methods. In a molecule containing a paramagnetic metal ion and a nitroxide spin label, the spin-spin distance can be measured by using relaxation based methods. The mechanism is as follows. At room temperature, the relaxation rates of a paramagnetic metal ion spin is generally many orders of magnitude faster than those of a nitroxide spin. Therefore, the metal ion spin is often considered as a fast-relaxing spin, and the nitroxide spin is often considered as a slowly-relaxing spin. In the presence of both spins, the relaxation rates of the nitroxide spin is enhanced in a distance dependent manner. Kulikov and Likhtenshtein showed the relationship between the spin-lattice relaxation rate of a slowly-relaxing spin, such as a nitroxide spin, in the presence and in the absence of a fast-relaxing spin, such as a metal ion spin, to be (*79-81*)

$$\frac{1}{T_{1s}} = \frac{1}{T_{1s}^0} + S(S+1) \times \left[\frac{b^2 T_{2f}}{1+(\omega_f - \omega_s)^2 T_{2f}^2} + \frac{c^2 T_{1f}}{1+\omega_s{}^2 T_{1f}^2} + \frac{e^2 T_{2f}}{1+(\omega_f + \omega_s)^2 T_{2f}^2} \right] \qquad (1\text{-}1)$$

$$b^2 = \frac{1}{6} g_s^2 g_f^2 \beta_e^4 \frac{(1 - 3cos^2\theta)^2}{\hbar^2 r^6}$$

$$c^2 = 3 g_s^2 g_f^2 \beta_e^4 \frac{sin^2\theta cos^2\theta}{\hbar^2 r^6}$$

$$e^2 = \frac{3}{2} g_s^2 g_f^2 \beta_e^4 \frac{sin^4\theta}{\hbar^2 r^6}$$

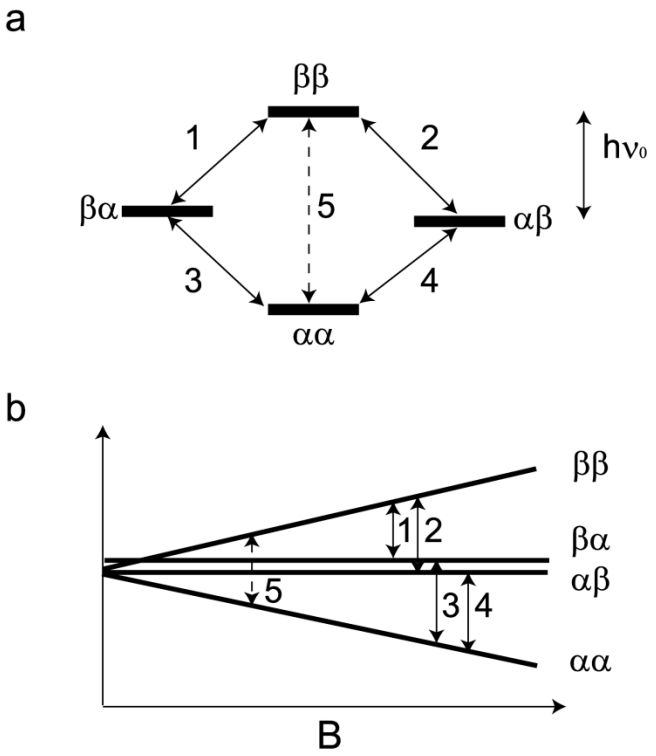

Figure 1-2. (a) The energy level diagram of a two-electron system. The transitions 1, 2, 3 and 4 are allowed by ESR selection rule. The transition 5 is weakly allowed when the dipolar interaction is large. (b) Plot of the energy versus the magnetic field. The "weakly allowed" transition occurs at half the magnetic field of the allowed transitions, as shown by the dotted line.

where *f* and *s* denote the fast- and slowly-relaxing spins, respectively; T_{1s}^{0} is the spin-lattice relaxation time of the slowly-relaxing spin in the absence of the fast-relaxing spin; T_{1s} is the spin-lattice relaxation time of the slowly-relaxing spin perturbed by the fast-relaxing spin; T_{1f} is the spin-lattice relaxation time and T_{2f} is the spin-spin relaxation time of the fast-relaxing spin. *S* corresponds to the electron spin quantum number of the faster-relaxing spin; ω_f and ω_s are the resonant frequencies for the fast- and slowly-relaxing spins, respectively; g_f and g_s are the *g* factors for the fast- and slowly-relaxing spins, respectively; β_e is the Bohr magneton; *r* is the interspin distance between two spins, and θ is the angle between the interspin vector and the external magnetic field, B_0. The enhancement of the relaxation rate of the slowly-relaxing spins depends on r^{-6}, as indicated by Equation 1-1. To measure distances using Equation 1-1, one needs to measure the relaxation rates of the paramagnetic centers. Commonly used ESR techniques to measure these relaxation rates are Inversion Recovery (IR) and Saturation Recovery (SR). Using these methods, distances between the fast-relaxing transition metal ions, such as Mn^{2+}, Fe^{3+} and Cu^{2+}, and the slowly-relaxing nitroxide spin labels have been determined (*82-84*).

Kulikov and Likhtenshtein later showed that (*82-84*), the maximum measurable distance depends on the intrinsic properties of the metal ion species such as the value of S, and the metal ion relaxation times. For instance, for a Fe^{3+}-nitroxide spin pair, up to 150 Å distances could be measured. The maximum measurable Cu^{2+}-nitroxide distance was also extended to ~100 Å, compared with that of less than 10 Å using the CW-ESR approaches. Consequently, the relaxation methods allow longer distance measurements. However, due to limitations in experimental methodology, such measurements were restricted to very low temperatures. Recent

advances in methodology have allowed distance measurements at physiological temperatures, compared with other pulsed ESR methods (*1, 2, 85, 86*).

Besides these elegant contributions, the major limitation of the relaxation methods is that, the determined distance is only the average distance between the two spin centers. The distribution of distances between spin centers is not directly revealed, which truly prevents the determination of the flexibility or dynamics of targeted proteins. To probe the distribution of distances between spin centers, other pulsed ESR methods, such as DEER and Double Quantum Coherence (DQC), are utilized; although those methods require lower experimental temperatures.

DEER and DQC. The pulsed ESR methods, DEER and DQC, extract the weak magnetic dipole-dipole interaction between two paramagnetic centers from other contributions to the ESR spectrum, by using specific pulse sequences and phase cycling. A DEER or DQC signal is usually a time domain curve that modulates with the frequency of the dipolar interaction between the two spins. Comparing with the relaxation methods, DEER and DQC experiments need to be performed at lower temperatures due to the following reasons.

The Hamiltonian term of the magnetic dipolar interaction between two free electron spins is given by

$$\hat{H}_{12} = \hat{S}_1 \cdot \overline{\overline{D}} \cdot \hat{S}_2 = c\frac{1}{r_{12}^3}\left[\hat{S}_1 \cdot \hat{S}_2 - \frac{3}{r_{12}^2}\left(\hat{S}_1 \cdot \vec{r}_{12}\right)\left(\hat{S}_2 \cdot \vec{r}_{12}\right)\right] \qquad (1\text{-}2)$$

where *c* is a constant given by

$$c = \frac{\mu_0}{4\pi\hbar} g_1 g_2 \beta_e^2 \qquad (1\text{-}3)$$

The parameter, r_{12}, represents the distance between the two spins. The μ_0 term is the permittivity of vacuum, and the β_e term is the Bohr magneton. For a system with S= ½, Equation 1-2 can be extended to the form of

$$\hat{H}_{12} = \frac{c}{r_{12}^3}(\hat{S}_{z1}\hat{S}_{z2}(1-3cos^2\theta) - \frac{1}{4}(\hat{S}_{1+}\hat{S}_{2-} + \hat{S}_{1-}\hat{S}_{2+})(1-3cos^2\theta) - \frac{3}{2}(\hat{S}_{1+}\hat{S}_{2z} +$$

$$\hat{S}_{1z}\hat{S}_{2+})\sin\theta\cos\theta\, e^{-i\varphi} - \frac{3}{2}(\hat{S}_{1-}\hat{S}_{2z} + \hat{S}_{1z}\hat{S}_{2-})\sin\theta\cos\theta\, e^{i\varphi} - \frac{3}{4}\hat{S}_{1+}\hat{S}_{2+}sin^2\theta e^{-2i\varphi} -$$

$$\frac{3}{4}\hat{S}_{1-}\hat{S}_{2-}sin^2\theta e^{2i\varphi} \qquad (1\text{-}4)$$

where θ is the angle between the external magnetic field, B_0 (also the z-axes of the lab frame) and the spin-spin vector, r_{12}, and φ is the angle between the x-axes of the lab frame and the projection of the interspin vector onto the xy-plane of the lab frame (cf. Figure 1-3). Under the high field approximation, the terms containing $\hat{S}_{1+}$, $\hat{S}_{1-}$, $\hat{S}_{2+}$, and $\hat{S}_{2-}$ in Equation 1-4 are negligible compared with the term containing $\hat{S}_{z1}\hat{S}_{z2}$. The Hamiltonian $\hat{H}_{12}$ can be written as (*87*)

$$\hat{H}_{12} = \omega_{12}\hat{S}_{z1}\hat{S}_{z2} \qquad (1\text{-}5)$$

where

$$\omega_{12} = c\frac{1}{r_{12}^3}(3cos^2\theta - 1) \qquad (1\text{-}6)$$

In Equation 1-6, the ω_{12} is the angular frequency due to the dipolar interaction.

As shown by Equation 1-6, the ω_{12} term depends on the spin-spin distance, r_{12}, and the θ angle. At room temperature, the dipolar interaction described by Equation 1-5 is averaged to zero due to the fast molecular tumbling. To measure distances, the protein sample is usually fast-frozen from the room temperature. The measured, "static" distance distribution at low temperatures still reflects the flexibility or the dynamics of the protein at physiological temperatures.

In a powder sample, the relative orientation of the external magnetic field and the interspin vector in the frozen sample is randomized, meaning that the θ angle ranges from 0° to 90°. Assuming a full excitation of the θ angles, which is essentially the case of nitroxide spin

labels, every spin pair contributes to the signal. This effect can be better visualized by a Fourier transformation (FT) of the time domain data, where spins at each orientation θ leads to a "peak". The frequency of each peak can be calculated by using Equation 1-6. The intensity of the "peak" depends on the number of spin pairs that contribute to the corresponding θ angle, which generally follows a $\sin(\theta)$ [$0° < \theta < 90°$] function. Consequently, the dominant peaks correspond to the case of $\theta = 90°$. Interspin vectors corresponding to $\theta = 0°$ only contribute to the shoulder peaks in the spectrum. This characteristic spectrum is known as the *"Pake pattern"* (cf. Figure 1-4). For most nitroxide spin labeled samples, the Pake pattern is resolved, although a distribution of distances broadens the Pake pattern and weakens the shoulder peaks.

Although DEER and DQC share the same spectrum, the principles of using DEER and DQC to measure distances are slightly different. Developed by Freed and coworkers, the DQC experiment excites the double quantum coherence of a spin pair (*88-90*). The rate of the double quantum coherence formation is related to the dipolar interaction between the two electron spins, providing spin-spin distances. To selectively measure the formation of the double quantum coherence signal, a pulse sequence containing 6 pulses and a 256-step phase cycling that isolates the DQC pathway from all other unwanted pathways are employed in the DQC experiment. More details on the DQC method can be found in literatures (*88-90*).

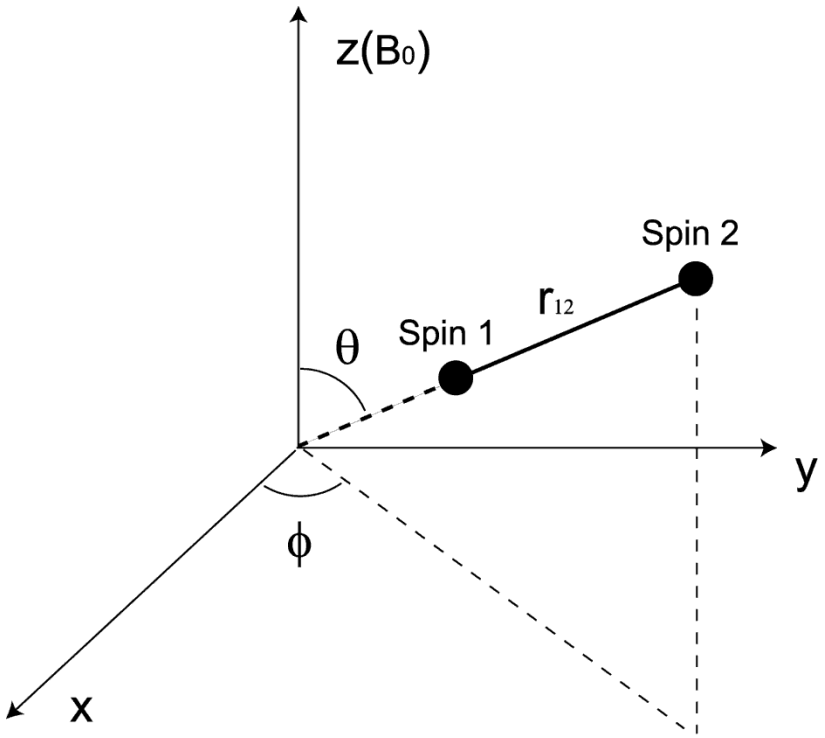

Figure 1-3. The definition of angles used in Equation 1-4. The angle between the interspin vector, r_{12} and the external magnetic field, B_0, is defined as θ. The angle between the x-axes of the lab frame and the projection of r_{12} on the xy-plane is defined as φ.

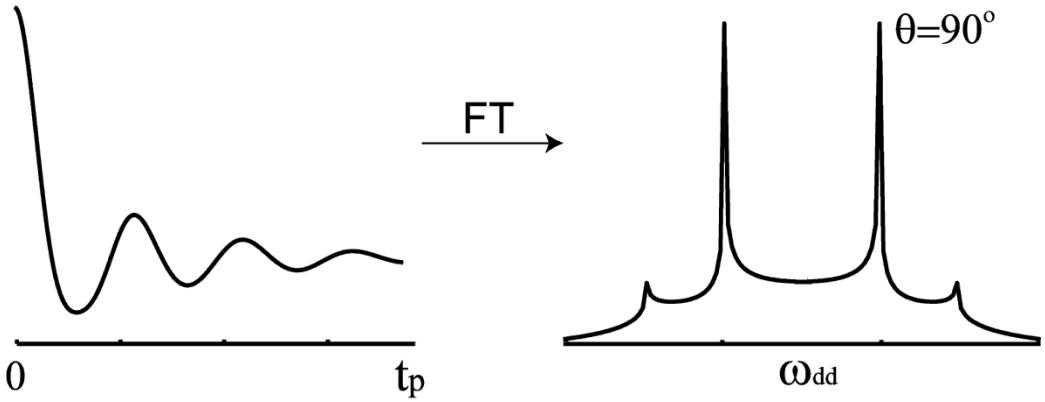

Figure 1-4. A typical DEER or DQC signal in the time domain and the frequency domain. The frequency domain spectrum is know as the Pake pattern, with the dominant peak corresponding to $\theta = 90^{o}$ and the shoulder peak contributed by $\theta = 0^{o}$.

The DEER technique, on the other hand, uses microwave pulses at two different frequencies to separately excite spins in resonance with each frequency. The dipolar coupling between these excited spins can be extracted from the DEER signal, providing distances. To illustrate the principle of DEER, we use a doubly nitroxide-labeled protein as an example. The principle of Cu^{2+}-based DEER is analogous. The pulse sequence of the three-pulse DEER is shown in Figurer 1-5a. The pulses applied at the main frequency, ν_1, are often referred to as the observer or the probe pulses, and the pulse applied at a slight different frequency (~70 MHz lower), ν_2, is known as the pump pulse. As shown in Figure 1-5a and b, the observer pulses excite part of the nitroxide ESR spectrum, generating a primary echo. The excited spins are named 'spin 1' in this thesis. At the pump frequency, a π pulse is applied to irradiate spins in resonance with ν_2 (namely 'spin 2') with a flip angle of π. The inversion of the magnetization of 'spin 2' due to the pump π pulse induces a change in the local magnetic field that 'spin 1' experiences. This change in the local field introduces a phase factor of $\cos(\varphi)$ to the refocused echo. The angle φ depends on the position of the pump pulse, t_p, and the magnetic dipolar interaction between these two spins, ω_{12}. As the pump pulse is stepped out, the size of the refocused echo is modulated with ω_{12}. The measured DEER signal, V(T), is therefore proportional to $\cos(\omega_{12} t_p)$.

It is worth mentioning that the spins in resonance with different frequencies (c.a. 'spin 1' and 'spin 2') need not be located in the same molecule (oligomer). Considering an ensemble of doubly labeled proteins, as shown in Figure 1-6, the interspin distance within the same protein is apparently the distance one wants to measure (cf. solid bars in Figure 1-6). The dipolar

interaction between these spins is called the "intramolecular" dipolar interaction, contributing to part of the DEER signal.

For a rigidly separated nitroxide spin pair in a protein molecule at low temperatures, the relative orientation of the interspin vectors and the external magnetic field is randomized. The DEER signal purely due to the intramolecular interaction, $V(t_p)$, can be analytically calculated by integrating over all possible θ angles.

$$V(t_p) = \int_0^{\pi/2} \xi(\theta) \cos(\omega_{12} t_p) \sin\theta \, d\theta \qquad (1\text{-}7)$$

where t_p is the time interval between the observer π/2 pulse and the pump pulse (cf. Figure 1-5a), ω_{12} is given by Equation 1-6, $\xi(\theta)$ is a factor that describes the excited θ angles due to the microwave pulses. For the case of a nitroxide spin pair, this factor is close to 1 for all the θ angles. A simulated DEER signal based on Equation 1-7 is shown in Figure 1-4a. The spectrum after Fourier transformation provides a Pake pattern (*91*) (Figure 1-4b), as discussed early in this section.

For real biological samples, however, due to the inherent flexibility of macromolecules and nitroxide spin labels, we expect a broadened distance distribution between the nitroxide spin labels. DEER signal due to intramolecular interaction can be calculated by summation over all the interspin distances with corresponding probabilities, P(r) (*92*).

$$V(t_p) = \int_{Rmin}^{Rmax} \int_0^{\pi/2} \xi(\theta) \cos(\omega_{12} t_p) \, \mathrm{P(r)} \sin\theta \, d\theta dr \qquad (1\text{-}8)$$

where P(r) is the distance distribution function. Defining x=cos(θ), $\omega_{DD}=\omega_{12}/r^3$, and assuming that $\xi(\theta)$ is 1, Equation 1-8 can be rewritten as

$$V(t_p) = \int_{Rmin}^{Rmax} \int_0^1 \cos((1-3x^2)\omega_{DD} t_p) \, P(r) dx dr \qquad (1\text{-}9)$$

The R_{min} and R_{max} are the range of possible distances for P(r). Equation 1-9 is a Fredholm equation with a kernel function, $\kappa(r,t_p)$, given by

$$\kappa(r,t_p) = \int_0^1 \cos\left((1-3x^2)\omega_{DD}t_p\right) dx \qquad (1\text{-}10)$$

Consequently, Equation 1-9 becomes

$$V(t_p) = \int_{Rmin}^{Rmax} \kappa(r,t_p)P(r)dr \qquad (1\text{-}11)$$

The distance distribution function, P(r), can be extracted from the Fredholm equation (Equation 1-11) and the corresponding kernel function (Equation 1-10).

For the case of nitroxide spin labels, a model free method to convert the time domain data into a distance distribution, known as the Tikhonov regularization method, has been implemented by Chiang *et. al.*(*93*) and Jeschke *et. al.* (*94*). More details about the Tikhonov regularization method is as follows. Equation 1-11 is converted into a discrete form for M data points and N solution points:

$$V(t_p) = \int_{Rmin}^{Rmax} \kappa(r,t_p)P(r)dr \approx \sum_{j=1}^{N} \omega_j \kappa\left(t_{p_i}, r_j\right) P(r_j) \qquad (1\text{-}12)$$

where $\omega_j = (R_{max} - R_{min})/N$, $r_j = (j - 1/2)\omega_j + R_{min}$ for $j = 1, 2, \ldots, N$, and $t_{p,i} = (i - 1/2)\,(t_{p,max}/M)$ for $i = 1, 2, \ldots, M$. The discrete form is converted into a system of linear algebraic equations represented by

$$\vec{S} = \overleftrightarrow{K} \cdot \vec{P} \qquad (1\text{-}13)$$

Elements of $\overleftrightarrow{K}$ are $\kappa_{ij} = \omega_j \kappa\left(t_{p_i}, r_j\right)$ and $\vec{S}$ are $S_i = V\left(t_{p_i}\right)$; for i=1,2,…M, and j=1,2,…,N. Here, $\overleftrightarrow{K}$ denotes an operator that maps the function $\vec{P}$ onto the experimental data vector, $\vec{S}$. The Tikhonov regularization method modifies the equation to the following functional form, $\Phi[\vec{P}]$:

$$\Phi[\vec{P}] = \left\|\overleftrightarrow{K} \cdot \vec{P} - \vec{S}\right\|^2 + \lambda^2 \left\|\overleftrightarrow{L} \cdot \vec{P}\right\|^2 \qquad (1\text{-}14)$$

where λ is the so-called regularization parameter and $\overleftrightarrow{L}$ is an operator identity. The regularized solution P_λ is obtained by minimizing Equation (1-15):

$$\vec{P}_\lambda = \left(\overleftrightarrow{K}^T \cdot \overleftrightarrow{K} + \lambda^2 \overleftrightarrow{L}^T \cdot \overleftrightarrow{L}\right)^{-1} \cdot \overleftrightarrow{K}^T \cdot \vec{S} \qquad (1\text{-}15)$$

The quality of the result depends strongly on the regularization parameter λ. If λ is too small, the result will show artificial peaks. If λ is too large, the result will be over-smoothed, providing a distance distribution that is too broadened. The criteria for choosing the optimum λ using the L-curve method can be found in references (*95*, *96*). Jeschke(*97*) has implemented a program package for fitting DEER data (DEERAnalysis 2006) based on the Tikhonov regularization method, which can be freely downloaded.

On the other hand, the DEER signal also contains the contribution from the dipolar interaction between spins excited from different proteins, which is also known as the intermolecular interaction. Since the proteins are randomly distributed, the distance dependent term in Equation 1-7 is averaged out, and a featureless decay is observed. Generally, the baseline is in the shape of an exponential decay function, which is often removed before DEER data analysis.

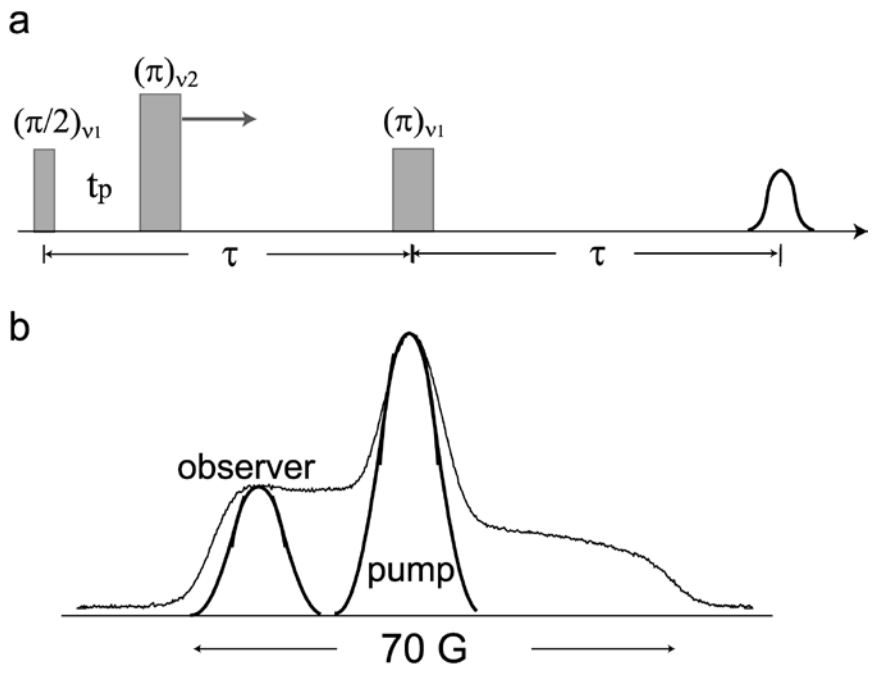

Figure 1-5. (a) The pulse sequence applied in a three-pulse DEER experiment. (b) The excitation profiles of probe and pump frequencies.

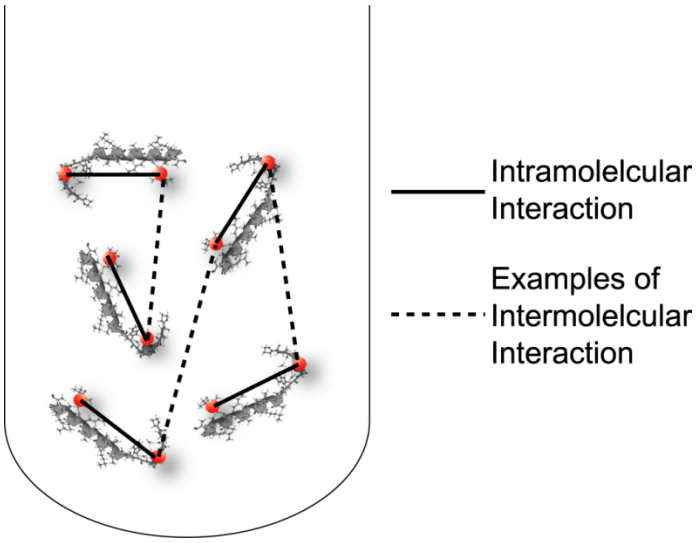

Figure 1-6. An illustration of the intramolecular interaction and the intermolecular interaction in a doubly labeled protein sample.

1.3 METAL ION BASED DEER

Nitroxide-to-nitroxide distances extracted by using Tikhonov regularization have served as important constraints to probe the structure and dynamics of proteins. Recently, attempts to measure distances between metal ion centers using DEER have been carried out. The extension of the spin probes to the case of metal ions provides an opportunity to measure distances in metalloproteins. In combination with SDSL, additional distance constraints, such as the metal ion–metal ion and the metal ion–nitroxide distances, can be obtained. It is found that ~ 1/3 of known proteins require metal ions to carry out their functions. Therefore, the metal ion-based DEER distance measurements have wide biological applications. The use of metal ions as the spin probes faces specific challenges, such as the relatively low signal-to-noise ratio and, more importantly, the so-called "orientational effects" on the experimental data. This section will provide a brief introduction of the motivation of using metal ions as spin probes and the specific challenges of using metal ions in DEER experiments.

• *Metal ions in proteins*

Metalloproteins are proteins containing and requiring cofactors of metal ions or metal-ion clusters to perform their biological functions. Depending on specific functions, metalloproteins are subcategorized to catalytic enzymes, oxygen and ion transport and storage proteins, and signal transduction proteins. Commonly found metal ions in metalloproteins are Mg^{2+}, Mn^{2+}, Zn^{2+}, Ca^{2+}, Cu^{2+} and Fe^{3+}. These metal ions are usually coordinated to nitrogen, oxygen or sulfur atoms from amino acids of the metalloproteins, forming stable metal ion-bound protein complexes. Among these ions, Mn^{2+}, Cu^{2+} and Fe^{3+} are typically paramagnetic, which can serve as the unpaired electron spin probes for distance measurements using DEER. There are also

applications of DEER distance measurements based on metal ion clusters (*7*, *57*). Among these metal centers, Cu^{2+} is the most commonly used in DEER distance measurements. Due to the electronic configuration of the Cu^{2+} ion, there is only one unpaired electron in the 3d atomic orbital of the copper atom. For Mn^{2+} or Fe^{3+} one can have as many as 5 unpaired electrons (the high spin state). The energy level diagram for Cu^{2+} is therefore relatively simpler, which potentially reduces the complication in the DEER data analysis. The relatively narrower Cu^{2+} absorption spectral line width also makes Cu^{2+} more favorable than other ions. This is because with the same sample concentration, ions with narrower line width usually provide higher signal-to-noise ratio in DEER measurements. Based on these two reasons, Cu^{2+} is relatively more commonly used in DEER compared with other ions. It is worth mentioning that the Cu^{2+} spectral line width is still 10 times broader than that of the nitroxide spin labels, as shown from Figure 1-7.

• *Challenges of using Cu^{2+} as the spin probe*

The broad Cu^{2+} ESR absorption spectrum generates potential challenges for the measurement of Cu^{2+}-based distances using DEER. The broadening of the Cu^{2+} spectrum originates from the larger anisotropies of the Cu^{2+} g and hyperfine tensors, which are intrinsic properties of the paramagnetic species. For a free electron, the g tensor is isotropic, meaning that the magnitude of the g value is identical in all directions. The ESR transition frequency of this electron is also isotropic, given by

$$\upsilon_{ESR} = g\beta_e B_0 \qquad (1\text{-}16)$$

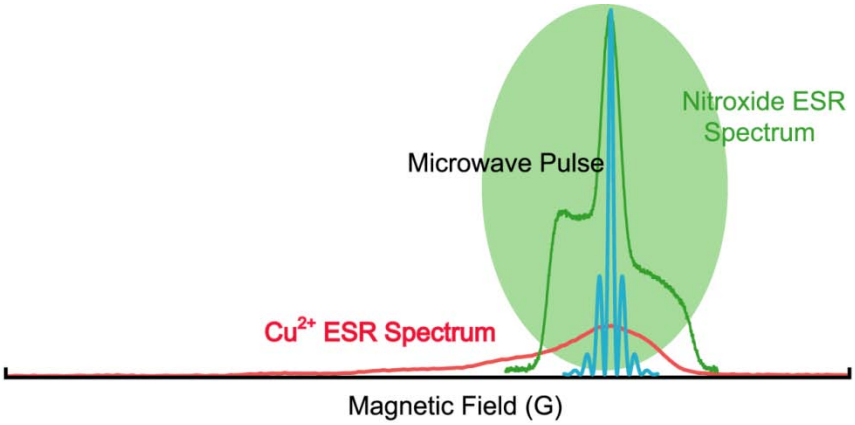

Figure 1-7. The example ESR absorption spectra of Cu^{2+}(red) and nitroxide spin labels (green). The typical coverage of the microwave pulses used in the DEER experiment is shown in blue.

where β_e is the Bohr magneton, B_0 is the external magnetic field, and g is the isotropic value of the g tensor. As the electron is localized to a specific atomic orbital, the ESR transition frequency becomes proportional to the local magnetic field, B_{local}, that the electron experiences, instead of the constant external magnetic field. This transition frequency is given by

$$\upsilon_{ESR} = g\beta_e B_{local} \qquad (1\text{-}17)$$

The B_{local} is a contribution from B_0 and the magnetic field due to the interaction of the atomic orbital angular momentum with B_0. Due to the anisotropic shape of the atomic orbitals (cf. Figure 1-8a), the ESR transition frequency is not isotropic but rather dependent on the relative orientation of the atomic orbital and the external magnetic field (cf. Figure 1-8b). Consequently, the absorption spectrum contains contributions from all ESR transitions that occur at every relative orientation. Such anisotropic character is also present in the hyperfine tensor, and it originates from the anisotropic electron-nuclear interaction. Generally, a 3x3 matrix is used to describe an orientation dependent tensor. The principal g values, g_{xx}, g_{yy} and g_{zz}, are usually referred as to the diagonal elements of the g tensor. The principal hyperfine values, usually named A_{xx}, A_{yy} and A_{zz}, are the diagonal elements of the hyperfine tensor.

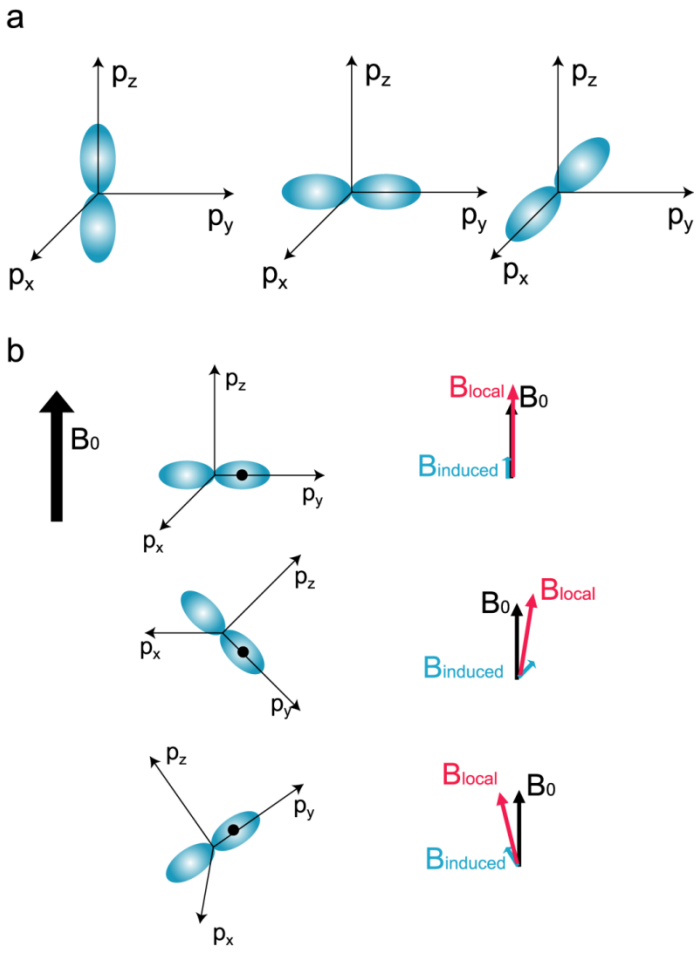

Figure 1-8. (a) An illustration of the anisotropic p_x, p_y and p_z orbitals. (b) The effects of induced magnetic field, $B_{induced}$, generated by the orbital on the local magnetic field that the electron experiences. The ESR transition frequency depends on not only B_0, but also the orientation of the orbital (cf. Equation 1-17).

The atomic orbital associated with the nitroxide and Cu^{2+} paramagnetic center is the 2p orbital of the nitrogen atom and the 3d orbital of the copper atom, respectively. The difference in the electron spin intensity and the shape of these two orbitals results in differences in the anisotropy of the g and hyperfine tensors between nitroxides and Cu^{2+}. Typically, the x-, y- and z-axes of the nitroxide spin label are along the N-O bond of MTSSL, the p_y orbital of the nitrogen atom and the direction perpendicular to the xy-plane, respectively (cf. Figure 1-9a). The typical principal g values for the nitroxide electron spin are 2.0032, 2.0046 and 2.0069, although these values may differ slightly for different samples. The hyperfine tensor is often assumed to be parallel to the g tensor. The typical principal nitroxide hyperfine values are A_{xx} = 5 G, A_{yy} = 5 G and A_{zz} = 30 G. On the other hand, the orientation of the Cu^{2+} g-tensor depends on the Cu^{2+} bound ligands and coordination geometry. One of the common Cu^{2+} binding modes is the type II Cu^{2+} center, which has a square-pyramidal geometry. The Cu^{2+} ion is coordinated by four ligands in the equatorial plane and a fifth ligand outside of the plane (cf. Figure 1-9b). The x- and y-axes of the Cu^{2+} g-tensor usually lie in the equatorial plane, parallel to two coordinate bonds (cf. Figure 1-9b). The z-axes points at a direction that is perpendicular to the equatorial plane (cf. Figure 1-9b). The g_{xx} and g_{yy} values are usually close to each other for the type II Cu^{2+}, in the range of 2.05-2.08. The g_{zz} value is typically in the range of 2.2 to 2.4. For a general Cu^{2+} binding mode, the g-tensor can be estimated by using the ORCA package developed by Neese and coworkers (*98*). Nevertheless, the g values are still in the same range as described above. The typical principal copper hyperfine values are A_{xx} = 30 G, A_{yy} = 30 G and A_{zz} = 160 G. Using these typical values, example ESR absorption spectra of these two samples are overlaid and shown in Figure 1-7.

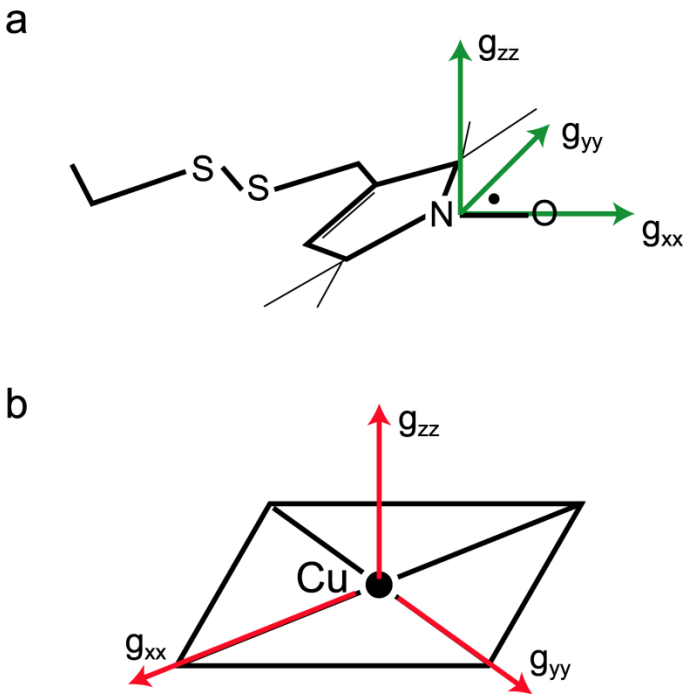

Figure 1-9. The orientation of a nitroxide g-tensor (a) and a type II Cu^{2+} g-tensor (b).

Orientation selective microwave pulses applied in the DEER experiments are usually 20 to 50 ns, corresponding to the pulse coverage of 20 to 50 MHz. Compared with a nitroxide spectral band width of 200 MHz, these pulses can excite most of the nitroxide spin orientations if applied as shown in Figure 1-5b. Consequently, the simplified kernel function can be used to extract the distance distributions between nitroxide spin labels (cf. section 1.2 of this thesis).

For the case of Cu^{2+}, the pulses can cover only a small part of the ~2 GHz Cu^{2+}-ESR spectrum, exciting a small portion of the Cu^{2+} spin pairs. The Fourier transformation of the Cu^{2+}-based DEER signal is not anticipated to be a Pake pattern as in the case of nitroxide, but becomes dependent on the excited θ angles. The simplified kernel function shown in Equation 1-10 is not suitable to extract the spin-spin distances from the DEER data due to this partial orientation excitation. One can remove this limitation by increasing the coverage of the pulses to excite more spin orientations. However, stronger pulses (c.a. 4 ns pulses) can also excite the electron-nuclear interaction, producing additional modulations to the DEER signal, which makes the determination of precise distance distributions problematic.

We sought to account for the partial orientation excitation effects by quantitatively evaluating the excitation probability for each θ angle. As demonstrated by Maryasov *et. al.*, for a nitroxide-based system (*99*), the θ excitation probability (also called the θ excitation function) depends on the experimental magnetic field, the frequency offset between the pump and the observer pulses, the g and hyperfine anisotropies and more importantly, the relative orientation of the g-tensors of the two coupled spins. We extended their analysis of the θ excitation function to the case of Cu^{2+}, and demonstrated the possibility of measuring Cu^{2+}–Cu^{2+} distances using DEER, as shown in Figure 1-10 and Chapter 2. In Chapter 3, we examined the role of the relative orientation distributions between the two Cu^{2+} centers in such experiments (cf. Figure 1-

11 and Chapter 3). In Chapter 4 we summarized the optimal experimental conditions to ensure efficient Cu^{2+}-based DEER data collection. Finally, we explored the developed methodology to the restriction endonuclease EcoRI-DNA complex and provided the first experimental evidence to show that the Cu^{2+} binding residue of the EcoRI is histidine 114. This result leads to the understanding of the roles of metal ions in the catalytic process of the DNA cleavage (cf. Figure 1-12 and Chapter 5).

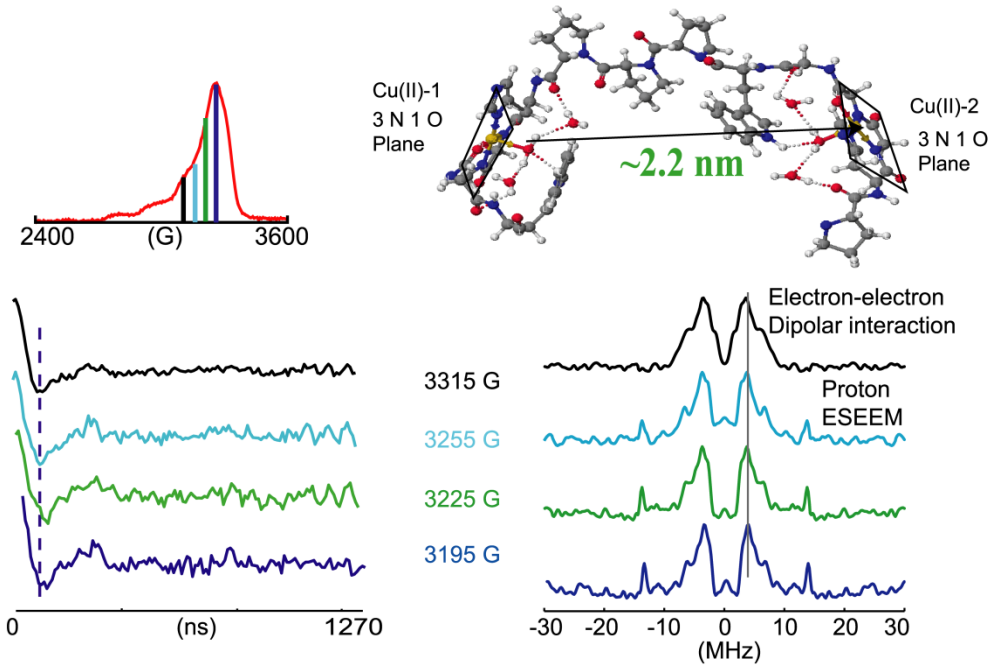

Figure 1-10. The DEER data on a synthetic model peptide at four different magnetic fields, indicating that Cu^{2+}-Cu^{2+} distance measurement is possible using DEER.

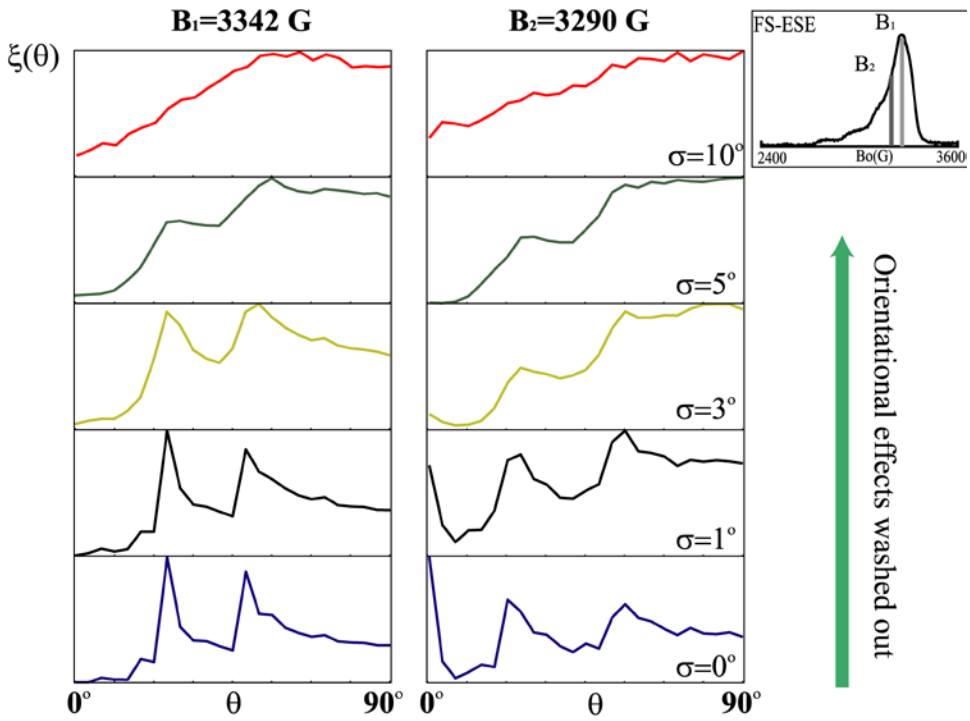

Figure 1-11. The role of the orientation distribution in the θ excitation profiles. The θ excitation profiles at two different magnetic fields are simulated. At both magnetic fields, as the flexibility in the relative orientation between the two Cu^{2+} centers is increased, the θ excitation profiles become indistinguishable. The orientational selectivity is reduced.

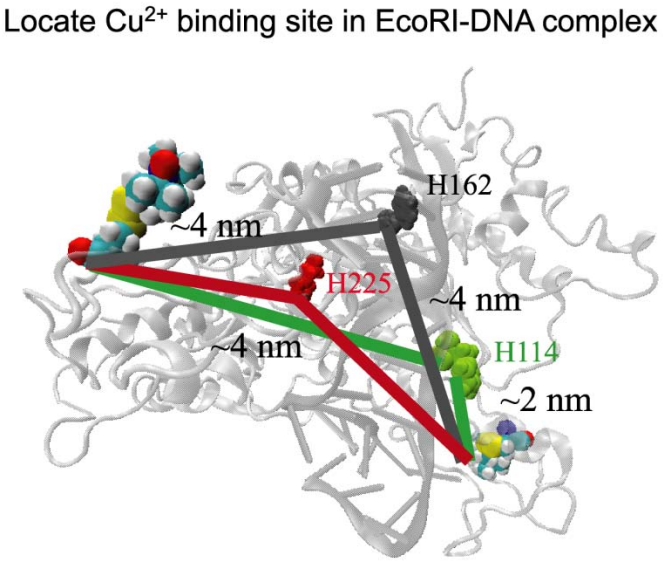

Figure 1-12. Using the distances measured from DEER, we triangulate the Cu^{2+} binding residue in the EcoRI-DNA complex to be histidine 114 (as shown in green).

2.0 ROLE OF ORIENTATIONAL SELECTIVITY IN COPPER ION–COPPER ION DISTANCE MEASUREMENTS

This work, written in collaboration with James S. Becker and Sunil Saxena, has been published in Journal of Magnetic Resonance, 2007, V.188, pages 337-343 (50).

2.1 ABSTRACT

The effects of orientational selectivity on the 4-pulse electron electron double resonance (PELDOR) ESR spectra of coupled Cu^{2+}–Cu^{2+} spins are presented. The data were collected at four magnetic fields on a poly-proline peptide containing two Cu^{2+} centers. The Cu^{2+}–PELDOR spectra of this peptide do not change appreciably with magnetic field at X-band. The data were analyzed by adapting the theory of Maryasov, Tsvetkov, and Raap [A.G. Maryasov, Y.D. Tsvetkov, J. Raap, Weakly coupled radical pairs in solids: ELDOR in ESE structure studies, Appl. Magn. Reson. 14 (1998) 101–113]. Simulations indicate that orientational effects are important for Cu^{2+}–PELDOR. Based on simulations, the field-independence of the PELDOR data for this peptide is likely due to two effects. First, the flexibility of the peptide washes out the orientation effects. These effects reduce the suitability of the poly-proline based peptide as a good model system to experimentally probe orientational effects in such experiments. Second,

for this peptide, the Cu^{2+} g-tensor(s) are in a very specific orientation with respect to the interspin vector. This appears to a very stringent requirement, which needs to be examined in the future. An average Cu^{2+}–Cu^{2+} distance of 2.1–2.2 nm was determined, which is consistent with earlier double quantum coherence ESR results.

2.2 INTRODUCTION

The sensitivity of pulsed electron spin resonance (ESR) to magnetic dipolar interactions has recently provided a powerful methodology to measure distances (~18–70 Å) between two spin labels (*1, 2, 85, 100-103*), in order to establish global folding patterns in proteins (*10, 104-109*) and nucleic acids (*21, 110-112*). Thus far, the ESR method has largely been restricted to the use of nitroxides as the spin labels. The internal orientations of the nitroxide spin labels typically have only a small effect on the spectral line shape in the pulsed electron electron double resonance (PELDOR) at X-band (*2*), although they have been observed in some cases (*113*). These orientation effects become significant at higher frequencies (*114, 115*), and can be used to infer the relative orientation of the spin labels.

Recently, the ESR distance mapping methodology has been extended to the case of paramagnetic metal centers in metalloproteins (*7, 11, 116*), oligomers (*52*), and peptides (*117*). For paramagnetic metals, the large g and hyperfine anisotropies can complicate the analysis of the experimental spectra. There is limited information about the effect of the internal orientation on the Cu^{2+}–Cu^{2+} distance measurements using PELDOR. Previous papers on Cu^{2+}–Cu^{2+} distance measurements using pulsed ESR only focused on the $g_{\perp}$ range of the Cu^{2+}–ESR spectrum (*7, 116, 117*).

In this Chapter, we address the effects of orientational selectivity on the 4-pulse PELDOR spectra of Cu^{2+} spins. Experimental data were obtained using a model peptide that contains Cu^{2+} binding sites (*117*). The effects of internal orientation on the Cu^{2+}–Cu^{2+} distance are analyzed by using the theory of Maryasov *et. al.*. (*99*). By fitting the experimental data to the theory, the Cu^{2+}–Cu^{2+} distance is determined. The results indicate that, for this peptide, the PELDOR line shape does not depend on the magnetic field at X-band. However, in general, the effects of the orientational selectivity must be considered so that accurate distance constraints are measured.

2.3 MATERIALS AND METHODS

A peptide with a sequence of PHGGGWPPPHGGGW was synthesized. The PHGGGW sequence is a common copper binding motif found in the prion protein (*118*). For ESR experiments, a 3.5 mM solution of the peptide in 30% glycerol/30% 2,2,2-trifluoroethanol/40% water containing 150 mM NaCl, buffered to pH 7.46 using N-ethylmorpholine was prepared. Two equivalents of Cu^{2+} were added to the solution from a 0.1 M standard solution of $CuSO_4$. About 30 μl of this solution was used for ESR experiments. All experiments were performed at a temperature of 20 K on a Bruker ElexSys E580 CW/FT ESR spectrometer. For the 4-pulse PELDOR experiments, a $(\pi/2)_{v1} - \tau_1 - (\pi)_{v1} - (\tau_1+T) - (\pi)_{v2} - (\tau_2-T) - (\pi)_{v1}$ pulse sequence was used. The detection $\pi/2$ pulse was 24 ns and its frequency (ν_1) was 9.556 GHz. The pump pulse length was 48 ns and its frequency (ν_2) was 9.656 GHz. These pulse-lengths were chosen to minimize the proton and Nitrogen-14 ESEEM in this system (*119*).

The pulse separations, τ_1, τ_2, were 200 and 1400 ns, respectively, and the echo signal was integrated using a video amplifier bandwidth of 20 MHz. The pump pulse was stepped out by 10 ns for a total of 128 points in T. In order to reduce the proton-ESEEM, the τ_1 separation was also stepped out by 16 ns (which is 25% of the proton-ESEEM modulation period) for a total of four data points (*120*). The final PELDOR signal was summed up from the signal at each of the four τ_1 values. The T = 0 value was carefully calibrated using a nitroxide biradical sample.

2.4 RESULTS AND DISCUSSION

A poly-proline peptide, shown in Figure 2-1a, with a sequence of PHGGGPPPHGGGW with two Cu^{2+} binding PHGGGW sequence was used for the experiments (*119*). Figure 2-1b shows the field-swept echo-detected ESR signal from the poly-proline peptide, obtained using a $\pi/2$ - τ - π sequence (*121*). The line shape is characteristic of an axially symmetric g-tensor (electron spin-1/2) with hyperfine splitting from the nuclei of spin-3/2. These splittings are evident for the larger $A_{||}$ component and are shown by arrows in Figure 2-1b. Each "resonance-field" in the spectrum consists of contribution from an orientation (or from a set of orientations) of the magnetic field with respect to the principal axis system (PAS) of the g-tensor for each Cu^{2+} center (cf. inset to Figure 2-1b for definition of angles). To first order, and given that the electron electron dipolar (EED) interaction is weak, the resonance field, B_{res}, for an orientation β_i (i = 1,2, cf. Figure 2-1b) is given by (*122*):

$$B_{res} = \frac{h\nu_0}{g_{\beta_i}\beta_e} - A_{\beta_i} m_I \qquad (2\text{-}1)$$

where m_I is the nuclear spin quantum number, ν_0 is the spectrometer frequency, β_e is Bohr magnetron for electrons, and $g_{\beta i}$ and $A_{\beta i}$ are defined as:

$$g_{\beta_i} = \left[g_{\perp}^2 \sin^2 \beta_i + g_{\parallel}^2 \cos^2 \beta_i \right]^{1/2}$$

and

$$A_{\beta_i} = \left[\frac{\left(A_{\parallel}^2 g_{\parallel}^2 - A_{\perp}^2 g_{\perp}^2 \right) \cos^2 \beta_i + A_{\perp}^2 g_{\perp}^2}{g_{\beta_i}^2} \right]^{1/2} \qquad (2\text{-}2)$$

where $g_{\parallel}$, $g_{\perp}$, $A_{\parallel}$, and $A_{\perp}$ are the parallel and perpendicular components of the g- and hyperfine tensors, respectively. A spectrum simulated using Equations 2-1 and 2-2 and with $g_{\parallel}$, $g_{\perp}$, $A_{\parallel}$, and $A_{\perp}$ of 2.230, 2.068, 165.0 G, and 2.0 G, respectively, is shown in Figure 2-1b.

The value of the hyperfine splitting is characteristic of Cu^{2+} coordinated to three nitrogen atoms and one oxygen atom (*119, 121*). This was confirmed by Electron Spin Echo Envelope Modulation (ESEEM) experiments (*117*) which contains peaks due to Electron Nuclear Dipolar (END) interactions with the remote ^{14}N nuclear spin of the imidazole and with the ^{14}N nuclear spin of the non-coordinated glycine residue (*118*).

Figure 2-2 shows the time domain PELDOR signal for the poly-proline peptide at four different magnetic fields. In this two-frequency experiment (*1, 100*), the detection frequency was 9.556 GHz and the pump frequency was 9.656 GHz. The separation between the detection pulse and the pump pulse was extended to 100 MHz, in order to reduce the ESEEM effects (*2*). In the experiments the modulation depth depended on the magnetic field and ranged from 0.6%-1%. The modulation depth calculated from theory is 1%-2.5% (*1*). The intramolecular dipolar modulation between the two Cu^{2+} spins is evident in the range of ~200 ns. The decay of the time domain trace is due to the intermolecular dipolar interaction between the Cu^{2+} electron spins. The total time domain signal can be expressed as (*123, 124*):

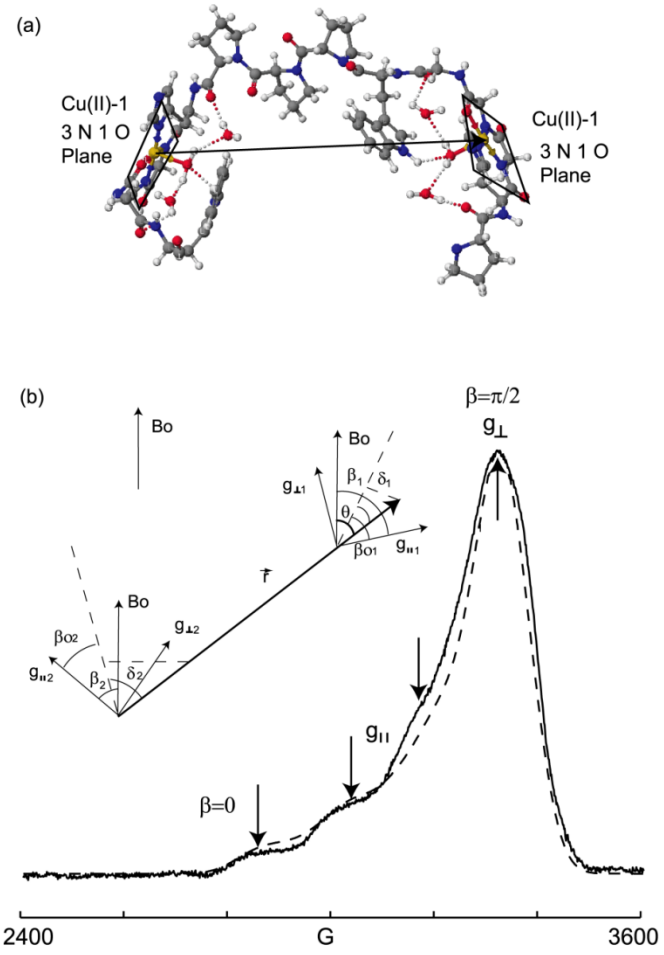

Figure 2-1. (a). The modeled structure of the Cu^{2+} binding peptide. The dipolar vector forms an angle of close to 90º with respect to the Cu^{2+} binding ligand plane (shown by rectangles). (b). Field-swept electron spin echo detected Cu^{2+}-ESR spectrum of the peptide at 20 K with a simulated spectrum shown as the dashed line. The Principal Axis System (PAS) with respect to the magnetic field and interspin vector is shown in the inset. Each spectral position corresponds to an orientation, β, (or a set of orientations), of the PAS with respect to the magnetic field. The data are consistent with Cu^{2+} binding to the PHGGGW sequence. Arrows show the larger hyperfine splitting.

$$V(t)_{total} = V(t)_{inter} V(t)_{intra} \qquad (2\text{-}3)$$

The intramolecular time domain signal at each magnetic field was obtained after a baseline correction and the resultant intramolecular time traces are shown in Figure 2-3a. The Fourier transformation of the intramolecular time domain traces are shown in Figure 2-3b at the four different magnetic fields. The PELDOR signal monitors the modulation due to the EED interaction which occurs at a frequency of (*125*):

$$\upsilon_d = \frac{\mu_0 g_a g_b \beta_e^2}{4\pi\hbar r^3}\left(3\cos^2\theta - 1\right) \qquad (2\text{-}4)$$

where μ_0 is the permeability of free space, $g_{a,b}$ are the g-factors for the electrons, r_{ab} is the Cu^{2+}–Cu^{2+} distance, and θ is the angle between the interelectron vector and the static magnetic field (cf. Figure 2-1b inset).

In general, the large anisotropy in the g-tensor can present an interesting opportunity for the case of Cu^{2+}-ESR. The experiment was obtained with detection pulses of 24 ns (π/2 pulse) and 48 ns (π pulse) and a pump pulse of 48 ns (π pulse). At a given magnetic field, the pulses "reorient" spin packets that are within a narrow bandwidth of about 41 MHz, compared to the full spectral bandwidth of ~2 GHz. Therefore, at a given magnetic field, only a subset of orientations of PAS (given by angles, δ_i, β_i), and, therefore, θ angles, are excited by the selective microwave pulses. From Figure 2-1b inset, it follows that:

$$\cos\theta_i = \cos\delta_i \cos\left(\beta_i - \beta_{0i}\right) \qquad i = 1,2 \qquad (2\text{-}5)$$

As shown in Figure 2-1b inset, for the i-th Cu^{2+} spin, β_i is the angle between the $g_{\|}$ and the external magnetic field, Bo. θ is the angle between the interspin vector and the external magnetic field, Bo. The projection of the interspin vector on the $g_{\|}$ and $g_{\perp}$ plane forms an angle

of β_{0i} with respect to the $g_{\|}$ axis. The angle between the interspin vector and its projection on the $g_{\|}$ and $g_{\perp}$ plane is defined by δ_i.

From Equations 2-1 to 2-5, it follows that the PELDOR frequency should vary with magnetic field in a fashion that depends on the angles δ_i and β_{0i}. However, the PELDOR data on the poly-proline peptide do not vary with magnetic fields (cf. Figure 2-2). The peak frequency is **~3.9** MHz.

In order to quantitatively analyze this effect, we use the theory of Maryasov, Tsvetkov and Raap (*99*). The PELDOR signal, V(T), is given by (*99*):

$$V(t_p) = \iint P(r)\xi(\theta)\langle 1 - \cos[\omega_D(1 - 3cos^2\theta) + J]t_p\rangle \sin\theta \, d\theta dr \qquad (2\text{-}6)$$

where the function $\xi(\cos\theta)$ contains information about the orientation of spins and is called the geometrical factor. The geometrical factor is given by (*99*):

$$\xi(\cos\theta) = \frac{1}{2}\sum_{m_{I1},m_{I2}}\left\langle k_{xa}^3 k_{xb}^2 \sin\phi_{1a}(1-\cos\phi_{2a})(1-\cos\phi_{3b}) + k_{xb}^3 k_{xa}^2 \sin\phi_{1b}(1-\cos\phi_{2b})(1-\cos\phi_{3a})\right\rangle_{\Phi,\delta\omega_1,\delta\omega_2}$$

$$\text{where } k_{xq} = B_{lq}/B_{rq} \qquad (2\text{-}7)$$

$$\text{and } B_{rq} = ([(\omega_{rq} - \omega_q)/\gamma^2]^2 + B_{lq}^2)^{\frac{1}{2}} \qquad (2\text{-}8)$$

in which ω_a and ω_b are the frequencies of the detection pulse and the pump pulse, respectively. B_{lq} is the amplitude of the oscillating magnetic field at frequency ω_q where q=a,b; ω_{rq} is the resonance frequency; Equation 2-8 includes the effect of inhomogeneous broadening of the ESR lines (*99*); γ is the gyromagnetic ratio for the electron; ϕ_{1a}, ϕ_{2a} and ϕ_{3b} are the rotation angles of the *i*th pulse. These rotation angles are expressed as (*99*):

$$\phi_{iq} = \gamma B_{rq} t_{pi} \qquad (2\text{-}9)$$

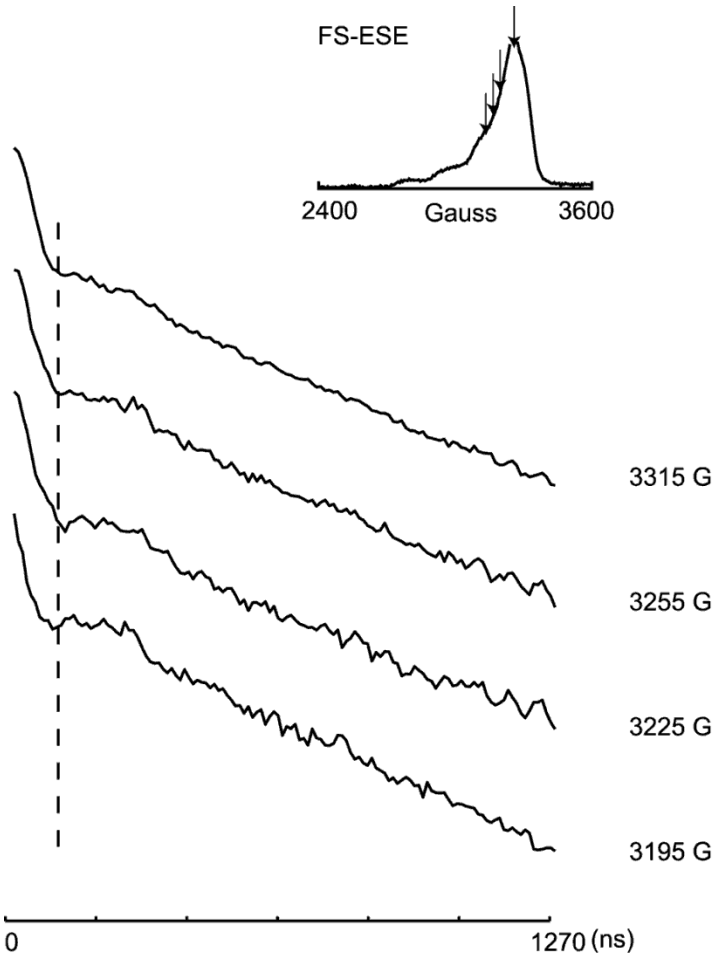

Figure 2-2. Time domain data of the Cu^{2+}-PELDOR spectra. The magnetic fields used are indicated by arrows on the FS-ESE spectrum, which is shown in the inset. The fast modulation in the time domain is from proton-ESEEM.

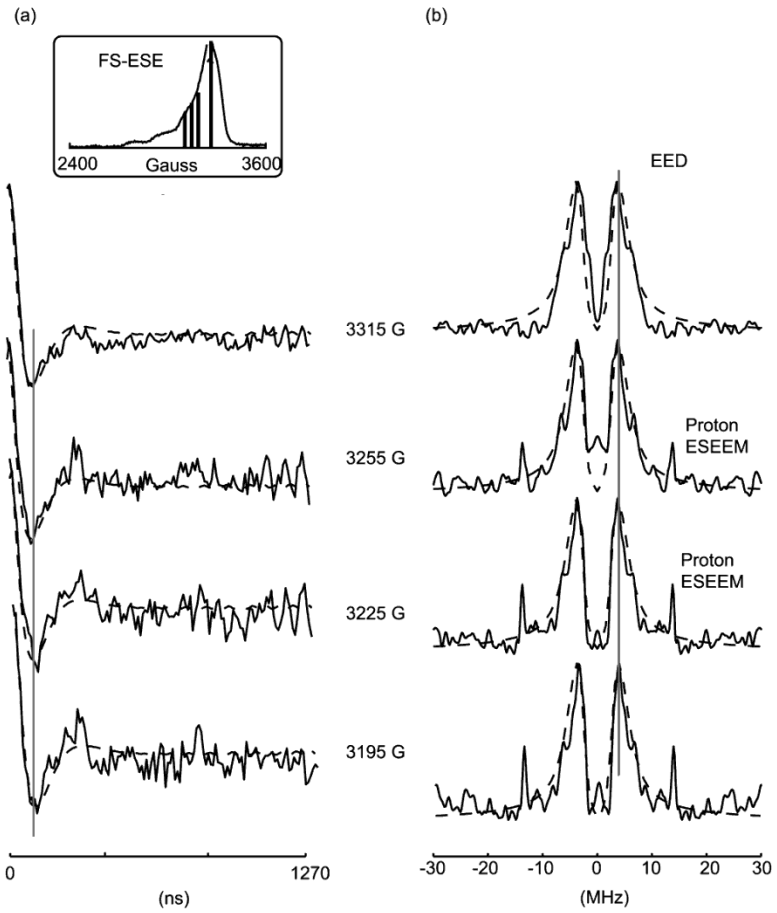

Figure 2-3. (a) The time domain signal of Cu^{2+}-PELDOR after baseline correction. The positions of magnetic fields used are shown on the Field Swept Cu^{2+}-ESE spectrum in the inset. The period of the dipolar modulation of the time domain is similar at each magnetic field. (b) The Fourier transformation of the baseline corrected time domain signal. At each magnetic field, the dominant frequency peak appears at ~3.9 MHz. The 14.8 MHz peak is from proton-ESEEM.

If all orientations are excited, as is substantially the case for nitroxides (*99*), the orientation factor is practically uniform for all values of cos(θ) and a characteristic Pake pattern results (*126*). In the Pake pattern, the frequency corresponding to θ = 90° dominates (cf. Equation 2-4), due to the greater probability of the presence of molecules with θ = 90° in the powder sample.

The presence of finite pulse-lengths, and large g-and hyperfine anisotropies, as in Cu^{2+} can lead to large orientation effects. Figures 2-4a and b show the simulated geometrical factor, $\xi(\cos\theta)$ and PELDOR spectrum, based on Equations 2-6 and 2-7, respectively. In these simulations, a single Cu^{2+}–Cu^{2+} distance is selected as 2.2 nm. The orientations of the principle axis systems for the two Cu^{2+} centers were set at $\beta_{01}=\beta_{02}=0°$, $\delta_1=\delta_2=0°$. δ_i was chosen as 0º since in this case the orientational selectivity of the PELDOR spectrum is the maximum. Only β_{0i} values of 0º are shown in Figure 2-4. Similar results were obtained with other β_{0i} values. At the magnetic field of 2900 G, the simulated DEER spectrum consists of a single peak at 4.1 MHz. Non-selective excitation would have yielded a Pake pattern with a dominant θ = 90° peak of 4.8 MHz (from Equation 2-4 with θ = 90° and r = 2.2 nm). The results can be rationalized from the geometrical factor, $\xi(\cos\theta)$. At this magnetic field and with $\beta_{01}=\beta_{02}=\delta_1=\delta_2=0°$, the geometrical factor peaks at θ~38° (cf. Figures 2-4a and b), which from Equation 2-4 leads to a frequency ~4.1 MHz in the DEER spectrum.

Figures 2-4c and d illustrate the orientational selectivity imparted by the choice of magnetic fields. At a magnetic field of 3000 G, the geometrical function is bimodal with peaks at θ ~ 30° and at θ ~53° which leads to frequencies of 6.1, 0.4 MHz in Equation 2-4. The simulated DEER spectrum based on Equation 2-7 yields peaks at 6.1 and 0.4 MHz. At a 3100 Gauss magnetic field, orientations with θ ~ 10°, 51°, and 68° are predominantly excited, which

corresponds to frequencies of 9.3, 0.9 and 2.8 MHz. From the simulated Pake pattern, the same frequency peaks were obtained. Finally, at 3200 Gauss orientation with θ centered at 50°, 73° and 80° are excited. The distribution between 73°- 80° generates a broad peak around 4.8 MHz while a peak at 0.9 MHz results from excitation of θ~50°. Therefore, theoretically, when δ~0°, there is strong orientational selectivity on the Cu^{2+}-PELDOR spectra, at X-band. Different DEER spectra are anticipated at different magnetic field.

The magnetic field dependence of PELDOR frequency persists even in the presence of a distribution in distances. Figure 2-5 shows simulated PELDOR spectra, based on Equation 2-6 for different values of magnetic field in the presence of a distribution of distances. A Gaussian distribution function with a mean distance of 2.2 nm and a standard deviation of 0.3 nm was used. The orientations were held at $\beta_{01}=\beta_{02}=135°$, $\delta_1=\delta_2=0°$. The PELDOR spectrum changes with magnetic field and the prominent frequency changes from 1.4 MHz to 4.1 MHz. However, this effect will be subtle in the presence of noise.

The results indicate that the presence of substantial g and hyperfine anisotropies leads to the excitation of only certain orientation at a given magnetic field when δ_i~0°. The PELDOR spectrum deviates from a simple Pake pattern and should vary with different magnetic field.

However, the orientational selectivity is washed out when δ_i approaches to 90°, as is evident from Equation 2-5. Under this condition, only the orientation with θ~90° are excited, and these features dominate the PELDOR spectrum. (Simulation data not shown).

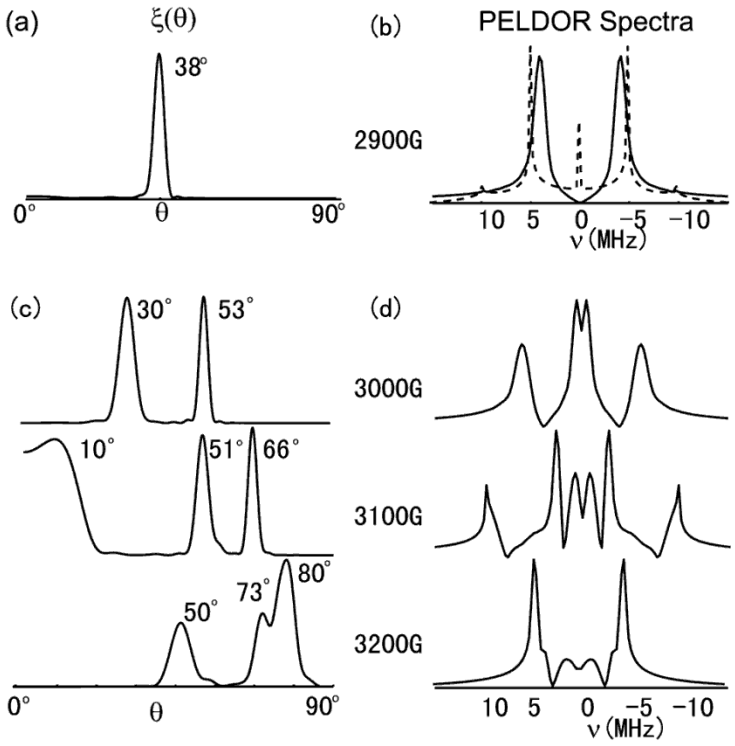

Figure 2-4. (a) The geometrical factor calculated using Equation 2-6 for $\beta_{01}=\beta_{02}=0^o$, $\delta1=\delta2=0^o$, r=2.2 nm and B_0=2900 G is shown. The plot indicates that at this magnetic field and for these parameters, only $\theta\sim 38^o$ orientations are excited by the selective pulses. (b) The simulated PELDOR spectrum consequently yields a frequency of 4.1 MHz (solid line). Non-selective excitation would yield a Pake pattern with a dominant peak at 4.8 MHz (dashed line). (c) The simulated geometrical factor with the same parameters but at three different magnetic fields is shown. These results indicate that the θ angles are different at different magnetic field. Therefore, the resultant PELDOR spectrum varies with magnetic field. (d) The simulated PELDOR spectra based on Equation 2-7 at three magnetic fields are shown. Such orientational effects are reduced when $\delta_1\sim90°$ and $\delta_2\sim90°$.

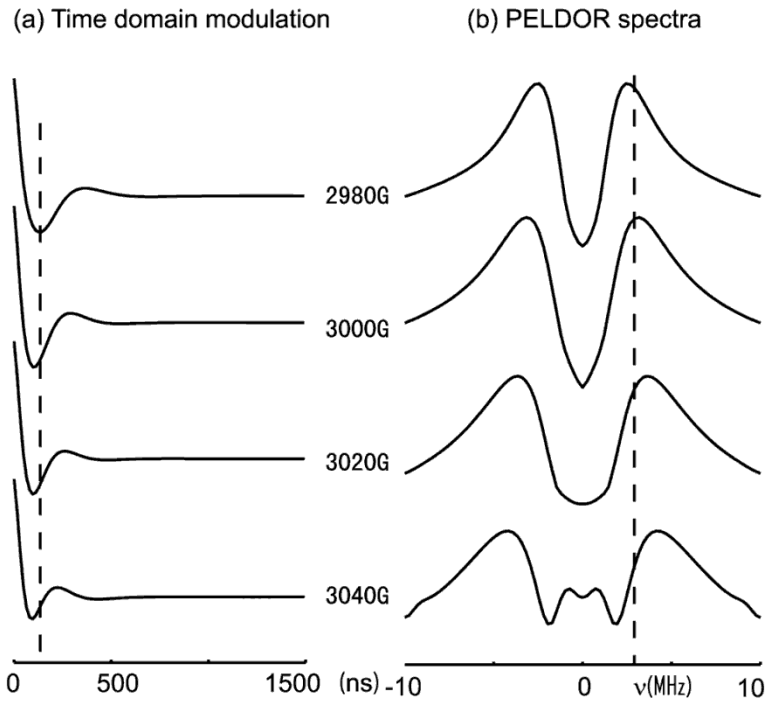

Figure 2-5. The magnetic field dependence of PELDOR frequency persists even in the presence of a distribution in distances. (a) Simulated time domain signal and (b) the spectra at 2980 G, 3000 G, 3020 G and 3040 G, with $\beta_{01}=\beta_{02}=135°$, $\delta_1=\delta_2=0°$. The interspin distance is held at 2.2 nm and a standard Gaussian distance distribution is used as 0.3 nm. The frequency shifts from 1.4 MHz to 4.1 MHz. Such orientational effects are reduced when δ_1~90° and δ_2~90°.

The field-independence of experimental data (shown in Figures 2-2 and 2-3) is possibly due to the combination of two effects. First, the orientation effects of Cu^{2+} electron spin are washed out by the flexibility of the peptide, which yields a large distribution in Cu^{2+}–Cu^{2+} distances. Second, for this poly-proline peptide the Cu^{2+} δ_1 and δ_2 may be close to 90°. The modeled structure of the Cu^{2+} binding peptide is shown in Figure 2-1a (*117*). The dipolar vector forms an angle of close to 90º with respect to the Cu^{2+} binding ligand plane. The angles between the Cu^{2+}–Cu^{2+} dipolar vector and each Cu^{2+} binding ligand (3 N 1 O) for the first Cu^{2+} are 82º, 118º, 92º and 84º. The angles between the Cu^{2+}–Cu^{2+} dipolar vector and each Cu^{2+} binding ligand (3 N 1 O) for the second Cu^{2+} are 110º, 81º, 75º and 106º. Therefore, the dipolar vector could form an angle of close to 90° with respect to the Cu^{2+} g-tensor plane. With the internal orientation that δ_1 and $\delta_2 \sim 90°$, the best fits were obtained with a Gaussian distribution of distances with an average interspin distance of 2.1-2.2 nm and a standard deviation of 0.3 nm. Similar results were obtained for any β_{0i} value. The resulted time traces and PELDOR spectra are shown by dashed lines in Figure 2-3. Double Quantum Coherence ESR results measured a distance of 2.0 nm on the same peptide (*117*). The δ_i values estimated from this work are consistent with the assumption made by Huber and coworkers in their metalloprotein (*116*).

For a general Cu^{2+}-based sample, however, the relative orientation of the two Cu^{2+} g-tensors may not be the same as in the case of the poly-proline peptide used in this work. Therefore, even in the presence of a distance distribution, strong orientational selectivity is still expected in the experimental data. This matter warrants more attention in the future.

Large distance measurements on spin labeled macromolecules have opened up the use of ESR to measure global folding patterns of proteins, nucleic acids, and flexibility of polymers.

Extension of this methodology to paramagnetic metals is likely to have a similar impact on the measurement of structure function relationships in metalloproteins.

2.5 SUMMARY

In this work, we present the Cu^{2+}-PELDOR spectra at four magnetic fields, at X-band. We found that the Cu^{2+}-PELDOR spectra do not vary with magnetic field. However, theory predicts that the Cu^{2+}-PELDOR spectra should vary strongly with magnetic field. We explained this magnetic field independency by the combination of two possible effects. First, the flexibility of the model peptide washes out the orientational selectivity of the Cu^{2+}-PELDOR spectra. Second, the Cu^{2+} g-tensor in our model peptide is in a specific orientation with respect to the interspin vector (cf. Figure 2-1a)- at these orientations the PELDOR data are expected to be field independent from theory. The combination of large flexibility and mutual orientations reduces the suitability of poly-proline based systems to monitor orientational effects in these experiments. However, the simulations indicate that, in general, the orientation effects are important for obtaining accurate Cu^{2+}–Cu^{2+} distance using PELDOR, and field dependent data should be acquired and analyzed as discussed in this work.

2.6 ACKNOWLEDGMENT

This work was supported by an NSF CAREER grant (MCB 0346898). The help of Dr. Soraya Pornsuwan with initial data analysis is gratefully acknowledged.

3.0 AN UNDERSTANDING OF ORIENTATIONAL EFFECTS ON COPPER ION–BASED DOUBLE ELECTRON ELECTRON RESONANCE

This work, written in collaboration with Drew Kise and Sunil Saxena, has been published in the Journal of Physical Chemistry B, 2010, V.114, pages 6165-6174 (51).

3.1 ABSTRACT

We present the measurement of Cu^{2+}–Cu^{2+} and Cu^{2+}–nitroxide distance distributions using double electron-electron resonance (DEER) on a proline-based peptide and an alanine-based peptide. The proline-based peptide contains two well-characterized Cu^{2+} binding segments, PHGGGW, separated by seven proline residues. The alanine-based peptide contains a PHGGGW segment at one end of the peptide and a nitroxide spin label attached to a cysteine residue close to the other end of the peptide. DEER experiments were performed at several external magnetic fields and resonance offsets to probe the orientational effects on the Cu^{2+}-based DEER signal. Subtle but detectable orientational effects were observed from the DEER spectra of both peptides. A general theoretical model was developed to analyze the experimental data sets. We show that the Tikhonov regularization-based method is not applicable to extract precise Cu^{2+}-based distance distributions. Instead, a full data analysis is required to obtain the distance distributions

and relative orientations between spin centers. A 30 Å mean Cu^{2+}–Cu^{2+} distance and a 27 Å mean Cu^{2+}–nitroxide distance were determined in the two peptides. These distances are consistent with structural models and with earlier measurements. Constraints on the relative orientation between paramagnetic centers in these two model peptides were determined by examination of the orientational effects. The data analysis procedure is system independent, and therefore is applicable to more complicated biological systems.

3.2 INTRODUCTION

Double electron electron resonance (DEER) (*1, 2, 101, 127, 128*) has become a powerful approach to measure interspin distance distributions in the range of 2-8 nm. The distribution of distances provides valuable structural information in order to probe the structure and dynamics of soluble proteins (*7-20*), DNA and RNA (*21-26*) and oligomers (*27-34*). The DEER technique is attractive because they can provide distance constraints even in membrane proteins (*35-47*) and large biomolecular complexes (*12, 48, 49*). The paramagnetic centers employed are mostly nitroxide spin-labels, which are covalently attached to a cysteine residue in a biomolecule by site-directed spin labeling (*4, 58, 60*). Nitroxide–nitroxide distance distributions can be precisely determined by utilizing an inversion technique based on Tikhonov regularization (*5, 6*). Recently, paramagnetic metal ions have also been employed as the spin centers (*5, 7, 8, 50, 52-56*). The data analysis procedures for metal ion centers, on the other hand, are still under development.

In principle, the selective microwave pulses applied in the DEER experiment excite only a small portion of the ESR spectrum. This partial selectivity of the ESR spectrum can impart the

so-called “orientational selectivity” on the DEER signal. For the case of nitroxide spin labels, the distance distribution can often be resolved by using an inversion technique based on Tikhonov regularization (*5, 6*). The Tikhonov regularization method extracts the distance distribution by solving a Fredholm equation containing a kernel that is readily available from theory. The kernel for nitroxide spin labels is simplified since effects due to relative orientations of the two spin centers are typically randomized, due to the large inherent flexibility of the spin labels (*5, 6*). However, in some specific cases, the nitroxide orientational selectivity can be observed (*2*). For instance, Prisner and coworkers observed a frequency offset dependence on the nitroxide-based DEER signal in the potassium ion channel, KcsA, even at X-band (*129*)**.** In this protein, the nitroxide spin labels were orientationally restricted due to the tertiary interaction. Such strong restriction of the nitroxide spin labels in the membrane protein made the Tikhonov regularization-based method problematic in extracting nitroxide–nitroxide distances. Instead, a full analysis of these frequency offset dependent DEER data was required. By using a molecular model, Prisner and coworkers were able to resolve not only the nitroxide–nitroxide distances but also the orientations of nitroxide spin labels at X-band (*129*). Orientational effects on nitroxide-based DEER signal also becomes more significant at higher resonance frequencies, where a full data analysis procedure is also required to obtain information on distances as well as the relative orientation of spin labels (*114, 115*).

For the case of paramagnetic metal ions such as Cu^{2+}, the importance of accounting for orientational effects has been noticed by us as well as other research groups (*7, 50, 52-54*). In most of these works, DEER data were collected at several magnetic fields and/or frequency offsets, and distances were measured by an analysis based on an appropriate theoretical model. In an elegant contribution from Prisner and coworkers, a procedure was developed for a model

compound where the Cu^{2+} and the spin label were separated by a fairly rigid linker (*53*). In a more recent work, Lovett *et. al.* developed another procedure to extract the distance as well as the relative orientation between two Cu^{2+} in a dicopper complex (*54*). In both cases, the structural information such as the location, the electron spin density delocalization, the orientation of each spin center, and the flexibility of the linker between spin centers could be estimated by X-ray diffraction measurements and/or DFT calculations. The availability of such structural information simplified the data analysis procedures. These works were important in establishing the role of the spin density delocalization in Cu^{2+}-based distances. Based on the understanding obtained by these works, we sought to develop a more general analysis procedure that can be applicable to an unknown sample or a more complicated biomolecules, where DFT calculations are not accessible.

The key step to make our procedure general is to use a molecular model, wherein the relative orientation of the principal axes system of the two spin centers was described by three Euler angles; - these angles were allowed to have a distribution. No structural information regarding the linker between the spin centers, or the precise distance, is required to analyze the DEER signal, which therefore ensures that this model is system independent. The model was tested on two synthetic peptides, one with Cu^{2+} bound to both ends of the peptide and the other with one Cu^{2+} bound to one end and one nitroxide attached to the other end of the peptide. Experimental DEER data showed only very subtle frequency offset dependence for the alanine-based peptide. Detectable magnetic field dependence was observed for the proline-based peptide data sets. These data sets were analyzed using our model, wherein both spin-spin distance distributions and relative orientations between spin centers were determined for the two peptides. These parameters were consistent with results of molecular modeling (*117, 130-132*). The

success of the present analysis procedure indicates that our model can be applied to more complicated biological systems.

3.3 MATERIALS AND METHODS

Theory. DEER data can be orientational selective due to the mechanism by which DEER measures the dipolar interaction. Given that 4-pulse DEER and 3-pulse DEER share the same mechanism, the 3-pulse DEER pulse sequence alone will be used to discuss the mechanism, even though all experimental data shown in this work were collected using the DEER sequence. In 3-pulse DEER, the $(\pi/2)_{\upsilon_1} - \tau - (\pi)_{\upsilon_1}$ sequence at the frequency of υ_1 generates a primary echo at time τ after the $(\pi)_{\upsilon_1}$ pulse. Only electrons resonant with frequency υ_1 (spin A) contribute to the primary echo. The pump $(\pi)_{\upsilon_2}$ pulse applied at time t_p after the $(\pi/2)_{\upsilon_1}$ pulse inverses the magnetization of electrons resonant with frequency υ_2 (spin B). This causes the inversion of the local magnetic field generated by spin B at the location of spin A. The local magnetic field that spin A experiences is proportional to the dipolar interaction between spin A and B, providing sensitivity to the distance between spin A and B. To measure the dipolar frequency, the t_p interval is incremented by a certain stepsize. The dipolar interaction, ω_{dd}, is

$$\omega_{dd} = -\frac{\mu_0 \mu_B^2}{4\pi\hbar}\frac{g_1 g_2}{r^3}(3\cos\theta^2 - 1) \qquad (3\text{-}1)$$

In Equation 3-1, μ_B is the Bohr magneton, g_1 and g_2 are the g-values of the coupled electron spins, $\hbar$ is the Planck constant divided by 2π, r is the spin-spin distance, θ is the angle between the spin-spin vector and the external magnetic field, and μ_0 is the vacuum permeability. The spectral frequency as shown in Equation 3-1 depends on r and the θ angles that are excited. For

the case of nitroxide spin labels, the relative orientations of the two spins are randomized due to the inherent flexibility of the spin label. The microwave pulses used in DEER experiments, therefore, can uniformly excite most of the θ values. A characteristic spectrum known as the Pake pattern is measured (cf. Figure 3-1a) (*126*). In a Pake pattern, the frequency peak corresponding to the θ of 90° dominates since in a powder sample there are more spin-spin vectors with a θ of 90° with respect to the magnetic field than other angles. The Tikhonov method with a simplified kernel can then be used to measure distance distributions. For the cases of higher resonance frequencies (*114, 115*) (>90 GHz), restricted label motions (*129*), or Cu^{2+}-based DEER experiments, this approach to extract interspin distances can be questionable.

The large g and hyperfine anisotropies of the Cu^{2+} electron spin broaden the Cu^{2+} ESR spectrum to ~2 GHz, compared with a 200 MHz nitroxide ESR spectrum (cf. Figure 3-1). The coverage of microwave pulses used in the PELDOR experiments is typically ~20-50 MHz, and thus only a small portion of the Cu^{2+} ESR spectrum is excited (cf. Figure 3-1b and below). The high-field part of X-band Cu^{2+} spectrum is highly disordered because of interplay of g and A anisotropies, in combination with I=3/2. Therefore, in the experimental setup, if both the observation and pumping frequencies excite the high-field part of the spectrum (which is essentially the case of most of our data collection), the range of angles θ contributing to DEER effect is expected to be rather broad. The orientational selectivity effects are expected to be not very strong, but they may still affect the resultant DEER spectrum. Consequently the spectrum may differ from a Pake pattern (cf. Figure 3-1b). The excited θ angles are in general unknown and dependent on the relative orientation of the two spin centers. The distance between Cu^{2+} centers cannot be extracted using the Tikhonov method with a simplified kernel (cf. Figure 3-1b), but becomes dependent on the θ excitation profile. The θ excitation profile can be

quantitatively analyzed as follows (*133*). In the rotating frame, the off-resonance magnetic field in the z direction is denoted by Ω. The amplitude of the microwave pulse applied along the +x direction is B_1. During the pulse, the effective magnetic field the electron spin experiences, B_{eff}, is the vector sum of B_1 and Ω. The initial magnetization, which is along with the z-axis, is rotated by an angle of β_{eff} around B_{eff} axis. The magnetization after this pulse is (*133*)

$$\begin{pmatrix} M_x \\ M_y \\ M_z \end{pmatrix} = R_y^{-1}(\alpha) R_z(\beta_{eff}) R_y(\alpha) \begin{pmatrix} 0 \\ 0 \\ M_0 \end{pmatrix} = \begin{pmatrix} M_0 \sin\alpha \cos\alpha \cos\beta_{eff} - M_0 \sin\alpha \cos\alpha \\ M_0 \sin\alpha \sin\beta_{eff} \\ M_0 \sin\alpha \sin\alpha \cos\beta_{eff} + M_0 \cos\alpha \cos\alpha \end{pmatrix}$$

(3-2)

where β_{eff} is the effective flip angle, α is the angle between the external magnetic field and B_{eff}. For spins that are off-resonance, the $(\pi/2)_{\upsilon_1}$ pulse provides a factor of $\sin\alpha_1 \sin\beta_{eff,1}$ (cf. M_y term of Equation 3-2. Subscript "1" corresponds to the $(\pi/2)_{\upsilon_1}$ pulse in the PELDOR sequence) to the total magnetization. The $(\pi)_{\upsilon_1}$ pulse provides another factor of $M_0 \sin\alpha_2 \sin\alpha_2 \cos\beta_{eff,2} + M_0 \cos\alpha_2 \cos\alpha_2$ (cf. M_z term of Equation 3-2. Subscript "2" corresponds to the $(\pi)_{\upsilon_1}$ pulse in the PELDOR sequence) to the total magnetization. In the υ_2 frequency, spin Bs are not uniformly flipped 180° by the $(\pi)_{\upsilon_2}$ pulse as intended. This $(\pi)_{\upsilon_2}$ pulse adds a factor of $M_0 \sin\alpha_2 \sin\alpha_2 (1 - \cos\beta_{eff,3})$ to the total DEER signal, which corresponds to a change in the z component of the magnetization. Therefore, besides the magnetic dipolar term, an additional factor is introduced to the final PELDOR signal,

$$\xi = \sin\alpha_1 \sin\beta_{eff,1} \sin\alpha_1 \sin\alpha_1 (1 - \cos\beta_{eff,2}) \sin\alpha_2 \sin\alpha_2 (1 - \cos\beta_{eff,3}) \qquad (3\text{-}3)$$

where ξ is a factor that accounts for the orientational effects on the PELDOR signal.

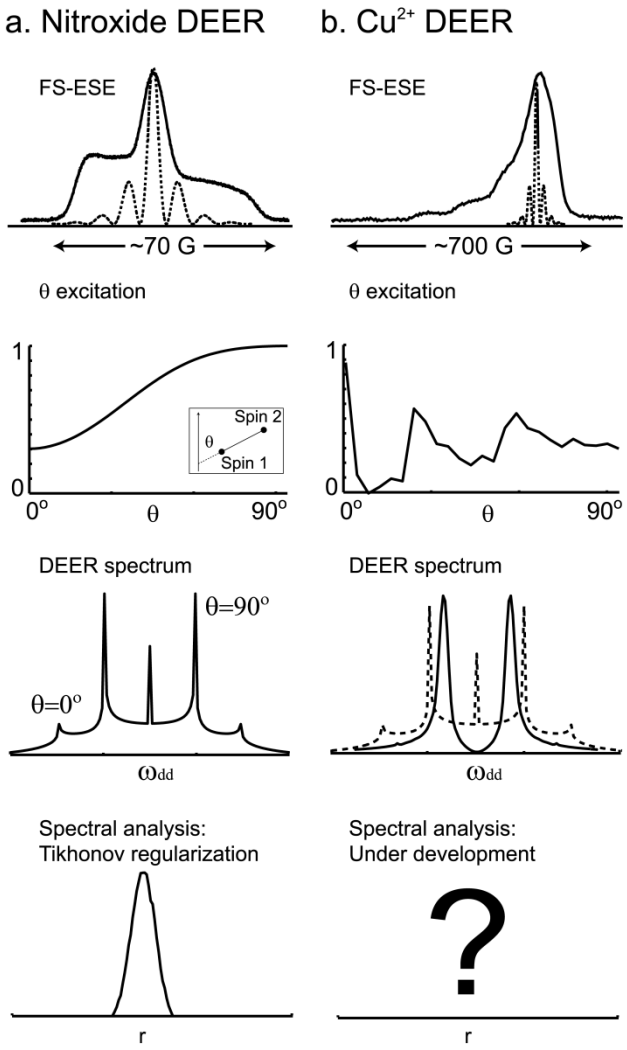

Figure 3-1. The field-swept electron spin echo (FS-ESE) spectrum, simulated θ excitation profile and simulated DEER spectrum for a nitroxide sample (a) and a Cu^{2+} sample (b), respectively. The coverage of the microwave pulse used in DEER is shown by the dashed line in both figures. For the case of nitroxide, most θ angles are excited resulting in the familiar Pake pattern shown in (a). For the case of Cu^{2+}, however, the θ excitation profile is not uniform and therefore the measured DEER spectrum differs from the Pake pattern (b).

Based on Equation 3-3, the orientational effects on the PELDOR signal is a result of the off-resonance effects, which depend on the difference between the local magnetic field an electron spin experiences and the external magnetic field. For the case of flexible nitroxide spin labels, wherein the inherent flexibility of the spin label largely randomizes the relative orientation of the spin labels, the local magnetic field experienced by a nitroxide spin label is randomized. The off-resonance term is close to 0, resulting in the α_1 and α_2 close to 90°; $\beta_{eff,1}$ close to 90°; $\beta_{eff,2}$ and $\beta_{eff,3}$ close to 180°. The geometrical factor is uniform with all θ angles. The kernel function utilized in the Tikhonov regularization method can be simplified to (*5*)

$$K(t_p, r) = \int \langle 1 - \cos[\omega_D(1 - 3cos^2\theta) + J]t_p \rangle d\theta \qquad (3\text{-}4)$$

and the DEER signal, in the presence of a distribution, is

$$V(t_p) = \int K(t_p, r) P(r) \sin\theta \, d\theta \qquad (3\text{-}5)$$

where P(r) is the distance distribution function. For the case of restricted nitroxide spin labels (*129*), the relative orientation of spin centers is rigid. The local magnetic field that a spin label experienced is not randomized but dependent on the resonance offset and magnetic field where the data was collected, leading to a non-zero off-resonance term. For the case of Cu^{2+}, due to the larger anisotropies of the Cu^{2+} spin center, the off-resonance term becomes comparable to the amplitude of B_1, which makes Equation 3-3 non-uniform, but generates a θ excitation profile (*50*). Equation 3-3 is essentially the same as the geometrical factor derived by Maryasov *et. al.* (*99*). They showed that

$$\sin\alpha_1 = \frac{w_1}{\sqrt{(\omega_{r1} - w_1)^2 + w_1^2}} \qquad (3\text{-}6)$$

where $\omega_{r1} = \frac{\beta B_0 g_{eff} + m_I A_{eff} + \delta\omega_1}{\frac{h}{2\pi}}$, g_{eff} is the effective g value, A_{eff} is the effective hyperfine value and $\delta\omega_1$ illustrates the inhomogeneous broadening. Similarly,

$$\sin\alpha_2 = \frac{w_2}{\sqrt{(\omega_{r2}-w_2)^2+w_2^2}}, \quad (3\text{-}7)$$

$$\beta_{eff,1} = \sqrt{(\omega_{r1}-w_1)^2 + B_1^2}\; t_{p,1}, \quad (3\text{-}8)$$

$$\beta_{eff,2} = \sqrt{(\omega_{r2}-w_2)^2 + B_2^2}\; t_{p,2}, \quad (3\text{-}9)$$

$$\beta_{eff,3} = \sqrt{(\omega_{r2}-w_2)^2 + B_2^2}\; t_{p,3} \quad (3\text{-}10)$$

Detailed explanations of each term in the geometrical factor can be found in previous works (*50, 99*). The geometrical factor depends on the resonance offset, the external magnetic field, the anisotropy of the electron spin species and the internal orientations of the two spin centers. To account for the orientational effects, the total DEER signal can be expressed as (*99*)

$$V(t_p) = \iint P(r)\xi(\theta)\langle 1-\cos[\omega_D(1-3cos^2\theta)+J]t_p\rangle \sin\theta\, d\theta dr \quad (3\text{-}11)$$

where

$$\xi(\theta) = \frac{1}{2}\sum_{m_{I1},m_{I2}} \langle k_{xa}^3 k_{xb}^2 \sin\phi_{1a}(1-\cos\phi_{2a})(1-\cos\phi_{3b})$$

$$+ k_{xb}^3 k_{xa}^2 \sin\phi_{1b}(1-\cos\phi_{2b})(1-\cos\phi_{3a})\rangle_{\Phi,\delta\omega_1,\delta\omega_2}$$

is the full expression of the geometrical factor; P(r) is the probability of distances. A comparison of Equation 3-5 and 3-11 indicates that, in the case of large off-resonance effects, the kernel utilized to extract distance distributions between spin centers cannot be simplified to the form shown by Equation 3-4. To extract precise Cu^{2+}-based spin-spin distances and relative orientations between spin centers, both the interspin distance and the geometrical factor need to be considered in the data analysis procedure.

The molecular model. The model is illustrated using the proline-based peptide which contains two copper centers. The g-tensor of the Cu^{2+} close to the N-terminus of the peptide (also referred to as the first Cu^{2+} in this work) was chosen to be the reference frame (cf. Figure 3-2) (*119*, *134*). The Cu^{2+} center in the C-terminus of the peptide can also be used as the reference frame. This will not affect the molecular model, the fitting procedure and the relative orientation between the two Cu^{2+} centers. The relative position between the two copper atoms was described by a vector, R, and an angle, χ (cf. Figure 3-2). The relative orientation of the two Cu^{2+} g-tensors was described by two Euler angles, γ and η. Only 3 angles are required to describe the geometry of the two spin centers because of the axial symmetry of the Cu^{2+} principal axes system. The geometrical factor as shown in Equation 3-11 depends only on the relative orientation between the principal axes system of the two spin centers. Therefore, the definition of the reference frame generates no ambiguity. To account for the flexibility of the peptide, the position of each copper atom in this model was assumed to be localized randomly within a spherical region. The radius of the sphere was denoted as ΔR. The angles χ, γ, and η were also assumed to be flexible within certain ranges.

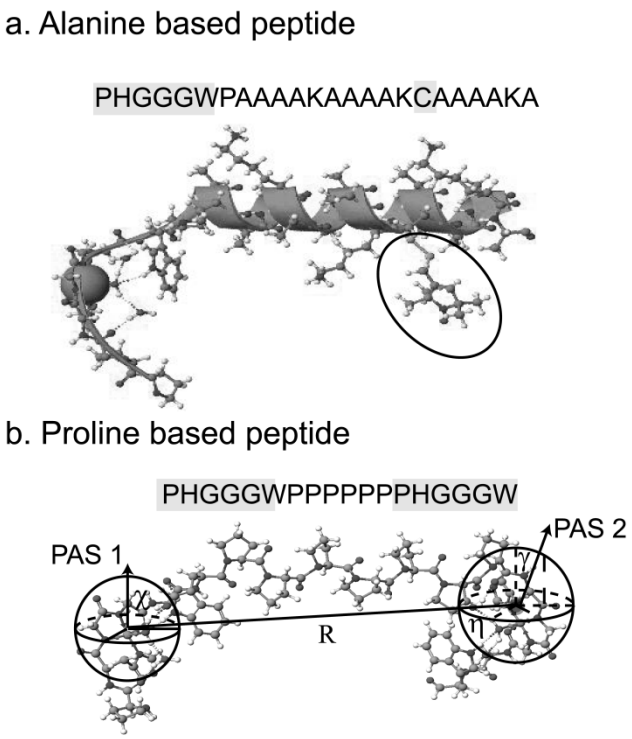

Figure 3-2. (a) The molecular structure of the alanine-based peptide, as adapted from Jun *et. al.*, *Biochemistry* 2006, *45*, 11666. The Cu^{2+} center is highlighted using the space-filling method. The nitroxide spin label is indicated by the circle. (b) The definition of the relative orientation of the two spin centers overlapped on a raw molecular structure of the proline-based peptide. This structure was built based on previous proline-based peptide work from Becker *et. al.*, *Chem. Phys. Lett.* 2005, 414, 248. The peptide sequences for both peptides are also shown.

In our approach we generated an ensemble containing 2000 different locations of the spin centers using a Monte Carlo procedure (see below). The DEER signal was calculated for each location and the 2000 signals were summed up to generate the total DEER signal. This signal depended on parameters such as the distance distribution as well as on the relative orientation. The DEER signal was compared to experiment and the parameters were varied until a good fit was reached. The whole procedure is summarized in Scheme 1.

The Monte Carlo (MC) procedure generates different positions of the copper centers as follows. In each MC step, the position of the first copper atom in the spherical coordinate system is expressed by

$$\begin{pmatrix} x_1 \\ y_1 \\ z_1 \end{pmatrix} = \begin{pmatrix} \Delta R \cdot \sin\theta_1 \cdot \cos\varphi_1 \\ \Delta R \cdot \sin\theta_1 \cdot \sin\varphi_1 \\ \Delta R \cdot \cos\theta_1 \end{pmatrix} \qquad (3\text{-}12)$$

where θ_1 is the inclination angle, describing the angle between the z-axis of the reference frame (the first spin g-tensor) and the vector connecting the center of the reference frame and the copper atom. The φ_1 angle is the azimuth angle, describing the angle between the x-axis of the reference frame and xy-plane projection of the vector connecting the center of the reference frame and the copper atom. The θ_1 was selected randomly from 0° to 180°, and φ_1 was selected randomly from 0° to 360°. Such random selection of inclination and azimuth angles ensured that the position of the first copper atom was selected randomly within the sphere. Similarly, the position of the second copper atom, (x_2, y_2, z_2) is expressed by

$$\begin{pmatrix} x_2 \\ y_2 \\ z_2 \end{pmatrix} = \begin{pmatrix} \Delta R \cdot \sin\theta_2 \cdot \cos\varphi_2 \\ \Delta R \cdot \sin\theta_2 \cdot \sin\varphi_2 \\ \Delta R \cdot \cos\theta_2 \end{pmatrix} + \begin{pmatrix} x_{2,0} \\ y_{2,0} \\ z_{2,0} \end{pmatrix} \qquad (3\text{-}13)$$

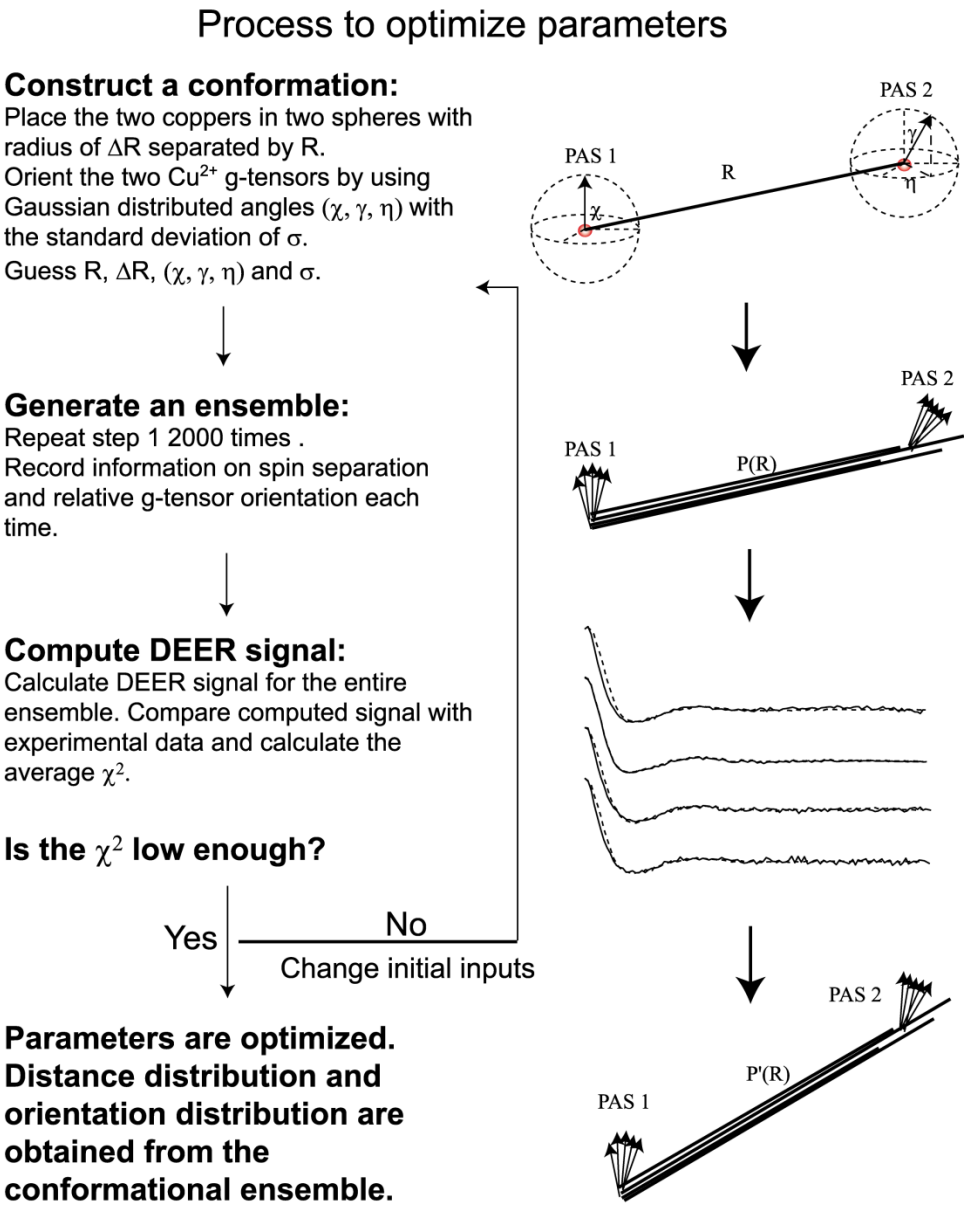

Scheme 3-1: Process in optimizing parameters in the molecular model.

where the inclination angle, θ_2, was randomly selected from 0° to 180°, and the azimuth angle, φ_2, was randomly selected from 0° to 360°. The ($x_{2,0}$, $y_{2,0}$, $z_{2,0}$) represents the center of the second Cu^{2+} sphere in the reference frame, which depends on ΔR, R, and angle χ. The χ angle was selected randomly. The probability of selecting each χ angle was assumed to be a Gaussian function, where the mean angle value was χ and the standard deviation of the χ angle was σ_χ in the simulations (*135*). Such pseudo-random selection of χ accounted for the flexibility in the χ angle. For this trajectory, by knowing the coordinates of each copper center, the interspin distance, r, can be computed with variables R, ΔR, χ and σ_χ.

As shown by Larson *et. al.* (*2*), the $g_{eff,i}$ and $A_{eff,i}$ terms in Equation 3-6 to 3-10 depend on the relative orientation between the external magnetic field and the z-axis of the Cu^{2+} g-tensors. For the first Cu^{2+} center, the external magnetic field in the Cu^{2+} g-tensor coordinate system is

$$\begin{pmatrix} B_{X,g,Cu} \\ B_{Y,g,Cu} \\ B_{Z,g,Cu} \end{pmatrix} = R(\chi) \cdot R(\theta, \varphi) \cdot \begin{pmatrix} 0 \\ 0 \\ B_0 \end{pmatrix} \tag{3-14}$$

where (θ, φ) describes the relative orientation between the external magnetic field and the interspin vector. The relative orientation between the external magnetic field and the second Cu^{2+} g-tensor is given by

$$\begin{pmatrix} B_{X,g,Cu,2} \\ B_{Y,g,Cu,2} \\ B_{Z,g,Cu,2} \end{pmatrix} = R^{-1}(\gamma, \eta) \cdot \begin{pmatrix} B_{X,g,Cu,1} \\ B_{Y,g,Cu,1} \\ B_{Z,g,Cu,1} \end{pmatrix} \tag{3-15}$$

Once the $g_{eff,i}$ and $A_{eff,i}$ terms are known, for this trajectory, the geometrical factor can be expressed with three Euler angles and their standard deviations (*2*). Similar to χ, the γ and η values were also pseudo-randomly selected, with corrreponding standard deviation of σ_γ and σ_η,

respectively. The DEER signal for this trajectory was calculated using Equation 3-11. The overall DEER signal, $V_{model}(t)$, was averaged over 2000 trajectories.

To fit the simulated signal to the experimental data, an average χ^2 value was employed to describe the goodness of the fit,

$$\chi^2 = \sum_{k=1}^{M} \frac{\sum_{i=1}^{N} \left(V_{model\ ,i}(t) - V_{exp\ ,i}(t) \right)^2}{N-1} \qquad (3\text{-}16)$$

where N represents the number of points in the DEER experiments and M is the total number of DEER data collected at different experimental conditions (i.e. the external magnetic field or resonance offset). The variables in the molecular model were varied until the lowest average χ^2 value was achieved. The optimized set of variables provided both the interspin distances and the relative orientation between Cu^{2+} centers. This model was originally developed for a Cu^{2+}- Cu^{2+} spin pair. The Cu^{2+}-nitroxide model was obtained by replacing the second Cu^{2+} center with a nitroxide spin label.

Electron spin density delocalization effects have been noticed and analyzed in several metal ion related systems (*53, 54*). These effects play a minor role in the DEER signal simulation except for the cases of strong delocalization (*54*). Nevertheless, we examined the spin density delocalization effects on our sample peptides during our analysis process. The Cu^{2+} binding centers in our model peptides display a five-center spin density distribution (the copper atom and the four binding ligands). The probability of the electron density distribution in the PHGGGW-Cu^{2+} center was determined by Larsen and coworkers (*134*) to be 64.53 % on the copper atom, 4.22 % on the δ-N of histidine, 14.45 % and 12.03 % on the amide nitrogen of the first and second glycine, respectively. There was almost no electron spin density delocalized on the equatorial oxygen. DEER signal for the case of a delocalized electron density was simulated using a procedure similar to that developed by Prisner and coworkers (*53*).

Strategy to optimize the variables in the model. Variables in the molecular model to be optimized are R, ΔR, χ, γ, η, σ_χ, σ_γ and σ_η. For an unknown model peptide, there is no information regarding the exact value of each variable. However, an estimation of the range of each variable can still be made based on properties of the sample molecules and spin centers. For instance, for both peptide sequences, the length between spin centers can be estimated to be in the range of 20 to 40 Å. The relative orientation of the two spin centers was expected to contain a similar flexibility in the direction of the x, y or z axis of the reference frame. Therefore, to a good approximation, we set $\sigma_\chi \approx \sigma_\gamma \approx \sigma_\eta$ at a value of σ. We then randomly chose values for the three angles and the standard deviation as the initial inputs and calculated the correlation of R and ΔR, by generating a contour plot of average χ^2 values in functions of R and ΔR using Equation 3-16. The lowest χ^2 value represented the best R and ΔR when the Euler angles and σ were applied at initial inputs. We then fixed R and ΔR at these optimized values, randomly chose a value for σ and varied χ, γ and η by increments of 30° ranging from 0° to 90° to calculate the average χ^2 values to find the best Euler angles. Third, we kept R, ΔR, χ, γ and η at the pre-optimized values and varied the σ value by increments of 3°, to determine the optimized standard deviation for each Euler angle. Once the Euler angles and the standard deviation were optimized, the correlation of R and ΔR were calculated again to ensure that the optimized R and ΔR values remained. If a new set of R and ΔR values were obtained, the same steps to optimize the Euler angles and standard deviations were performed again until self-consistent results were obtained.

The robustness and specificity of the optimized variables were further tested by using different initial inputs. For example, we used a different set of Euler angles to investigate the best R and ΔR values, and then optimized the angles and the standard deviation. We even tried to randomly choose the values for R and ΔR as the initial inputs and optimized the angles first, then

use the optimized angles to optimize the R and ΔR. The optimized variables were found to be unchanged for both peptides.

Sample preparations. Alanine-based peptide sample: The sequence of the alanine-based peptide is PPHGGGWPAAAAKAAAAKCAAAAKA (cf. Figure 3-2a. P, proline; H, histidine; G, glycine; W, tryptophan; A, alanine; K, lysine; C, cysteine). This peptide was synthesized at the Molecular Medicine Institute, University of Pittsburgh. The lysine residues in this peptide increase the solubility of the peptide in aqueous solutions. The PHGGGW on one end of the peptide serves as a copper binding sequence (*118, 119, 136*). The purpose of the cysteine residue close to the other end of the peptide was to covalently attach the (1-oxy-2,2,5,5-tetramethylpyrroline-3-methyl) methanethiosulfonate (MTSSL) spin label, using site-directed spin labeling (SDSL). The spin labeled alanine-based peptide was mixed with 25 mM *N*-ethylmorpholine (NEM) buffer and 25% glycerol and the pH value of the mixture was adjusted to be 7.4-7.6. The concentration of the peptide sample was 1.2 mM. Isotopically enriched $^{63}CuCl_2$ was dissolved in the same buffer as for the peptide solution with the same pH value to make the Cu^{2+} stock solution. Cu^{2+} was then mixed with the peptide solution with a 1:1 Cu^{2+}-to-peptide ratio. Based on the binding affinity of Cu^{2+} to the PHGGGW segment, more than 99% of the Cu^{2+} was bound to the peptide (*132*).

Proline-based peptide sample: The peptide sequence of the proline-based peptide is PPHGGGWPPPPPPPHGGGW. This peptide was also synthesized at the Molecular Medicine Institute, University of Pittsburgh. The proline-based peptide was mixed with 25 mM *N*-ethylmorpholine (NEM) buffer and 25% glycerol and the pH value of the mixture was adjusted to be 7.4-7.6. The concentration of the peptide sample was 1.6 mM. Isotopically enriched $^{63}CuCl_2$ was dissolved in the same buffer with the same pH value to make the Cu^{2+}

stock solution. Cu^{2+} was then mixed with the peptide solution with a 6:1 Cu^{2+}-to-peptide ratio to ensure that both PHGGGW sites were occupied by Cu^{2+}.

ESR experiments. All of the pulsed ESR experiments were performed on a Bruker Elexsys 580 spectrometer at 20 K. A MD5 resonator was used in all the experiments. The effective sample volumes for both samples were ~120 μL.

The three pulse ESEEM signals were collected by recording the stimulated electron spin echo intensity as a function of T using the sequence: (π/2)-τ-(π/2)-T-(π/2)-τ-(stimulated echo), on both peptides. The duration of the (π/2) pulses was 16 ns. The inter-pulse delay τ was fixed at 200 ns. The time interval T was incremented from 400 ns with a step size of 16 ns, for a total of 1024 points. A four step phase cycle was employed to eliminate unwanted signals (*101*).

For the DEER experiments a $(\pi/2)_{\upsilon_1}$ - τ_1 - $(\pi)_{\upsilon_1}$ - T - $(\pi)_{\upsilon_2}$ - τ_2 - $(\pi)_{\upsilon_1}$ -τ_1-echo was employed. The pulse duration of the $(\pi/2)_{\upsilon_1}$, $(\pi)_{\upsilon_1}$ and $(\pi)_{\upsilon_2}$ pulses was adjusted to be 24 ns, 48 ns and 36 ns, respectively. However, for the DEER data on the proline-based peptide at 3060 G, the pump pulse legnth was set to be 16 ns. For the alanine-based peptide, the interval T was incremented from 136 ns with a stepsize of 12 ns, for a total of 128 points. Proton modulation was averaged by adding traces at four different τ_1 values, starting at 200 ns and incrementing by 18 ns (*2*). Interval τ_2 was adjusted to make (τ_1+τ_2) =1700 ns. A two-step phase cycling (+x,-x) was carried out on the first (π/2) pulse. For the proline-based peptide at higher magnetic fields (>3230 G), the interval T was incremented from 144 ns with a stepsize of 16 ns, for a total of 128 points. At 3060 G, the stepsize applied was 10 ns, with the same number of points. A similar procedure was applied to reduce the effect from proton ESEEM as in the alanine-based peptide sample.

To measure the distance between Cu^{2+} and the spin label in the alanine-based peptide, the pump and observer pulses were placed at the nitroxide and Cu^{2+} ESR spectrum, respectively. Four different frequency offsets, 260, 364, 448 and 560 MHz, were maintained to probe the orientational effects on the DEER signal. The relative position of the pump and observer frequencies is shown in the Figure 3-3a inset. Signal collection time varied from 4 hours to 16 hours, depending on the frequency offset.

To measure the Cu^{2+}-Cu^{2+} distance in the proline-based peptide, both the pump and observer frequencies were applied to the Cu^{2+} ESR spectrum. DEER signal were collected at five different magnetic fields, 3320, 3290, 3260, 3230 and 3060 G. Signal collection time was 8 to 72 hours depending on different magnetic field. DEER signal were also collected for two different frequency offsets, 200 and 300 MHz.

3.4 RESULTS AND DISCUSSION

DEER on the alanine-based peptide. The alanine-based peptide contains a Cu^{2+} center and a nitroxide spin label. Prior to DEER experiments, the Cu^{2+} binding environment in the alanine-based peptide was confirmed by using 3-pulse electron spin echo envelop modulation (ESEEM) spectroscopy. The resultant ESEEM spectrum showed characteristic peaks due to electron nuclear dipolar interactions between the unpaired Cu^{2+} electron and ^{14}N nuclear spins from both a histidine residue and a non-coordinated glycine residue (data not shown) (*118*). These peaks are signatures of Cu^{2+} binding to the prion protein copper binding segment, PHGGGW (*119*).

The experimental DEER traces for the alanine-based peptide are shown in Figure 3-3a. The pump pulse was applied at the maximum position of the nitroxide ESR spectrum, as shown

by the dashed arrow in the inset to Figure 3-3a. The observer pulses were applied at four different resonance offsets, as indicated by the solid arrows in the inset to Figure 3-3a, that range from 260 MHz to 560 MHz. The zero time of each data set was precisely determined and illustrated by the dashed line in Figure 3-3a. A slight but noticeable modulation occurring at ~200 ns can be observed in all the data sets. The modulation depth varied in the range of 5-10 % depending on different frequency offsets (detailed values are listed on each curve). This range is comparable to theoretical values which gave a range of 7-12 % (*127*) (The slight difference is possibly caused by the inhomogeneous excitation of the mw B_1-field (*31*)). Depending on the observer frequency, the DEER data show different decaying slopes due to the intermolecular interaction. The background signal for each data set was fit by an exponential function and removed from the original data. The baseline corrected DEER traces are shown in Figure 3-3b. The differences between these DEER traces are difficult to visualize. However, a Fourier transformation of each data set shows subtle differences between different data sets in the frequency domain, indicating a weak orientational selectivity (cf. Figure 3-4). For example, the linewidth of data set with 260 MHz resonance offset is slightly narrower than the other three. Such subtle differences can not be directly used to calculate the spin-spin distance between spin centers. Quantitative analysis of the orientational effects is required.

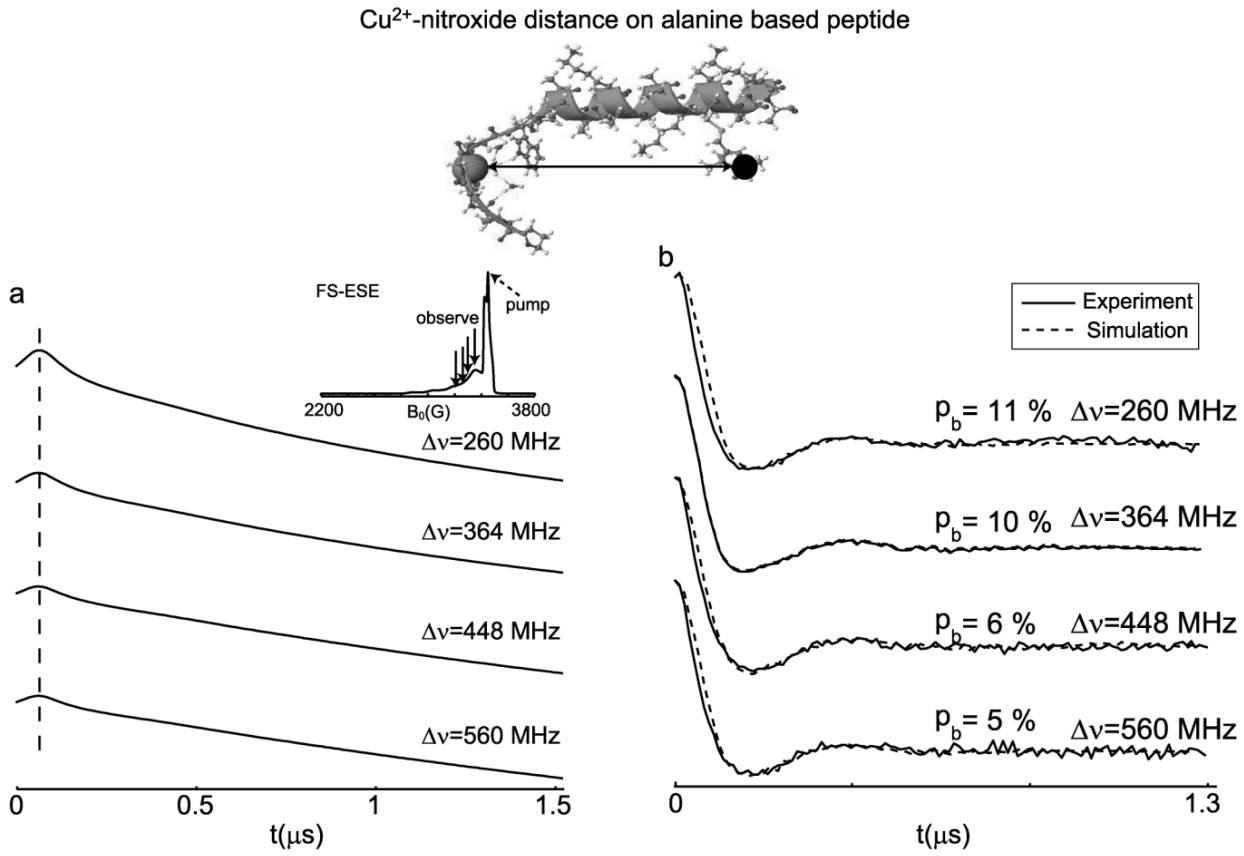

Figure 3-3. (a) Experimental DEER time domain traces for the alanine-based peptide at four different frequency offsets between 260 MHz and 560 MHz. The vertical dashed line indicates the zero time of each trace. (Inset) The FS-ESE spectrum with the pump and observer frequencies used in DEER shown by arrows. (b) DEER signal after the removal of the intermolecular decay by division of an exponential decay. A clear modulation can be observed at ~200 ns, for all the experimental data sets. These baseline corrected DEER data were fit by using the theoretical model developed in this work. Simulations are shown by dashed lines.

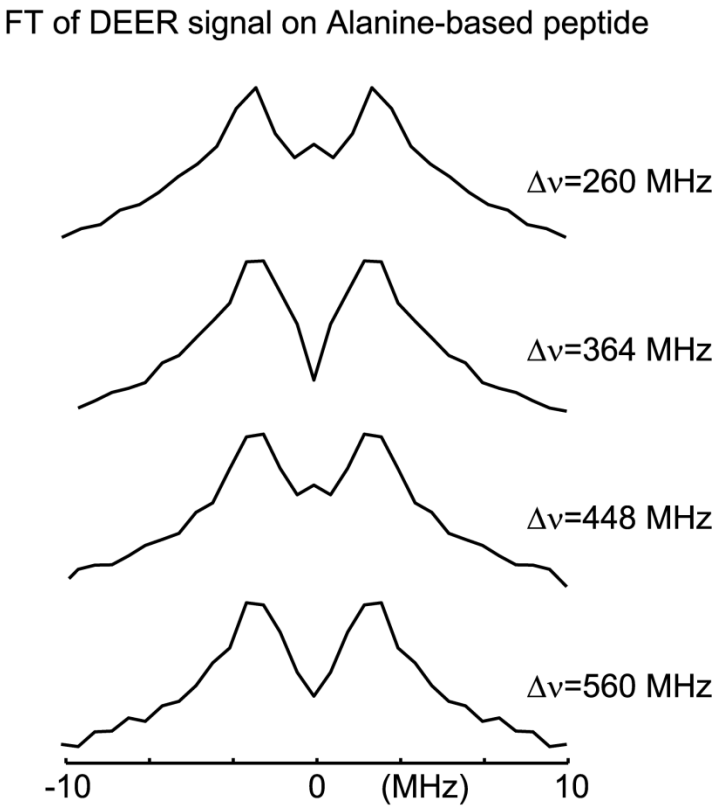

Figure 3-4. Fourier transformation of the baseline corrected experimental signal with corresponding frequency offset listed.

The alanine-based peptide was earlier used by Jun *et. al.* to measure the average distance between Cu^{2+} and the nitroxide spin label based on T_1 measurements and molecular dynamics simulations (*132*). Based on their MD model, the initial Euler angles were selected to be χ=90°, γ=0° and η=60° (*132*). A combination of the peptide backbone flexibility and nitroxide spin label flexibility creates large flexibilities in the three Euler angles. As initial inputs, we set the standard deviation at 20°. This value together with the initial Euler angle inputs were optimized later in this section. The radius of the sphere in which the nitroxide spin is located, namely $\Delta R'$, is not necessary to be the same as the Cu^{2+} sphere. Initially we set $\Delta R' = \Delta R$ and in later simulations investigated the best radius of the nitroxide sphere. Using these initial inputs, the correlation of R and ΔR was calculated and shown in Figure 3-5a. The best fit occurred at R=27 Å and ΔR=3 Å. We then fixed R andΔR at the optimized values and optimized χ, γ, η, and σ as explained in the method section. The best fit occurs at (χ, γ, η)=(90°, 30°, 30°) and σ = 9° - 12°. Lastly we varied $\Delta R'$ and ΔR in the range of 1 – 5 Å to investigate the best fit and determined that the best fit occurred at $\Delta R' = \Delta R$ = 3 Å. Most likely the flexibility of the peptide backbone is the major contributor to the flexibility in the locations of the spin centers. Using the optimized parameter set, the relative orientation between Cu^{2+} and nitroxide g-tensors can be illustrated by the black dots shown in Figure 3-5b.

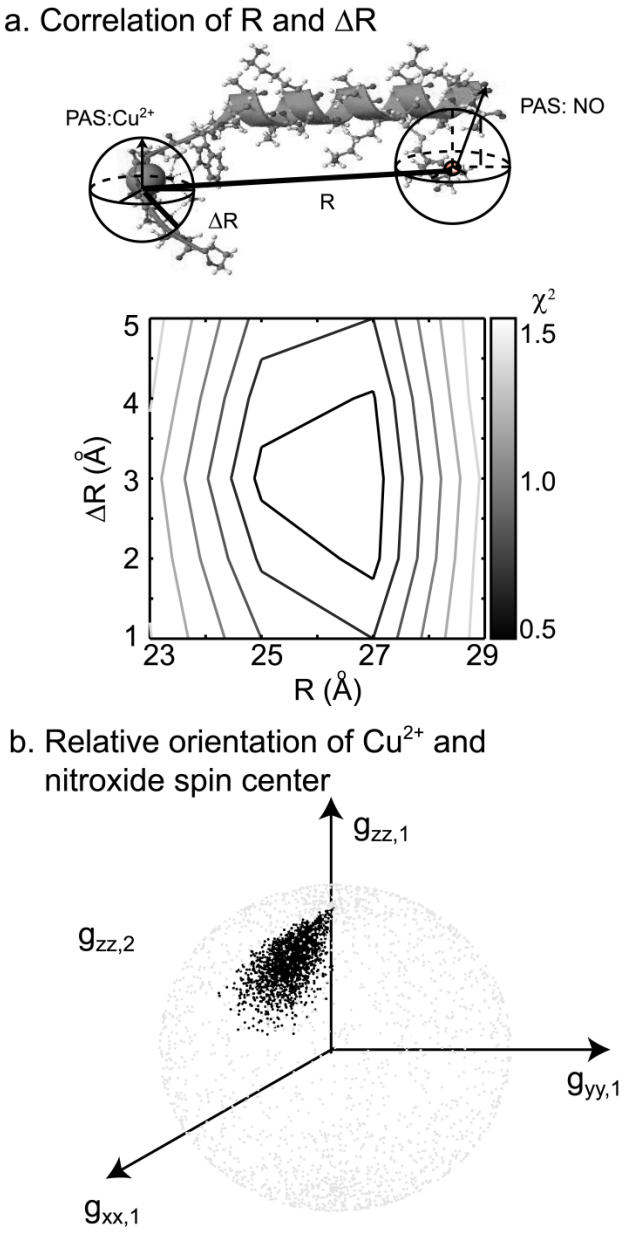

Figure 3-5. (a). Correlation between R and ΔR, using initial inputs of χ=90°, γ=0° and η=60°. The lowest χ^2 value occurs at R=27 Å, ΔR=3 Å, χ=90°, γ=30° and η=30°. (b). Orientations of the nitroxide g_{zz} axis with respect to the Cu^{2+} g-tensor shown by black dots.

The specificity of the optimized Euler angles, χ=90°, γ=30°, η=30°, and σ=9°-12° was further examined by investigating the change of the average χ^2 values upon changing parameters. Representative fittings are shown in Figures 3-6 to 3-8. Our results showed that the χ angle played the most important role. Figure 3-6 shows the fitting of the first 600 ns of the time domain traces for three experimental data sets, by scanning χ values from 0° to 90°, using γ=30° and η=30°. The χ^2 values are listed on each fitting curve. The χ^2 values show that the best χ value occurs at 90°, with corresponding χ^2 values of 0.0802, 0.062, and 0.104 for the three experimental data sets. When the χ value deviated from 90°, the χ^2 value increased more than 3-fold. Similarly, in Figures 3-7 and 3-8, we show the effects of γ and η on the fitting of the experimental data. The changes in χ^2 values by changing the γ and η angles were not as significant as changing the χ values (cf. listed χ^2 values in Figures 3-7 and 3-8). However, different γ and η angles still provided different fits to the experimental data. For instance, as shown in Figure 3-7, γ=0° provides good fits to experimental data at 260 MHz and 364 MHz frequency offsets with the corresponding χ^2 values of 0.0838 and 0.0485, respectively. At 448 MHz resonance offset, however, the χ^2 increased to 0.121. Similarly, as shown in Figure 3-8, using η=0° the fit to the experimental data with 448 MHz resonance offset was actually better than using η=30°, as shown by the χ^2 values. However, the fits to the other two experimental data sets was not acceptable. The optimized σ was also investigated in a similar manner. We observed that σ values below 9° led to a simulated signal with a higher modulation amplitude compared with the experimental data, resulting in a "bad" fit. Conversely, σ values above 12° led to a lower modulation amplitude compared with the experimental data, also resulting in a "bad" fit. The weak orientational selectivity did not change the distance distribution function between spin centers but could be used to isolate the best orientational parameters.

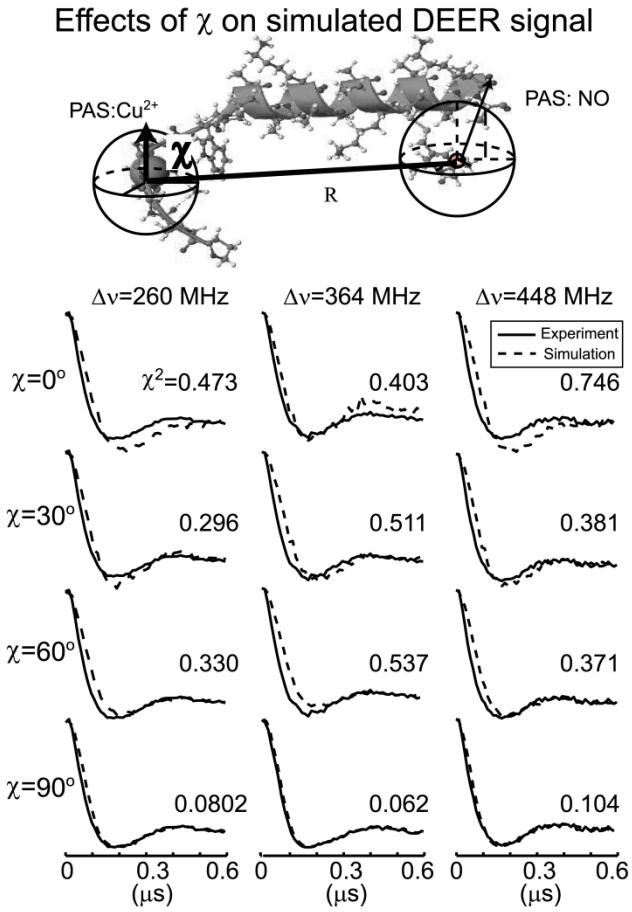

Figure 3-6. Investigation of the effect of the χ angle on the DEER simulation. Representative fitting of three experimental data using χ values varying from 0° to 90° are shown. The χ^2 values for each fitting are also listed. For all experimental data, the best χ value is 90°.

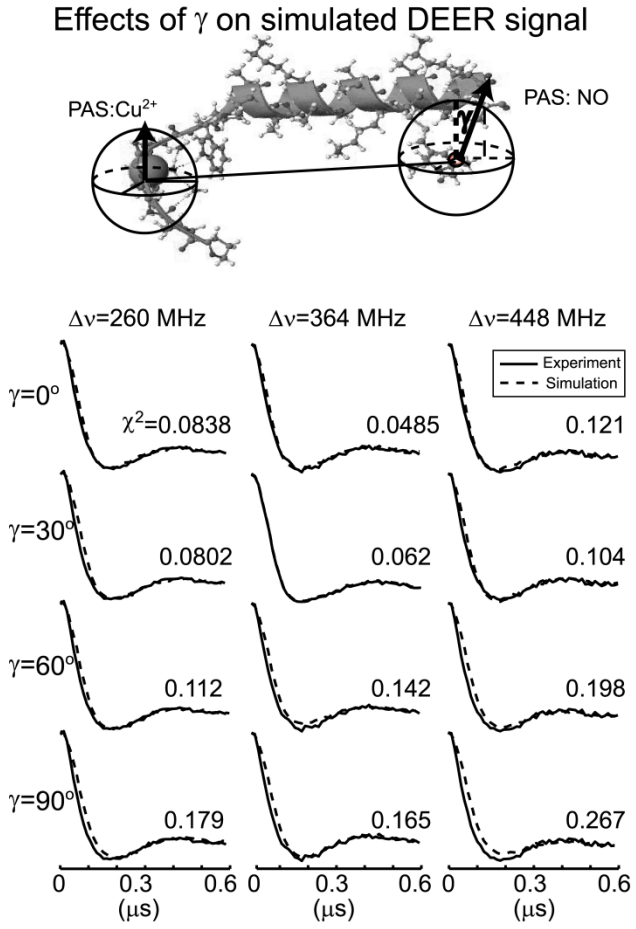

Figure 3-7. Investigation of the effect of the γ angle on the DEER simulation. Representative fitting of three experimental data using γ values varying from 0° to 90° are shown. The χ^2 values for each fitting are also listed. For all experimental data, the best γ value is 30°.

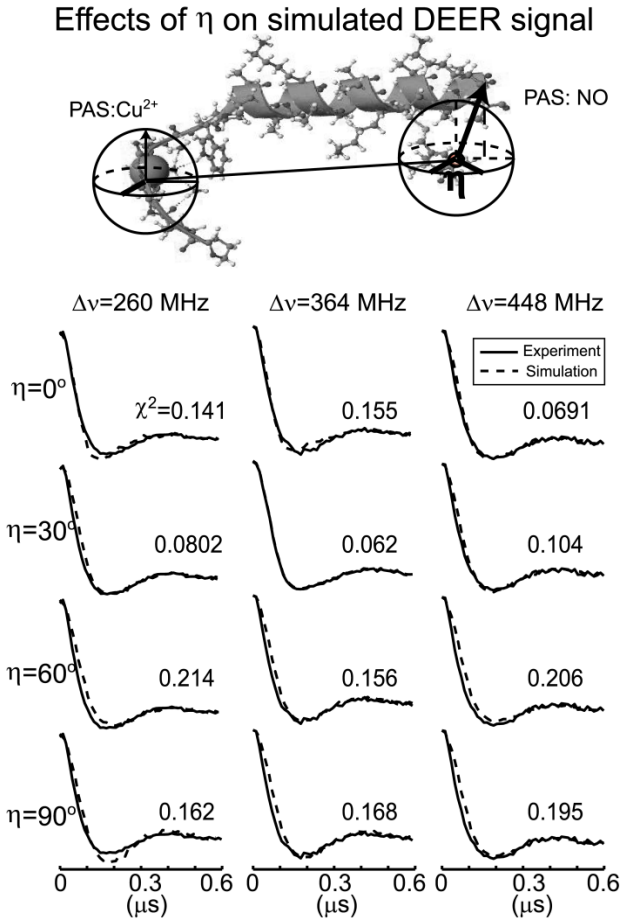

Figure 3-8. Investigation of the effect of the η angle on the DEER simulation. Representative fitting of three experimental data using η values varying from 0° to 90° are shown. The χ^2 values for each fitting are also listed. For all experimental data, the best η value is 30°.

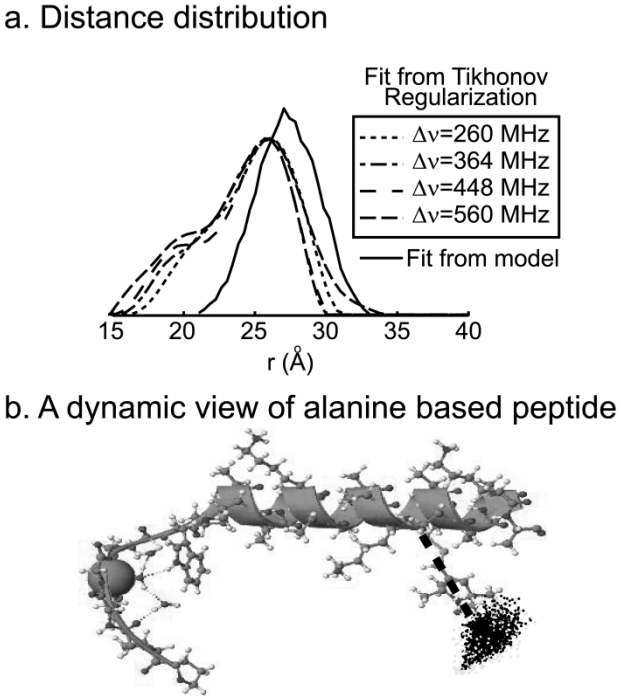

Figure 3-9. (a). Solid line: the determined Cu^{2+}-nitroxide distance distribution function using the molecular model. Dashed lines: the distance distribution functions obtained from different experimental data sets using the Tikhonov regularization method. (b). A "dynamic" view of the alanine-based peptide.

Five different initial inputs were tested in the fitting procedure. In all cases, we obtained the same optimized Euler angles of χ=90°, γ=30°, η=30° and σ of 9° - 12°. The distance distribution function was also unchanged. Spin density delocalization effects were also investigated in the fitting and were found to have no effect on the simulated DEER signal as well as the determined distance distribution function. Using the optimized parameters, the Cu^{2+}-nitroxide distance distribution was calculated by a statistical histogram plot of the spin-spin distances for 2000 conformations and shown by the solid line in Figure 3-9a. The mean distance and the standard deviation were calculated to be 27 Å and 2.4 Å, respectively. The mean distance is consistent with relaxation results (see below) (*132*). The standard deviation is also in agreement with literature estimates of polyalanine peptides (*130*). The large values of σ are reasonable given that a small bending of the polypeptide chain can lead to a large change in the relative orientation. Using the determined Euler angles and standard deviations of Euler angles, the model of the alanine-based peptide was rebuilt. Specifically, the nitroxide spin label was oriented by using the optimized γ and η angles. The flexibility of the spin label was also reflected by using the σ from our model. The resultant, "dynamic" structural model of the alanine-based peptide is shown in Figure 3-9b.

In such a Cu^{2+}-based measurement, the use of the Tikhonov regularization method to extract distance distribution functions is believed to be problematic. To illustrate the necessity of full data analysis for Cu^{2+}-based DEER data, the experimental data were analyzed by using the Tikhonov regularization method after baseline correction. The resultant distance distributions are depicted in Figure 3-9a, using different styles of dashed lines (cf. figure captions). The distance distributions obtained from different resonance offsets are slightly different from each other, showing very weak orientational selectivity. The average distances using Tikhonov

regularization are shorter than that obtained from our molecular model (Figure 3-9a solid line). The distributions of distances are broader than that from our molecular model. This is due to the fact that the Tikhonov regularization method assumes that all of the orientations are excited in the analysis of the DEER signal. However, in the case of Cu^{2+}-based DEER, only partial orientations are excited. To fit the experimental data using the Tikhonov regularization method, broader distance distributions are required to complement the narrower range of excited orientations. Therefore, to obtain precise distance distributions between Cu^{2+} involved spin pairs, full data analysis is required.

The average Cu^{2+}-nitroxide distance in the folded state of the alanine-based peptide has been measured to be 25±0.8 Å at physiological temperatures by using the effects of Cu^{2+} on the T_1 of the nitroxide (*132*). As pointed out by these authors this distance is expected to be shorter than the actual average, since T_1 enhancements depend on r^{-6} rather than r. Indeed, we obtained a mean distance of 27 Å. In comparison, the average distance from the Tikhonov method is smaller than 25 Å. The measurement of the distance distribution allows us to make a closer comparison. The value of r_{ESR}, measured by a relaxation based measurement, as shown by Jun *et. al.* (*132*), is given by

$$r_{ESR} = \kappa^{1/6} \cdot [\left\{\sum_{r_1}^{r_2} P(r)\left(\frac{\kappa}{r^6} + \frac{1}{T_{1s}^0}\right)\right\} - \frac{1}{T_{1s}^0}]^{-1/6} \qquad (17)$$

where κ is a constant as defined previously (*132*), T_{1s}^0 is the longitudinal relaxation time of the "slow" relaxing spin, the nitroxide, in the absence of Cu^{2+}, P(r) is the distance distribution between Cu^{2+} and nitroxide spins, and r is the real Cu^{2+}-nitroxide distance in each conformation of the peptide (*132*). Using the same $T_{1s,0}$ and T_{1s} values as Jun *et. al.* (*132*), we obtained a 25.7 Å "ESR averaged" Cu^{2+}-nitroxide distance using Equation 3-17, consistent with the previous results (*132*). In contrast, using the distance distributions obtained from the Tikhonov

regularization method we obtained "ESR averaged" Cu^{2+}-nitroxide distances of 21 Å to 23 Å, 2 to 3 Å shorter than the previous results (*132*). This further verifies that to obtain precise distance distributions between Cu^{2+} and nitroxide spin centers, full data analysis is required.

DEER on the proline-based peptide. The proline-based peptide contains two copper centers separated by seven prolines. The Cu^{2+} binding environment in the proline-based peptide was also confirmed by using the 3-pulse electron spin echo envelop modulation (ESEEM) spectroscopy (data not shown) (*119*). The experimental DEER traces on the proline-based peptide are shown in Figure 3-10a. The observer pulses were applied at five different magnetic fields scanning from the $g_{\perp}$ region to the $g_{\parallel}$ region, as indicated by the arrows in the inset to Figure 3-10a. The pump pulse was applied at a frequency 92 MHz lower than the observer frequency. The zero time of each data set was precisely determined and illustrated by the dashed line in Figure 3-10a. Depending on the external magnetic field, the modulation depth for each data set is 0.5-2%, consistent with theoretical calculations (*127*). In the raw data, a modulation can be visualized before baseline correction. After baseline correction by using an exponential function, the results are shown in Figure 3-10b. The modulation curve did not change appreciably among the data sets in the $g_{\perp}$ region. The first period of modulation ends at ~600 ns for each data set. At the $g_{\parallel}$ region, the first period of modulation ends at ~540 ns, which differs distinctively from other data sets (cf. the vertical dashed line). The Fourier transformation of the baseline corrected signal also show subtle differences in the dominant frequency peak (cf. Figure 3-11). From the $g_{\perp}$ region to the $g_{\parallel}$ region, the main frequency peak shifts ~ 0.15 MHz. This shift is distinguishable given a resolution of 0.06 MHz in the frequency domain. Such subtle differences can not be directly used to calculate the spin-spin distance between spin centers. Quantitative analysis of the orientational effects is required.

Before fitting the experimental data, a raw structure of the peptide was constructed by using the package of CAChe 6.12 using the following procedures. The seven prolines were built to form a PPII conformation. The structure of the two Cu^{2+}-PHGGGW groups were adapted from the crystal structure obtained by Millhauser and coworkers (*119*). The two Cu^{2+}-PHGGGW groups were connected to both ends of the seven proline segment. The binding angles and dihedral angles between the PHGGGW groups and the seven-proline segment were adapted from Becker *et. al.*, where two Cu^{2+} bound PHGGGW groups were attached to a three-proline segment (*117*). The resultant proline-based peptide is shown in Figure 3-2b. The Euler angles are measured to be χ=60°, γ=30° and η=0° in this model. These Euler angles were used as the initial inputs. The standard deviation was assumed to be the same for all of the three Euler angles, at 20°. The correlation of R and ΔR was calculated and shown in Figure 3-12a. The best fit occurred at R = 30 Å and ΔR= 3 Å. We then fixed R and ΔR at the pre-optimized values and optimized the other parameters. The best fit occurred at (χ, γ, η) = (60°, 60°, 0°) and σ from 9° - 12°. Using these Euler angles and deviations, the R and ΔR correlation was checked again. The best fit still occurred at R = 30 Å and ΔR = 3 Å. Using the optimized parameter set, the relative orientations between Cu^{2+} g-tensors can be illustrated by the black dots shown in Figure 3-12b.

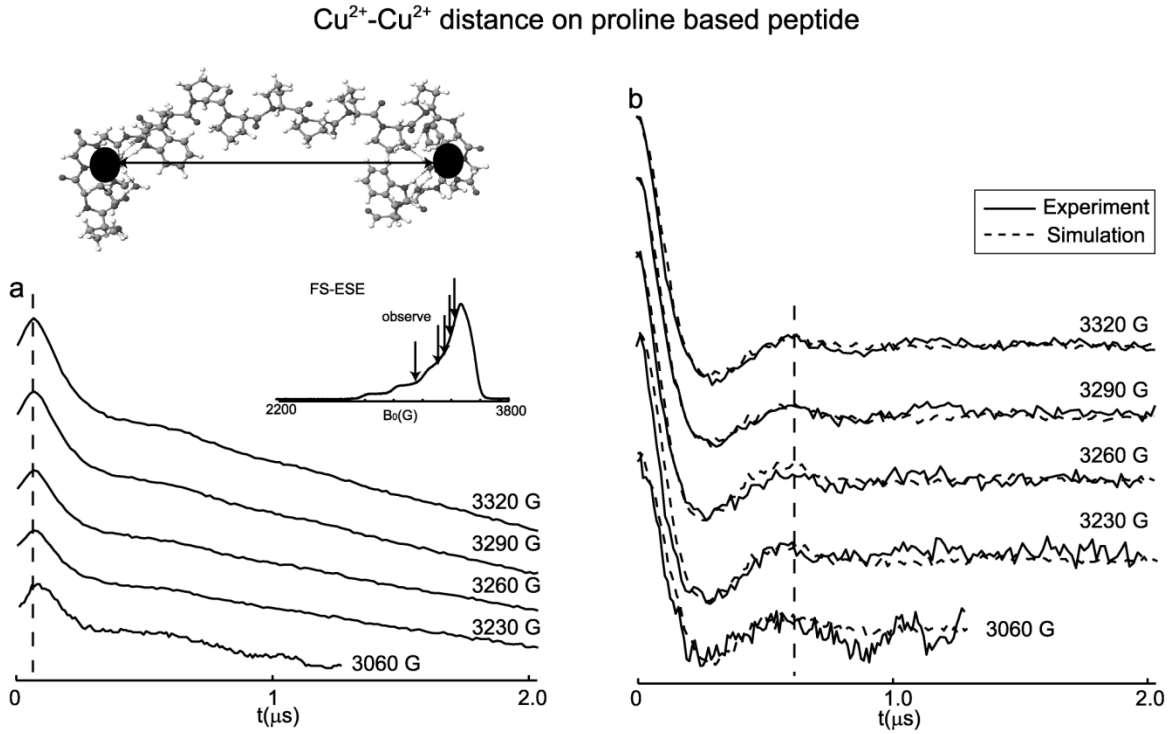

Figure 3-10. (a). Experimental DEER time domain traces for the proline-based peptide at five magnetic fields between 3060 G and 3320 G. The vertical dashed line indicates the zero time of each trace. (Inset) The FS-ESE spectrum of the proline-based peptide with observer frequencies indicated by arrows. The pump pulse was kept 90 MHz lower than the observer frequency in all the data sets. (b). DEER signal after the removal of the intermolecular decay by division of an exponential decay. At the $g_{\perp}$ region, the modulation period is ~ 600 ns. At the $g_{\parallel}$ region, the modulation period shifts to ~ 540 ns. These baseline corrected DEER data were fit by using the theoretical model developed in this work. Simulations are shown by dashed lines.

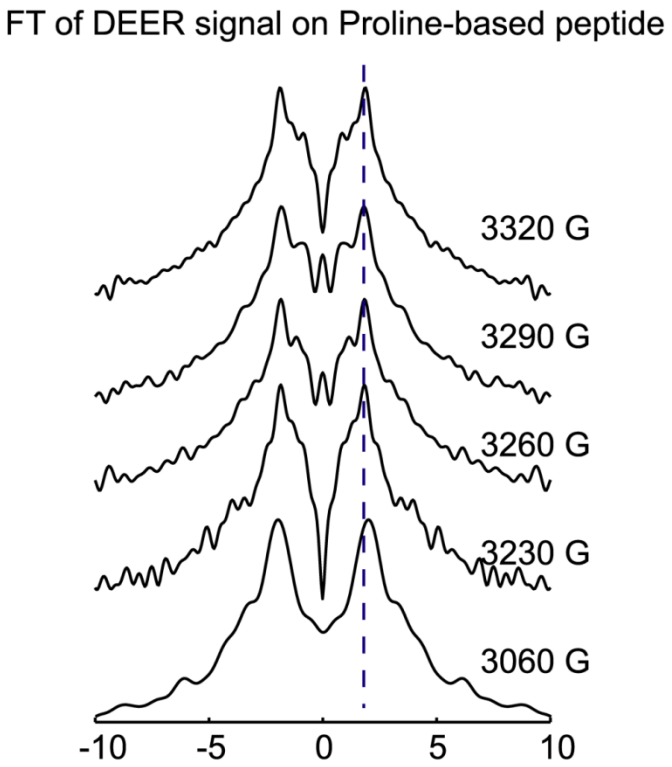

Figure 3-11. Fourier transformation of the experimental signal with corresponding experimental magnetic field listed. The SNR is similar to all these data sets. The “noise” in the first four data sets is due to the sinc effects from zero-filling of the original data, with the purpose of increasing resolution.

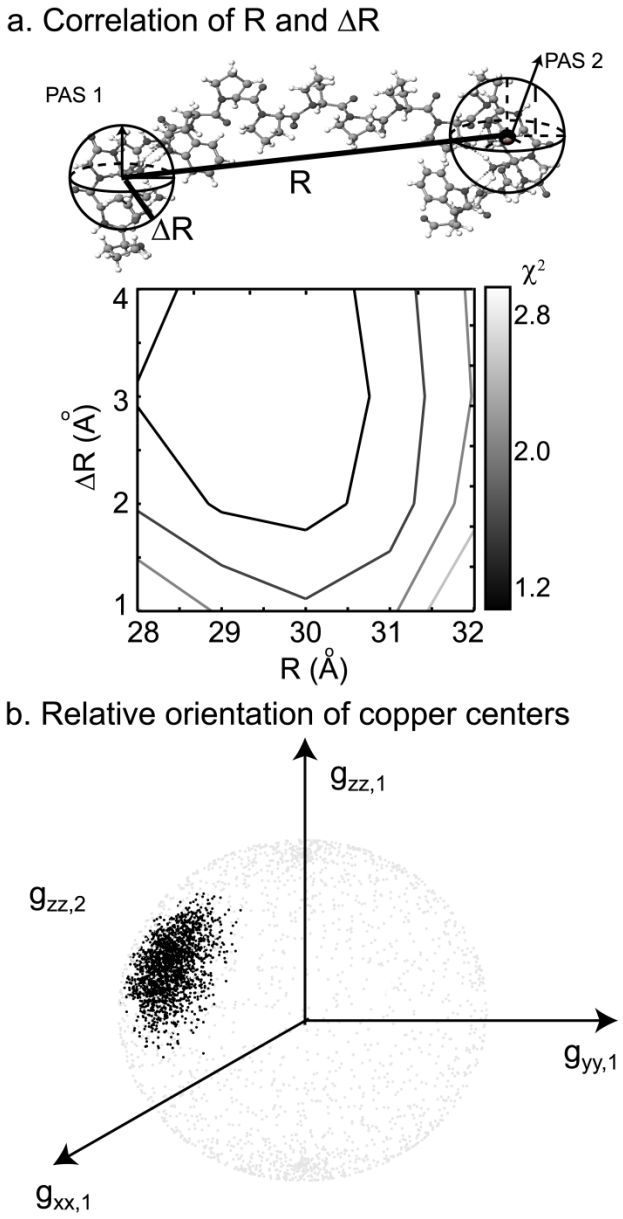

Figure 3-12. (a). Correlation between R and ΔR, using initial inputs of χ=90°, γ=0°, η=60°. The lowest χ^2 value occurs at R= 30 Å, ΔR= 3 Å, χ=60°, γ=60°, and η=0°. (b). Orientations of the second Cu^{2+} g_{zz} axis with respect to the first Cu^{2+} g-tensor shown by black dots.

The specificity of the optimized Euler angles, χ=60°, γ=60° and η=0° was further examined by investigating the change of the average χ^2 values upon changing the Euler angles. Representative fittings are shown in Figures 3-13 to 3-15. Figure 3-13 shows the fitting of the first 1000 ns of time domain traces for three experimental data sets, by scanning χ values from 0° to 90°, using γ=60° and η=0°. The χ^2 values are listed near each fitting curve. Both visual inspection and the χ^2 values show that the best χ value occurred at 60°, which resulted in χ^2 values of 0.11, 0.0745 and 0.0791 for the three experimental data sets. When the χ value deviated from 60°, the χ^2 value increased up to 5-fold. Similarly, in Figures 3-14 and 3-15, we show the effects of γ and η on the fitting of the experimental data. The changes in χ^2 values by changing the γ and η angles were not as significant as changing the χ values (cf. Figures 3-14 and 3-15). For instance, in Figure 3-14, γ=30° provides good fits to experimental data at 3290 G and 3260 G, with the corresponding χ^2 values of 0.0528 and 0.089, respectively. At 3320 G, however, the χ^2 increased to 0.176. The failure of using γ=30° to fit the experimental data with 3320 G ruled out the possibility of γ = 30°. Similarly, as shown in Figure 3-15, using η=30° the fits to the experimental data with 3320 G and 3290 G was slightly better than using η=0°, based on the χ^2 values. However, the fit to the experimental data at 3260 G was not acceptable. Varying σ values resulted in the same scenario as in the case of the alanine-based peptide. The weak orientational selectivity did not change the distance distribution function between spin centers but could be used to isolate the best orientational parameters.

Similar to the fitting procedure for the alanine-based peptide, up to five other initial inputs were tested for the proline-based peptide. Our simulations showed that the optimized parameter set and distance distribution function were unaffected. Spin density delocalization

effects were also investigated and did not affect the simulated DEER signal as well as the determined distance distribution function (*53*).

The Cu^{2+}- Cu^{2+} distance distribution was calculated by a statistical histogram plot of the spin-spin distances for 2000 conformations generated using our model and shown by the solid line in Figure 3-16a. The mean distance and standard deviation was calculated to be 30 Å and 2.4 Å, respectively. The average Cu^{2+}-Cu^{2+} distance is consistent with the structural model shown in Figure 3-2b. The standard deviation is in agreement with literature estimates of polyproline peptides (*131*). Similar to the alanine-based peptide, the large σ values are reasonable given that a small bending of the proline-based peptide can lead to a large change in the relative orientation between Cu^{2+} centers. The distance distribution function obtained from our molecular model was compared with that from the Tikhonov regularization method. As shown in Figure 3-16a, the distance distribution function from the Tikhonov regularization method shows a shorter mean Cu^{2+}-Cu^{2+} distance and a broader distribution of Cu^{2+}-Cu^{2+} distances. The rationalization of these experimental results is similar to that in the case of the alanine-based peptide. This further verifies that to obtain precise Cu^{2+}-Cu^{2+} distances, full data analysis is required. Using the determined Euler angles and standard deviations of these angles, the model of the proline-based peptide was rebuilt. Specifically, the position and the orientation of the second copper center with respect to the first copper center were determined by the optimized variables in the model. The resultant, “dynamic” structural model of the proline-based peptide is shown in Figure 3-16b.

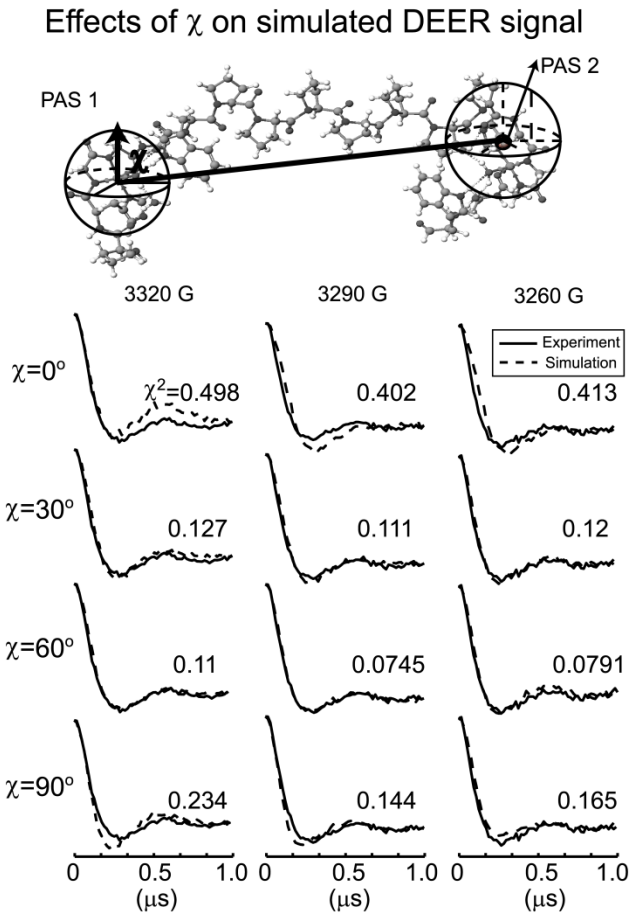

Figure 3-13. Investigation of the effect of the χ angle on the DEER simulation. Representative fitting of three experimental data using χ values varying from 0° to 90° are shown. The χ^2 values for each fitting are also listed. For all experimental data, the best χ value is 60°.

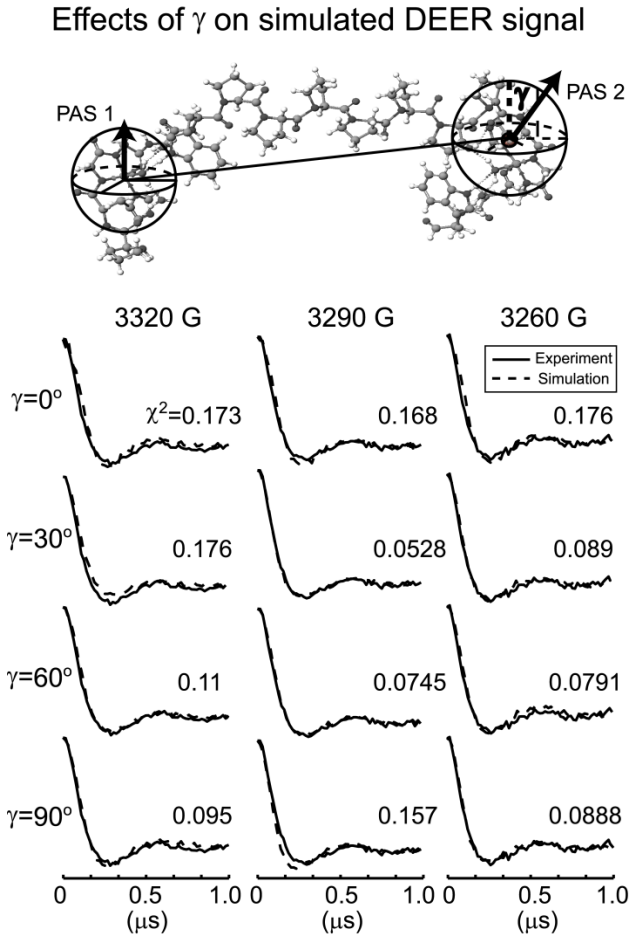

Figure 3-14. Investigation of the effect of the γ angle on the DEER simulation. Representative fitting of three experimental data using γ values varying from 0° to 90° are shown. The χ^2 values for each fitting are also listed. For all experimental data, the best γ value is 60°.

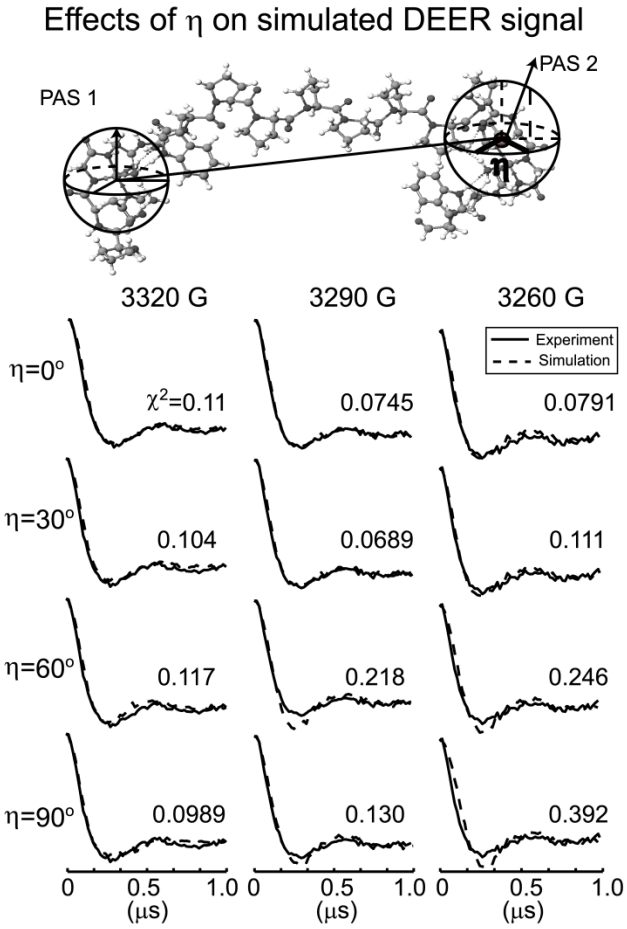

Figure 3-15. Investigation of the effect of the η angle on the DEER simulation. Representative fitting of three experimental data using η values varying from 0° to 90° are shown. The χ^2 values for each fitting are also listed. For all experimental data, the best η value is 0°.

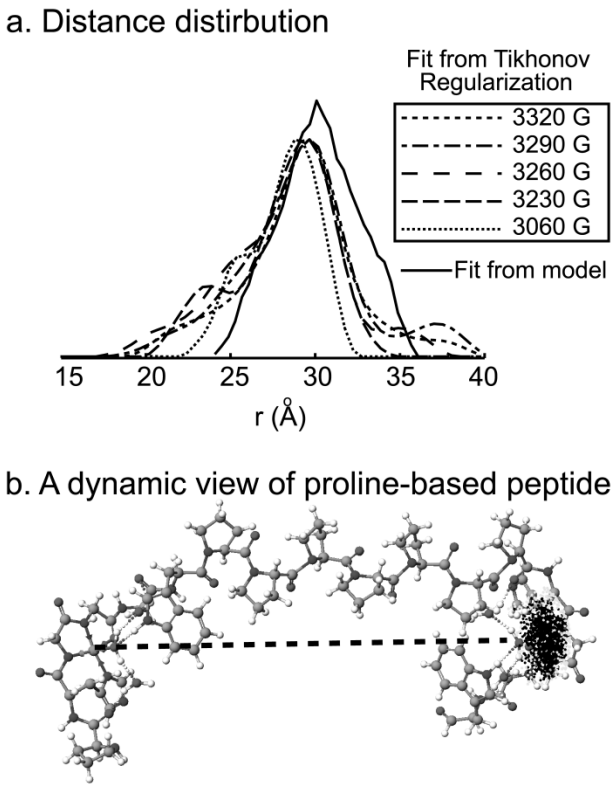

Figure 3-16. (a). Solid line: the determined Cu^{2+}- Cu^{2+} distance distribution function using the molecular model. Dashed lines: the distance distribution functions obtained from different experimental data sets using the Tikhonov regularization method. (b). A "dynamic" view of the proline-based peptide obtained based on the relative orientation and flexibility determined from the analysis of the DEER data on the proline-based peptide.

Role of σ in reducing orientational effects. For both peptides, the flexibilities of the Euler angles reduced the orientational selectivity of the simulated DEER signal. This is reflected by representative calculations of the geometrical factor shown in Figure 3-17 for the proline-based peptide at two magnetic fields. In Figure 3-17, at two different magnetic fields, σ=1° leads to extremely different θ excitation profiles. Strong orientational selectivity of the DEER signal can, therefore, be anticipated in cases of smaller σs (*50*). Our simulations also confirmed this consequence. As σ increases, the θ excitation profiles for both magnetic fields become broader, indicating that more θ angles are excited. However, the excitation probabilities for different θ angles are not uniform. Therefore the case of σ=10° is not sufficient to completely wash out the orientational selectivity, and we still anticipate observing weak orientational effects on the DEER signal, as confirmed by our simulations. As σ increases to higher values, the orientational selectivity further reduces.

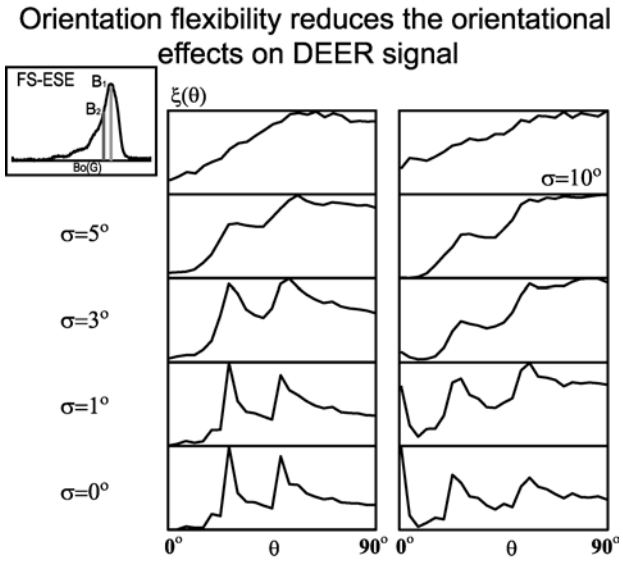

Figure 3-17. Representative calculations of the geometrical factor for the proline-based peptide at two magnetic fields, 3342 G and 3290 G. As σ increases, the θ excitation profiles show that more θ angles are excited, indicating that the orientational selectivity is reduced. (Inset) Field-swept electron spin echo spectrum with the two magnetic fields indicated.

3.5 SUMMARY

We show DEER data on a bis-Cu^{2+}-labeled peptide and a Cu^{2+}-nitroxide labeled peptide. DEER experiments were performed at several external magnetic fields and resonance offsets, to probe the orientational effects on the Cu^{2+}-based DEER signal. Subtle but detectable orientational effects were observed from the DEER spectra of both peptides at X-band. A general theoretical model was developed to analyze the experimental data sets. A 30 Å mean Cu^{2+}-Cu^{2+} distance and a 27 Å mean Cu^{2+}-nitroxide distance were determined. The relative orientation of spin centers was also determined from the molecular model for both peptides. We show that to obtain precise Cu^{2+}-based distance distributions a full data analysis procedure that incorporates orientational effects is required. Our data analysis procedure is applicable to a unknown, larger sample.

3.6 ACKNOWLEDGMENT

This work was supported by NSF (MCB 0842956). We thank Prof. Sarah Larsen and Dr. William Ames for providing the spin density distribution in the Cu^{2+} bound PGHHHW group. We also thank Ming Ji for the spin density distribution calculations using the ORCA package.

4.0 PRACTICAL ASPECTS OF CU ION-BASED DOUBLE ELECTRON ELECTRON RESONANCE DISTANCE MEASUREMENTS

This work, written in collaboration with Ming Ji, and Sunil Saxena, is in preparation for submission to Journal of Magnetic Resonance.

4.1 ABSTRACT

In this chapter, we present the optimal experimental conditions that lead to efficient Cu^{2+}-based DEER data collection. The optimal experimental temperature is ~20 K, and the preferable sample concentration is in the range 0.1 -1.5 mM. By systematically investigating the effects of pulse lengths, we find that the optimal observer π pulse length is 20 to 48 ns and the length of the pump pulse needs to be minimized (16 ns in our case). Simulations show that the use of relatively shorter observer pulses (~20 ns) does not eliminate the orientational selectivity. For a Cu^{2+}-Cu^{2+} DEER measurement, the optimal frequency offset is ~100 MHz. For a Cu^{2+}-nitroxide DEER measurement, the frequency offset is often varied in the range 100 to 500 MHz, to probe the orientational selectivity. For both cases, the frequency of the pump pulse is smaller than the observer pulses in order to obtain a better modulation depth. For the same reason, the pump pulse is typically chosen to be resonant with the central nitroxide peak for Cu^{2+}-nitroxide distances, and resonant at a higher magnetic field for Cu^{2+}-Cu^{2+} distances. In addition, we show the effects

of multiple coupled spins in a Cu^{2+}-based sample on the modulation depth of the DEER signal. The experimental parameters are applicable to general paramagnetic metal ion-based DEER measurements.

4.2 INTRODUCTION

Double electron electron resonance (DEER) (*1, 2, 137*) has become an attractive approach to measure distance distributions between paramagnetic centers. The most commonly employed paramagnetic centers are nitroxide spin labels, which are usually attached to a protein by using site-directed spin labeling (SDSL) (*4, 58-60*). The distance distribution between spin labels can be extracted from the DEER data by utilizing Tikhonov regularization (*5, 6*). Using this approach, information on structures of soluble proteins (*7-20*), DNA and RNA (*21-26*), oligomers (*27-34*) and even more complicated systems such as membrane proteins (*35-47*) and protein-protein/protein-DNA complexes (*12, 48, 49*) has been determined. Recently, paramagnetic metal centers, such as Cu^{2+}, have begun to be employed (*7, 32, 50-53*), with the motivation of measuring Cu^{2+}-Cu^{2+} distances in metalloproteins. In combination with SDSL, Cu^{2+}-nitroxide distance distributions can also be measured (*51*).

Generally the extension of the DEER technique to the case of metal ions is a non-trivial task. For the case of nitroxide-nitroxide distance measurements, the distance distribution is obtained from the experimental signal by solving a Fredholm equation containing a simplified kernel that is readily available from theory. This approach of analysis is not usually applicable to systems containing paramagnetic centers. The use of microwave pulses of durations in the 10's of nanoseconds necessarily leads to the excitation of only select spins in the ensemble, whose

interspin vector is appropriately oriented with respect to the main magnetic field. Consequently, the Cu^{2+}-based DEER signal becomes orientational selective, meaning that the DEER signal depends on the relative orientation of the two Cu^{2+} g-tensors. We and other research groups find that, to obtain precise Cu^{2+}-based distance distributions, it is crucial to account for the orientational effects in the data analysis (*32, 50, 51, 53*).

The established Cu^{2+}-based DEER experimental procedure is to collect DEER signal at several magnetic fields and/or frequency offsets. A proper model is then utilized to analyze the data to provide both the spin-spin distance distribution and the relative orientation of spin centers. The high-field part of the X-band Cu^{2+} spectrum is highly disordered because of the interplay of g and A anisotropies, in combination with $I = 3/2$. The orientational effects on the DEER signal are generally diluted. In combination with a distribution in relative spin center orientation, the differences in time domain signal collected at different magnetic fields and/or frequency offsets are very subtle (*50, 51*). Therefore, to perform orientational selectivity analysis, a high-quality data is required to distinguish the differences between time domain signals. In particular, ESR parameters such as pulse lengths, frequency offsets and external magnetic fields need to be considered prior to a Cu^{2+}-based DEER measurement, in order to optimize the sensitivity of the DEER measurement. Therefore, it is crucial to understand the effects of each parameter on the DEER signal and select optimal parameters for efficient data collection.

We provide a systematic investigation of some key parameters in DEER measurements. We show the effects of these parameters on the DEER signal to provide the optimum values that can lead to efficient Cu^{2+}-based DEER data collection. We also provide a discussion on the

calculation of the DEER signal modulation depth for systems with both Cu^{2+} and nitroxide spin centers.

4.3 MATERIALS AND METHODS

Sample preparation: Two peptide samples were used in this work, an alanine-based peptide and a proline-based peptide. The sequence of the alanine-based peptide is PPHGGGWPAAAA-KAAAAKCAAAAKA (P, proline; H, histidine; G, glycine; W, tryptophan; A, alanine; K, lysine; C, cysteine). The PHGGGW on one end of the peptide serves as a copper binding sequence (*118, 119, 136*). The purpose of the cysteine residue close to the other end of the peptide is to covalently attach the (1-oxy-2,2,5,5-tetramethylpyrroline-3-methyl) methanethiosulfonate (MTSSL) spin label. The spin labeled alanine-based peptide was mixed with 25 mM *N*-ethylmorpholine (NEM) buffer and 25% glycerol and the pH value of the mixture was adjusted to be 7.4-7.6. The concentration of the peptide sample was 1.2 mM. Isotopically enriched $^{63}CuCl_2$ was dissolved in the same buffer as for the peptide solution with the same pH value to make the Cu^{2+} stock solution. Cu^{2+} was then mixed with the peptide solution with a 1:1 Cu^{2+} to peptide ratio. Based on the binding affinity of Cu^{2+} to the PHGGGW segment, more than 99% of the Cu^{2+} was bound to the peptide (*132*). The peptide sequence of the proline-based peptide is PPHGGGWPPPPPPPHGGGW. This peptide was also synthesized at the Molecular Medicine Institute, University of Pittsburgh. The proline-based peptide was mixed with 25 mM *N*-ethylmorpholine (NEM) buffer and 25% glycerol and the pH value of the mixture was adjusted to be 7.4-7.6. The concentration of the peptide sample was 1.6 mM. Isotopically enriched $^{63}CuCl_2$ was dissolved in the same buffer with the same pH value to make the Cu^{2+}

stock solution. Cu^{2+} was then mixed with the peptide solution with a 6:1 Cu^{2+} to peptide ratio to ensure that both PHGGGW sites were occupied by Cu^{2+}.

Pulsed ESR measurements: Pulsed ESR data were collected at X-band frequencies (9.5–9.7 GHz) using a Bruker Elexsys 580 spectrometer equipped with a MD5 resonator. The temperature was controlled by using a continuous flow helium cryostat (CF935, Oxford Instruments) and an Oxford Intelligent temperature controller ITC 503S. For all pulsed ESR measurements, the resonator was over coupled to a Q~200. The field-swept electron spin echo (FS-ESE) experiments for both samples were obtained by using the pulse sequence of $(\pi/2)$-τ-(π)- τ-(echo). The pulse lengths of the $(\pi/2)$ and (π) pulses were adjusted to be 16 ns and 32 ns, respectively. A total of 1024 data points were collected in the magnetic field domain. The pulse sequence and phase cycling for the four-pulse DEER experiments was described previously (*51*). The pulse length, pump frequency and observer frequency were varied during the measurements to investigate the relationship between these parameters and the DEER signal (details described in each experimental data set). Proton ESEEM effects were averaged as described previously (*51*). The acquisition time for each data set varied from 2 to 72 hours, depending on the signal-to-noise ratio.

4.4 RESULTS AND DISCUSSION

The experimental temperature for DEER measurements is ~ 20 K. The T_m values at this temperature for all of our Cu^{2+}-based samples are in the order of 2-3 μs, which are sufficient for measuring distances up to 45 Å, while the shot repetition times (SRT) at this temperature are in the order of 2-3 ms (*51, 54*), leading to a reasonable data acquisition time (from 2 hours to 3

days, depending on sample concentrations, experimental magnetic fields, pulse power, etc). The sample concentration is ~1.2 mM for the alanine-based peptide and ~ 1.6 mM for the proline-based peptide. These concentrations are found to provide decent signal-to-noise ratios (SNRs) for data sets collected with several magnetic fields/frequency offsets, using a relatively short signal averaging time (2 hrs to 12 hrs) (*51*). However, these concentrations are not mandatory. In our recent work, a concentration of ~180 μM is found to be sufficient to perform Cu^{2+}-based DEER measurements with orientational selectivity analysis (*138*), although the data acquisition time are substantially increased (up to 72 hours). We used a MD5 resonator with an effective sample volume of ~ 120 μl for all of our data acquisition. The bandwidth of this resonator was determined by a nutation experiment on the alanine-based peptide. As shown in Figure 4-1, the pulse nutation frequency remains relatively stable from ~9.5 GHz to ~9.8 GHz, indicating a ~ 300 MHz bandwidth. This suggests that, in a DEER measurement, the optimal frequency offset between the pump and the observer frequency is < 300 MHz. However, practically we were able to achieve a frequency offset of ~500 MHz (*51*).

The DEER signal consists an intramolecular dipolar signal that is overlaid on a featureless decay due to the intermolecular interaction (Figure 1-6 in Chapter 1). In order to maximize sensitivity to the intramolecular interaction, the modulation depth should be maximized. The modulation depth of a normalized DEER signal is defined as $(1-V_p)$, where V_p is the intensity of the baseline intermolecular signal at $t_p = 0$ ns. The pulse length, the frequency offset between the pump and observer frequencies as well as the external magnetic field are key parameters determining the modulation depth.

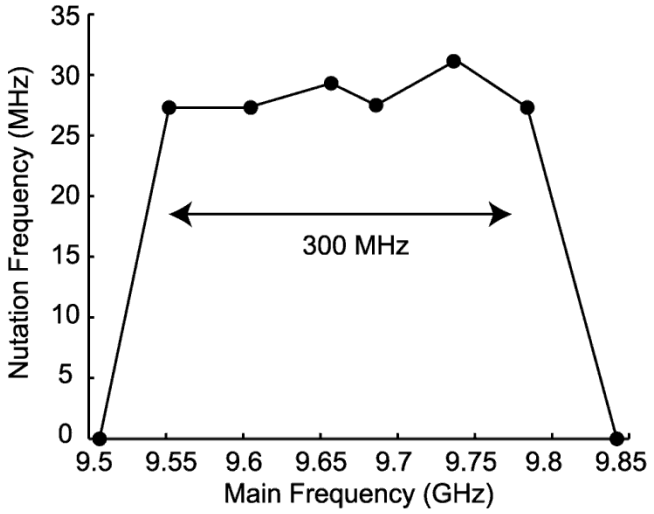

Figure 4-1. The coverage of the MD5 resonator determined by using a standard echo-nutation experiment.

To investigate the effects of pulse length on the Cu^{2+}-based DEER signal, we collected DEER data on the alanine-based peptide with the same frequency offset but different pump and observer pulse lengths. Only the alanine-based peptide was used in this investigation because the modulation depth for this peptide is much higher than the proline-based peptide (up to 20 % comparing with less than 10 % for the proline-based peptide) (*51*). The changes upon application of different pulse lengths are more significant. Initially, the pulse lengths for the pump and observer π pulses were adjusted to be similar to probe the general effects of the pulse length. Figure 4-2 shows the unprocessed DEER data on the alanine-based peptide. The observer pulses are varied from 20 ns to 160 ns, with the corresponding pump pulse scanning from 16 ns to 120 ns, as listed in Figure 4-2. The frequency offset was selected to be 260 MHz, as shown in the inset to Figure 4-2. Both the modulation depth and the slope of each signal change according to different pulse lengths. The baseline of each raw data was corrected using a polynomial function. The baseline corrected signal was then shifted by a value of the corresponding V_p to make each signal start from a value of 1. The resultant signal are shown in Figure 4-3. As the pulse length is increased, the modulation depth of the signal is decreased, from ~19 % to ~1 %. In addition, the signal-to-noise ratio (SNR) is comparable for data sets collected using observer π pulse from 20 ns to 48 ns (cf. Figures 4-3a to d). For observer π pulses that are 60 ns or longer, the SNR is rapidly decreased (cf. Figures 4-3e to h). Therefore, an optimal combination of pulse lengths is an observer π pulse of 20 ns and a pump π pulse of 16 ns, which provides a comparable SNR and the largest modulation depth. The selection of an observer π pulse of 48 ns and a pump π pulse of 36 ns is also found to provide a ~10 % modulation depth with a decent SNR.

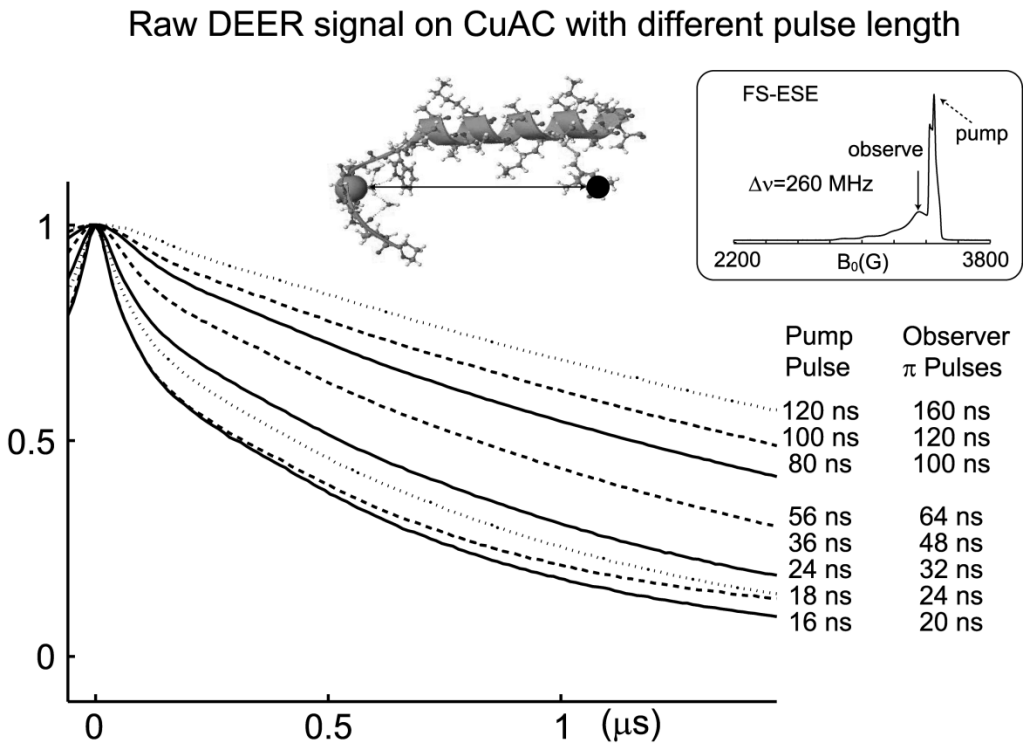

Figure 4-2. Unprocessed DEER data on the alanine-based peptide using different pump and observer pulses. The pulse lengths are listed on each curve. The pump and observer frequencies are selected as indicated in the inset.

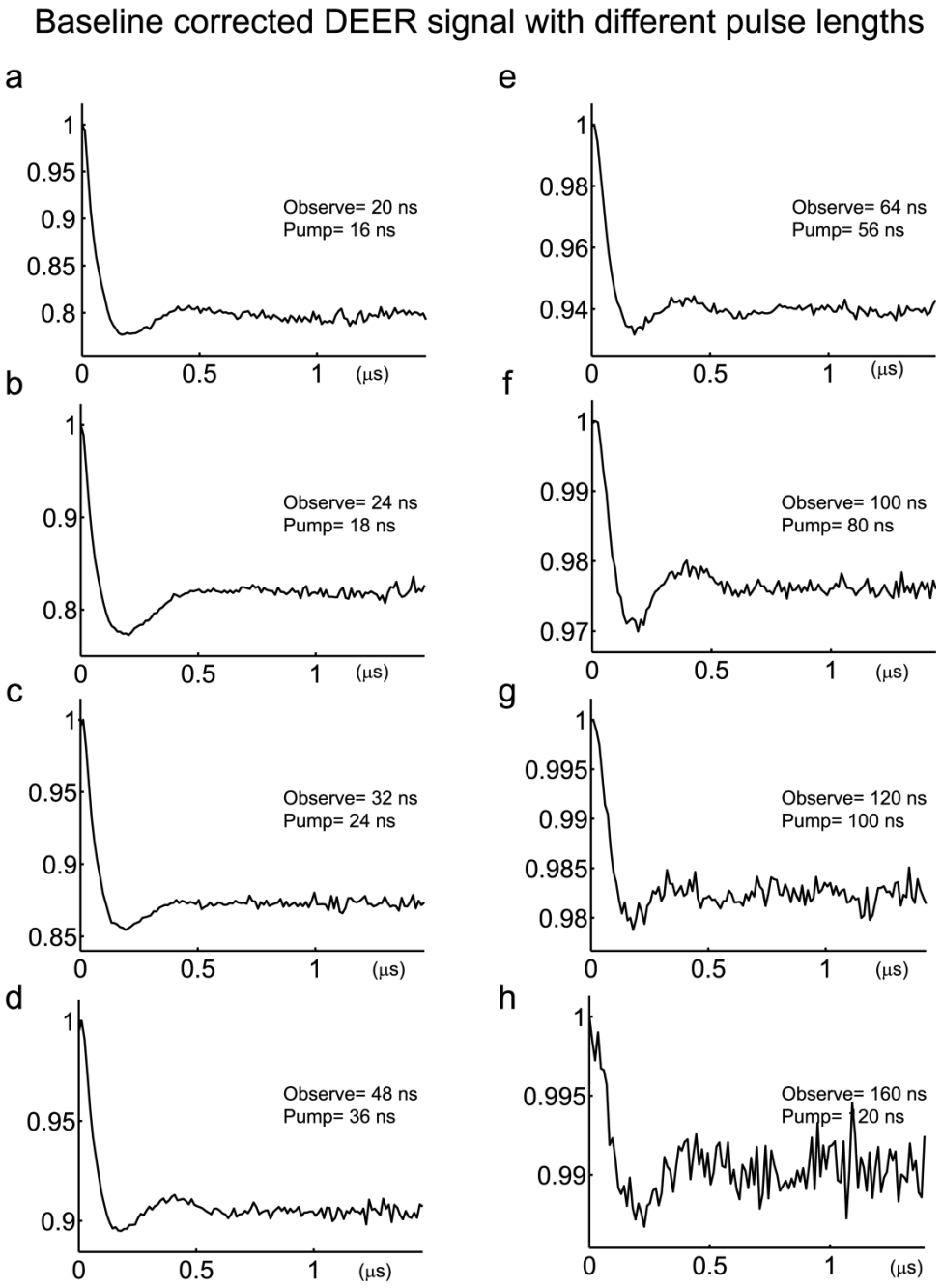

Figure 4-3. Baseline corrected DEER data on the alanine-based peptide using different pump pulses. The pump pulse length for each data set is listed on each curve.

To investigate the effects of pump pulse length on the modulation depth, we show DEER data collected on the alanine-based peptide (the Cu^{2+}-nitroxide labeled peptide) using pump pulse lengths from 16 ns to 80 ns. Since the modulation depth of the signal only depends on the pump pulse length, and a 48 ns observer π pulse provides a comparable SNR as a 20 ns observer pulse does, in these series of experiments, an observer π pulse of 48 ns was used. The general trend of modulation depths and SNR for a 20 ns observer π pulse is identical. The frequency offset in these experiments was set to be 260 MHz (cf. Figure 4-4 inset). The acquisition time for every data was ~ 2 hrs. The unprocessed DEER data with the corresponding pump pulse lengths are shown in Figure 4-4. The modulation depth of each curve is significantly different. This can be better visualized in the baseline corrected data. As shown in Figure 4-5, as the pump pulse is increased from 16 ns to 80 ns, the modulation depth is decreased from 19 % to 4 %. Data shown in Figure 4-5 indicate that, with pump pulse of 16 ns, the modulation depth is the largest, meaning the highest sensitivity. The signal-to-noise ratio for this data set is also substantially higher than other data sets. Under our experimental conditions, clearly the use of a pump pulse length of 16 ns provides the most efficient data collection. A comparison of Figures 4-3a and 4-5a indicates that, for a 16 ns pump pulse, a 20 ns and a 48 ns observer π pulse provide DEER signals with identical SNR and modulation depth. Therefore, the optimal observer π pulse is 20 to 48 ns. The optimal pump pulse is 16 ns.

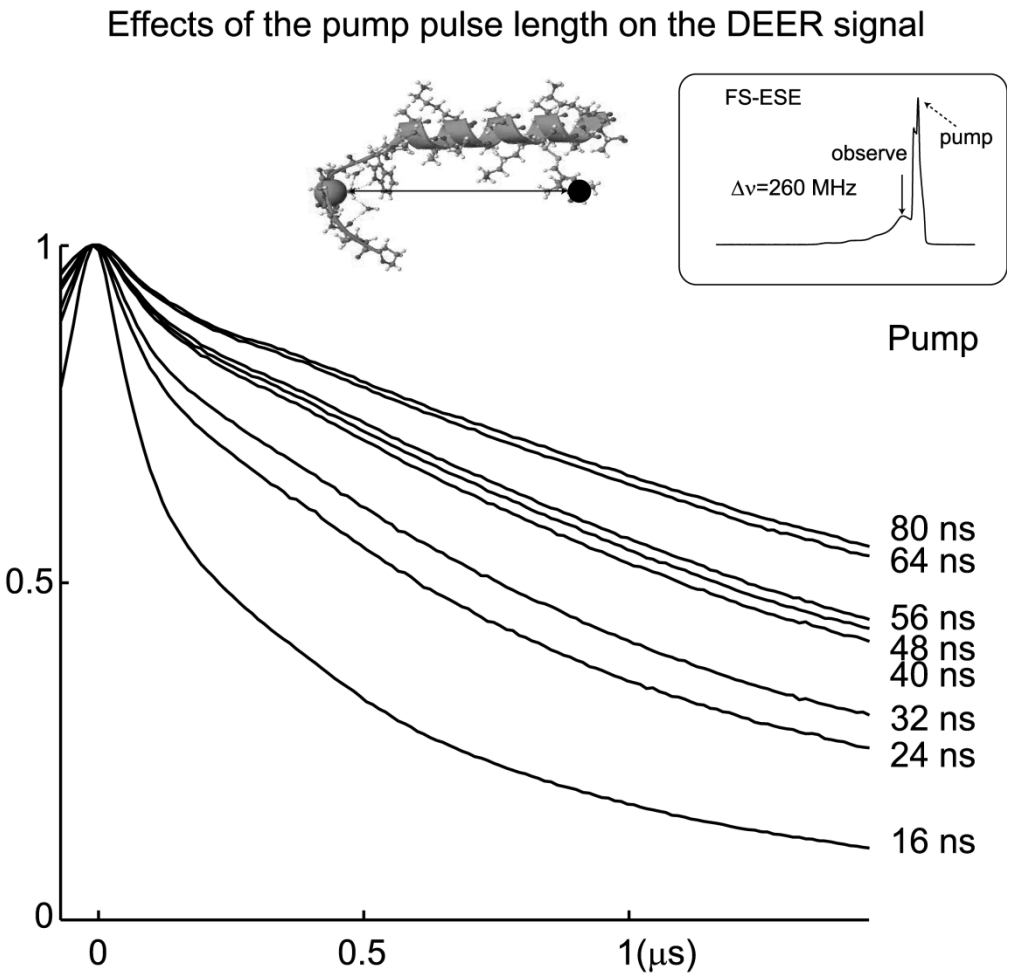

Figure 4-4. Unprocessed DEER data on the alanine-based peptide using different pump and observer pulses. The pulse lengths are listed on each curve. The pump and observer frequencies are selected as indicated in the inset.

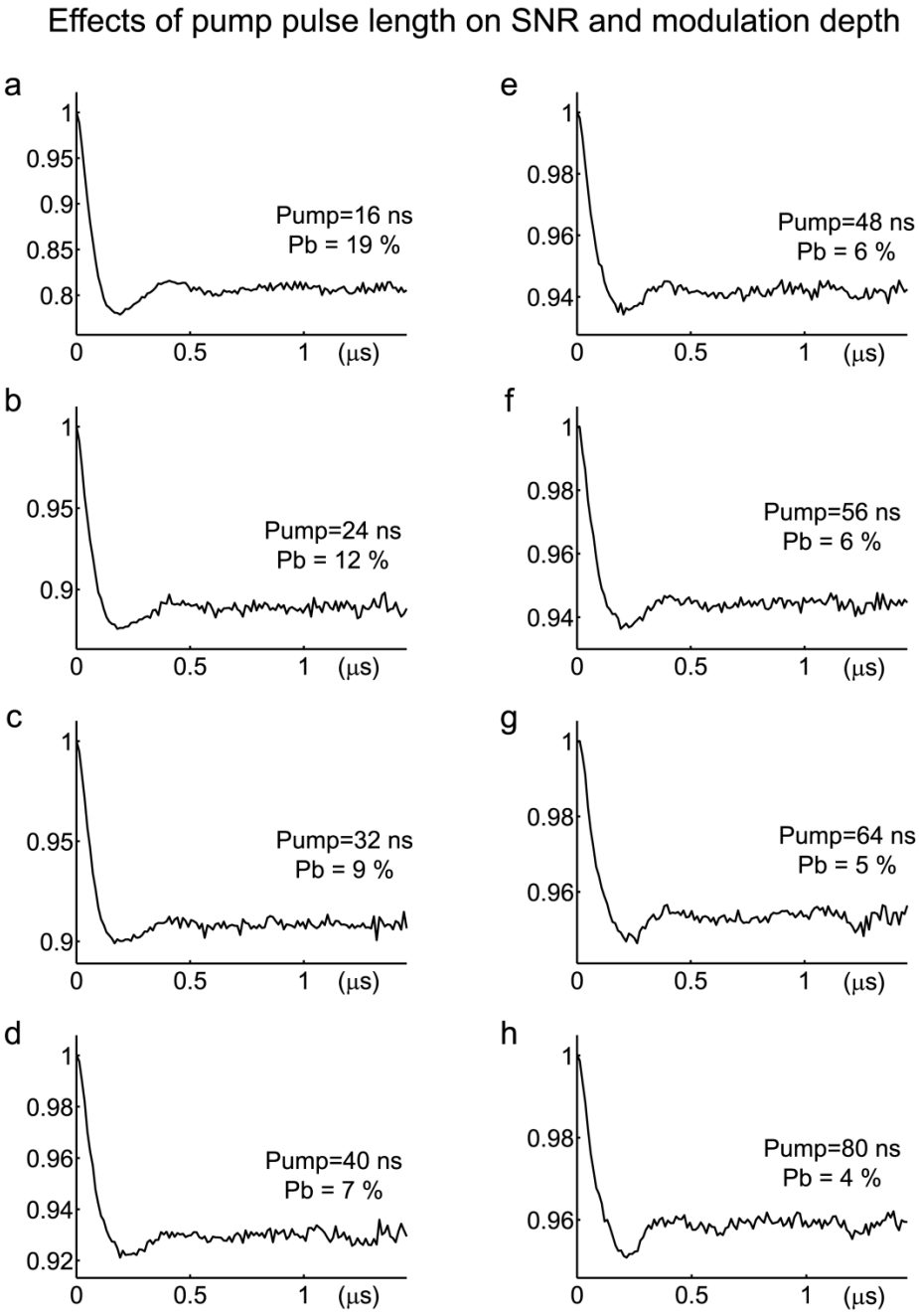

Figure 4-5. Baseline corrected DEER data on the alanine-based peptide using different pump pulses. The pump pulse length for each data set is listed on each curve together with the modulation depth, P_b.

The modulation depth obtained from each data set is recorded and plotted as a function of pump pulse length (cf. Figure 4-6 blue squares). The uncertainty of the modulation depth in each data set is estimated to be ~ ± 1 %. This value is a result of different baseline definitions. Generally these modulation depths are consistent with theoretical expectations. We also calculated the modulation depths for each pump pulse length using a theory demonstrated by Tsvetkov and coworkers (*1*). Theoretically, the modulation depth depends on the ESR line shape, the DEER experimental magnetic field and the number of coupled spins. In our measurements, the number of coupled spins in the alanine-based peptides is found to be close to two (*132*). Using these parameters, we calculated the theoretical values for the modulation depth and plotted it as a function of pump pulse length, as shown in Figure 4-6 (the curve). Similar to the trend for the experimental data (the squares), the modulation depth is decreased as the pump pulse length is increased. The experimental values are slightly smaller than theoretical values. This may be caused by the inhomogeneous excitation of the mw B_1-field (*31*). This may also indicate that in the alanine-based peptide sample, not all of the peptides are occupied with two spins (one nitroxide and one Cu^{2+}).

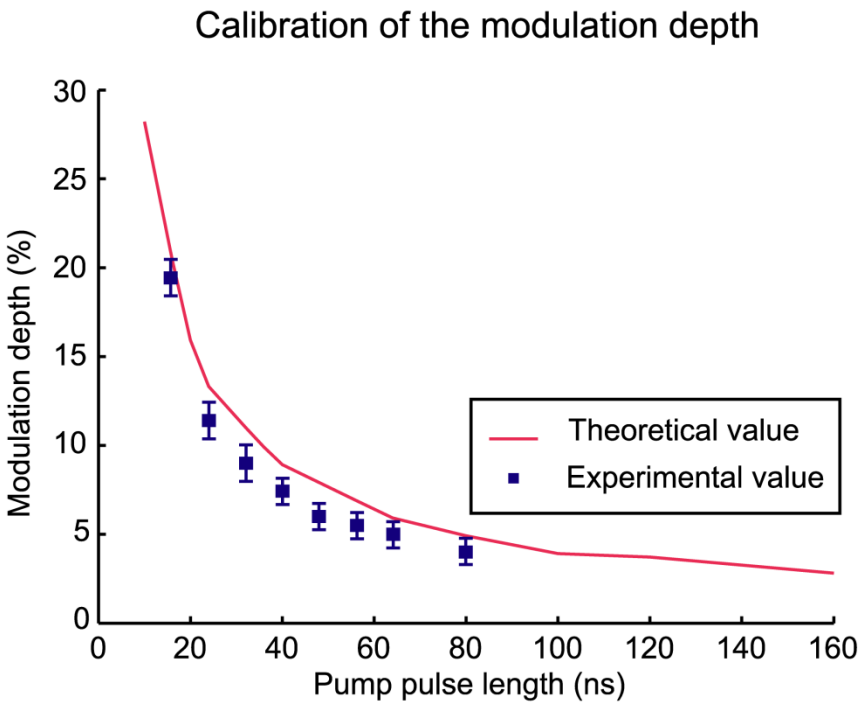

Figure 4-6. Effects of the pump pulse on the modulation depth of the DEER signal on the alanine-based peptide. For pump pulse length from 8 ns to 160 ns, the modulation depths were calculated. The experimental modulation depths for data sets collected using pump pulse lengths from 16 to 80 ns are overlaid on theoretical values and indicated by squares. The error bars are caused by the different definition of baseline.

Similar effects of pulse lengths were also found for the proline-based peptide sample (where two Cu^{2+} ions were attached to both ends of the peptide). Using a shorter observer π pulse (a 24 ns pulse in this case) and a shorter pump π pulse (a 16 ns pulse), we obtained relatively deeper modulation depth (~9 %), as shown in Figures 4-7c and d. The DEER data collected in our previous work using an observer π pulse of 48 ns and a pump π pulse of 36 ns is reprinted in Figures 4-7a and b for the purpose of comparison. Clearly a better choice is to use a shorter pump pulse (16 ns). The frequency offset of 200 MHz in this measurement (Figures 4-7c and d) is selected to reduce the ESEEM effects (*2*). Interestingly, the use of the harder observer and pump pulses still provides an opportunity to probe the orientational selectivity of the Cu^{2+}-based DEER signal. Using the same Cu^{2+}-Cu^{2+} distance distribution and relative orientation of the two Cu^{2+} centers (χ=60º, γ=60º, η=0º) obtained from this peptide (*51*), we simulated DEER signal for five different magnetic fields. As shown in Figure 4-8, a ~60 ns deviation between the time domain signal collected at 3060 G and at the $g_{\perp}$ region indicates that the use of relatively shorter pulses still probes the orientational selectivity.

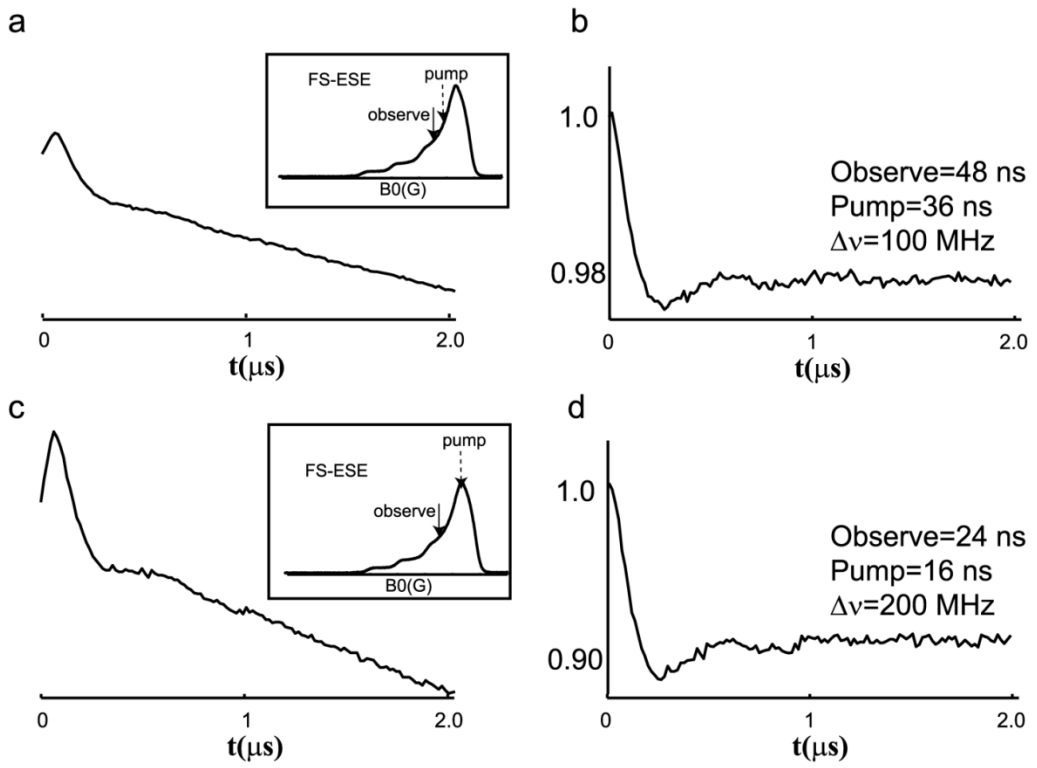

Figure 4-7. (a) Unprocessed DEER signal on the proline-based peptide using 48 ns observer π pulse and 36 ns pump π pulse, with a frequency offset of 100 MHz (data reprinted from Chapter 3 for the purpose of comparison). (b) Baseline corrected signal for data (a). (c) Unprocessed DEER signal on the proline-based peptide using 24 ns observer π pulse and 16 ns pump π pulse, with a frequency offset of 200 MHz. (d) Baseline corrected signal for data (c).

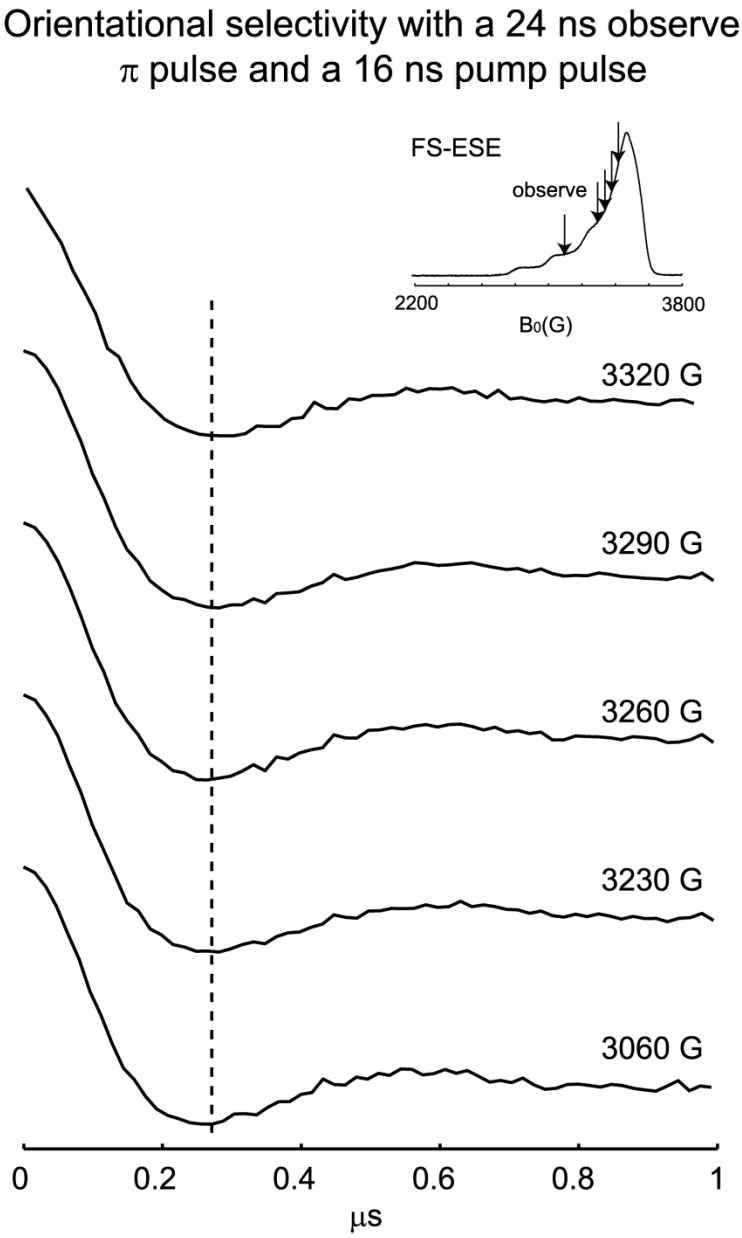

Figure 4-8. DEER simulations show orientational selectivity even under a 24 ns observer π pulse for the proline-based peptide. Using the obtained relative Cu^{2+} g tensor orientation (χ=60º, γ=60º, η=0º), DEER signal were simulated for five different magnetic fields.

Frequency offset and magnetic field: The frequency offset and the main magnetic field are considered together to obtain the best modulation depth. For a sample with only Cu^{2+} probes, the frequency of the pump pulse is often adjusted to be in resonant with a magnetic field that has a higher intensity than the observer pulses, to obtain a better modulation depth (cf. Figures 4-7 and 4-9). The frequency offset is often selected to be relatively narrow (~100 MHz). The reason is that, using the same pump frequency, a smaller frequency offset means that the observer frequency is adjusted to be in resonant with a higher magnetic field compared to a larger frequency offset (ca. 200 MHz). This selection of frequency offset leads to a better SNR.

For a sample with both Cu^{2+} and nitroxide spin labels attached, the pump pulse is often applied at the maximum of the nitroxide ESR spectrum to main the best modulation depth. Example data sets on the Cu^{2+} bound S180C-EcoRI-DNA specific complex (cf. Chapter 5) are shown in Figure 4-9. Using the same frequency offset, the modulation depth of signal collected in the case of pumping nitroxide is larger than in the case of pumping Cu^{2+}. The frequency offset for a sample with both Cu^{2+} and nitroxide spin labels attached is required to be varied in order to probe the orientational selectivity. There is not a strict definition of an "optimal" frequency offset in this case. Usually we use the frequency offset range of 100 MHz to 500 MHz.

Taken together, to perform efficient Cu^{2+}-based DEER data collection, the optimal observer pulse length is ~ 20 to 48 ns (π pulse), and the optimal pump pulse length is the minimum pulse length one can achieve from the instrument. For a Cu^{2+}-nitroxide DEER measurement, the frequency offset is often varied in the range 100 to 500 MHz, to probe the orientational selectivity. The pump pulse is often applied at a magnetic field with a higher intensity than the observer pulses to maintain the maximum modulation depth.

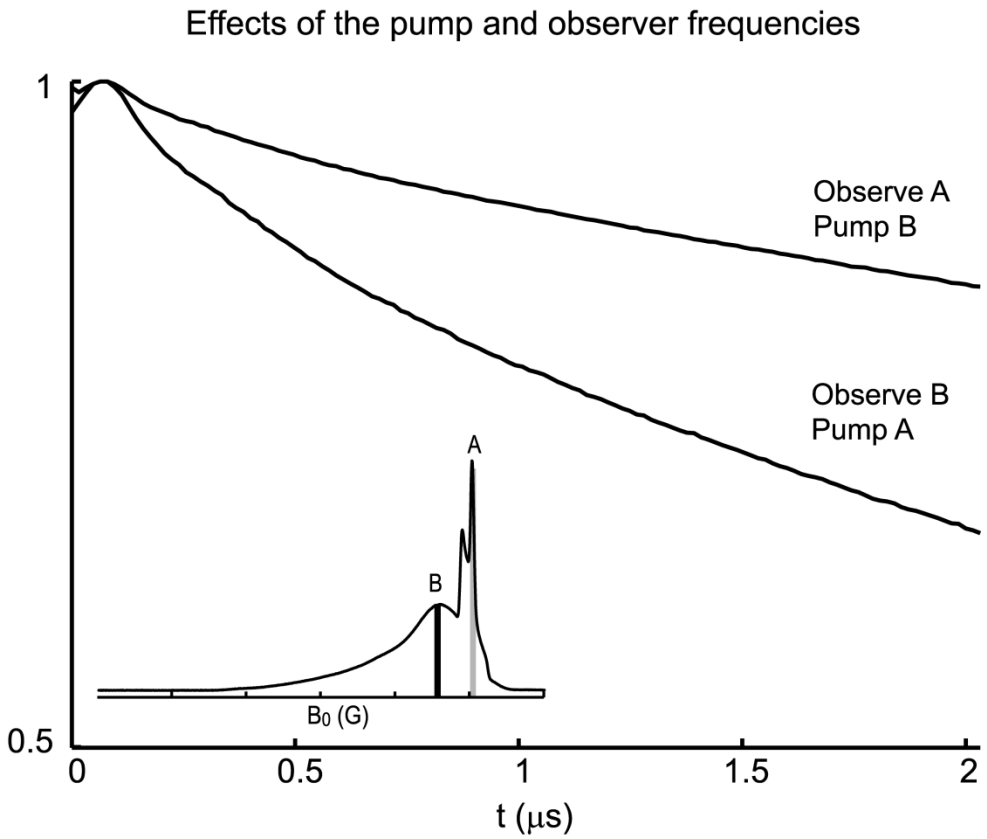

Figure 4-9. Effects of the pump and observer frequencies on the modulation depth of a DEER signal. The data was collected on the Cu^{2+} bound S180C-EcoRI specific complex (cf. Chapter 5).

Number of coupled spins: Besides the distance distribution and relative orientation of spin centers, DEER signal also reflects the number of coupled spins. For a system containing N different spins, the intramolecular interaction V_{intra} is given by the form of (*139*)

$$V(t_p)_{intra} = \frac{1}{N}\sum_{j=1}^{N}\left\{\prod_{\substack{k=1\\k\neq j}}^{N}\left(1-p_b\left(1-\langle\cos\left(D_{jk}\,t_p\right)\rangle\right)\right)\right\} \qquad (4\text{-}1)$$

where j and k are the index of different spins, and D_{jk} is the dipolar interaction between spins j and k. The term, p_b, represents the excitation probability of the spins due to the application of the pump pulse. Orientational effects of the Cu^{2+}-based DEER signal are ignored in Equation 4-1. At t_p of ∞, the $\langle\cos\left(D_{jk}\,t_p\right)\rangle$ is close to zero (*139*).

For a molecule with three nitroxide spins, namely spin A, B and C, Equation 4-1 can be expanded as

$$V(t_p)_{intra} = \frac{1}{3}\left\{\left(1-p_{b,NO}\right)\left(1-p_{b,NO}\right)+\left(1-p_{b,NO}\right)\left(1-p_{b,NO}\right)+\left(1-p_{b,NO}\right)\left(1-p_{b,NO}\right)\right\} \qquad (4\text{-}2)$$

where the term, $p_{b,NO}$, represents the excitation probability of the nitroxide spins due to the application of the pump pulse. For the case where the pump pulse excites spin A and the observer pulses excite spin B and spin C, using Equation 4-1 one obtains the first term in Equation 4-2. Similarly the second term in Equation 4-2 reflects the case where the pump pulse excites spin B and the observer pulses excite spin A and spin C. The third term can be understood analogously. Further simplification of Equation 4-2 gives

$$V(t_p)_{intra} = \left(1-p_{b,NO}\right)^{N-1} \qquad (4\text{-}3)$$

where N=3. This is the well-known equation for calculation of number of coupled spins.

For a spin system containing different spin species, c.a. Cu^{2+} and nitroxide spins, the calculation of the modulation depth requires extra care. As shown in Figure 4-10a, Equation 4-1 becomes

$$V(t_p)_{intra} = \frac{1}{2}\{(1 - p_{b,NO}) + (1 - p_{b,Cu})\} \qquad (4\text{-}4)$$

where the term, $p_{b,Cu}$, represents the excitation probability of the Cu^{2+} spins due to the application of the pump pulse.The first term in Equation 4-4 accounts for the DEER signal contributed by the case where the pump pulse excites the nitroxide spins and the observer pulses excite the Cu^{2+} spins. On the other hand, the second term in Equation 4-4 reflects the case where the pump pulse excites the Cu^{2+} spins and the observer pulses excite the nitroxide spins. Since no Cu^{2+} spins can be excited by applying the pump pulse as indicated in Figure 4-10a, the p_b term in

$$1 - p_b\left(1 - \langle\cos\left(D_{jk}\, t_p\right)\rangle\right) \qquad (4\text{-}5)$$

becomes 0. Equation 4-4 becomes

$$V(t_p)_{intra} = \frac{1}{2}\{(1 - p_{b,NO}) + 1\} \qquad (4\text{-}6)$$

The $p_{b,NO}$ in Equation 4-6 can be calculated for a sample containing only nitroxide spin labels (*1*). Using a 36 ns pump pulse, the $p_{b,NO}$ value is ~10 %. For a sample containing both Cu^{2+} and nitroxide, a $p_{b,NO}$ value of 10 % leads to a theoretical V_P value of ~0.95 according to Equation 4-6. Experimentally we obtained a V_p value of ~0.94. Therefore in our alanine-based peptide, the number of coupled spins is close to 2.

Reversing of the frequencies of the pump and observer pulses generates different V_p values. As shown in Figure 4-10b, the expression of Equation 4-4 is unchanged. Since almost no nitroxide spins are excited by the pump pulse in this case, the p_b value in Equation 4-5 becomes zero, giving the first term of Equation 4-4 a value of 1. Equation 4-4 can be rewritten as

$$V(t_p)_{intra} = \frac{1}{2}\{1 + (1 - p_{b,Cu})\} \qquad (4\text{-}7)$$

The $p_{b,Cu}$ in Equation 4-7 can be calculated for a sample containing only Cu^{2+} spin probes (*1*). Using a 36 ns pump pulse, the $p_{b,Cu}$ value is ~2 %. For a sample containing both Cu^{2+} and nitroxide, a $p_{b,Cu}$ value of 2 % leads to a theoretical V_P value of ~0.99 according to Equation 4-7, consistent with our experimental findings.

For a system with two Cu^{2+} and two nitroxide labels (*138*), the expected V_p value can be obtained in a similar approach. As shown in Figure 4-10c, when the pump pulse is applied to the maximum of the nitroxide ESR spectrum and observer pulses are applied to the maximum of the Cu^{2+} ESR spectrum, the V_P value is equal to 0.895. Switching the pump and observer frequencies, as indicated schematically by Figure 4-10d, generates different modulation depth. Using the same p_b values for Cu^{2+} and nitroxide spins, the V_P value is equal to 0.97.

For a general sample with different spin species, our approach to calculate the V_p is applicable. However, if the sample molecules are not fully labeled, there is no straight forward way to calculate the spin labeling efficiency.

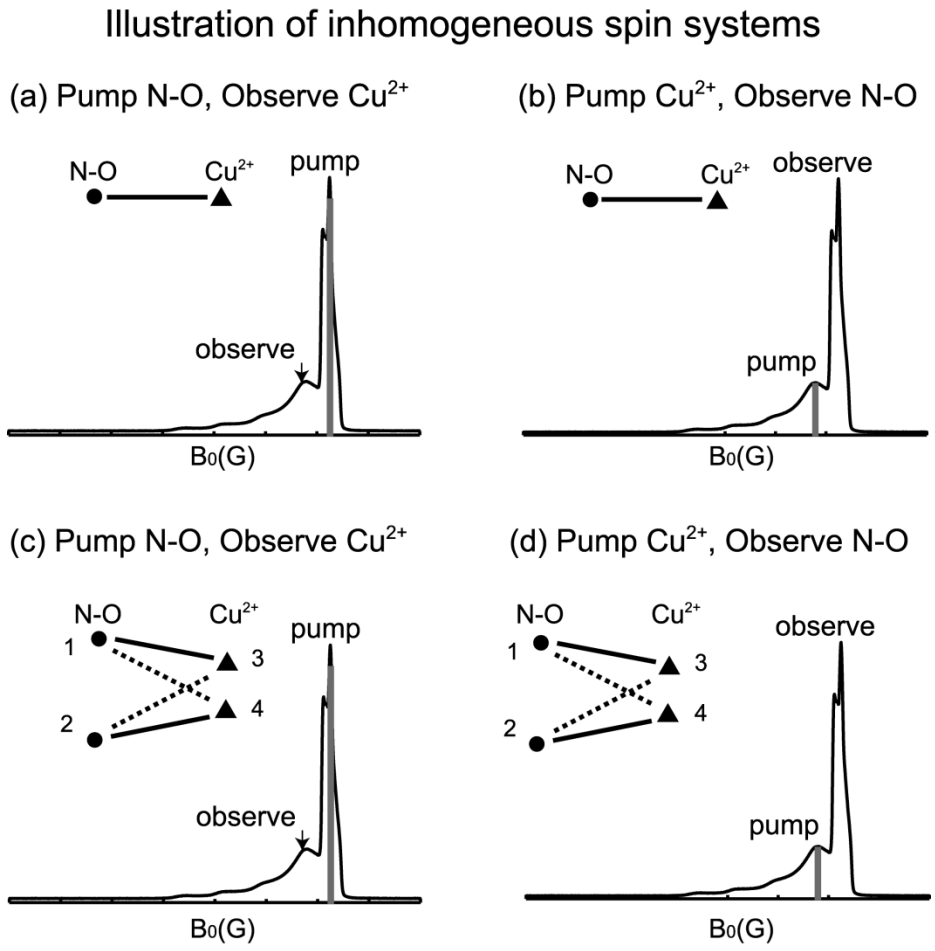

Figure 4-10. Illustration of spin systems and the frequencies applied in a DEER measurement. (a) Illustration of a sample labeled with one Cu^{2+} ion and one nitroxide spin label, with the pump pulse exciting the nitroxide spins and the observer pulses exciting the Cu^{2+} spins. (b) Illustration of the same sample as in (a) but with the pump pulse exciting the Cu^{2+} spins and the observer pulses exciting the nitroxide spins. (c) Illustration of a sample labeled with two Cu^{2+} ions and two nitroxide spin labels, with the pump pulse exciting the nitroxide spins and the observer pulses exciting the Cu^{2+} spins. (d) Illustration of the same sample as in (c) but with the pump pulse exciting the Cu^{2+} spins and the observer pulses exciting the nitroxide spins.

4.5 SUMMARY

We present the optimal experimental conditions and ESR parameters that lead to efficient Cu^{2+}-based DEER data collection. The optimal experimental temperature is ~20 K, and the preferable sample concentration is in the range 0.1 -1.5 mM. By systematically investigating the effects of pulse lengths on the data acquisition, we find that the optimal observer π pulse length is 20 to 48 ns and the power of the pump pulse needs to be maximized (16 ns in our case). Simulations show that the use of relatively shorter observer pulses (~20 ns) does not eliminate the orientational selectivity. For a Cu^{2+}-Cu^{2+} DEER measurement, the frequency offset is ~100 MHz. For a Cu^{2+}-nitroxide DEER measurement, the frequency offset is often varied in the range 100 to 500 MHz, to probe the orientational selectivity. For both cases, the frequency of the pump pulse is smaller than the observer pulses in order to obtain a better modulation depth. For the same reason, the pump pulse is typically chosen to be resonant with the central nitroxide peak for Cu^{2+}-nitroxide distances, and resonant at a higher magnetic field for Cu^{2+}-Cu^{2+} distances. In addition, we show the effects of multiple coupled spins in a Cu^{2+}-based sample on the V_p value of the DEER signal.

4.6 ACKNOWLEDGMENT

The research was supported by an NSF grant (MCB 0842956).

5.0 ESR DISTANCE MEASUREMENTS IN ECORI REVEAL A SECOND METAL ION BINDING SITE

This work, written in collaboration with Ming Ji, Preeti Mehta, Linda Jen-Jacobson, and Sunil Saxena, is in preparation for submission to Proc. Natl. Acad. Sci. U.S.A.

5.1 ABSTRACT

The EcoRI restriction endonuclease cleaves a specific sequence of viral DNA in the presence of some divalent ions such as magnesium. Copper, on the other hand, does not support the catalysis by itself. In order to gain insight into this process, pulsed ESR spectroscopy were applied to the EcoRI-DNA complex. The Electron Spin Echo Envelope Modulation (ESEEM) experiment established that copper is coordinated to one of the five histidine residues in EcoRI. Cu^{2+}-based Double Electron Electron Resonance (DEER) experiments were performed in order to reveal this histidine. Using the Cu^{2+}-based DEER data analysis procedure developed in Chapter 3, copper-copper and copper-nitroxide distances were extracted. A triangulation procedure based on the copper-copper and copper-nitroxide distances demonstrated that Cu^{2+} binds to histidine 114 in EcoRI. Biochemical results show that Cu^{2+} stimulates the Mg^{2+}-catalyzed DNA cleavage. These results raise the question of whether EcoRI can also bind two Mg^{2+} ions during its normal cleavage reaction and, if so, whether the second Mg^{2+} is necessary.

5.2 INTRODUCTION

The EcoRI restriction endonuclease recognizes and binds to the specific recognition site, 5'-GAATTC-3' of DNA. The association constant of EcoRI with the specific site is as much as 90,000 fold higher than with sites (*140, 141*) that differ by one base pair from the specific site. In the presence of Mg^{2+}, the specificity is found to be even higher (*140, 142, 143*), and DNA is cleaved at the specific site. This cleavage activity and selectivity is essential for EcoRI natural function of protecting bacterial cells against viral infection. The DNA cleavage activity is completely dependent on a divalent metal cofactor. Replacement of the natural cofactor Mg^{2+} by other divalent metals decreases the cleavage rates according to the series $Mg^{2+} \approx Mn^{2+} > Co^{2+} >> Zn^{2+} >> Cd^{2+} > Ni^{2+}$ (*144*). Ca^{2+} cannot support catalysis and acts as an inhibitor by competing with the essential Mg^{2+}. The divalent metal ion, Cu^{2+}, does not catalyze the cleavage of DNA by EcoRI (*144*).

It is fascinating to determine the exact nature of the divalent ion coordination in order to illuminate the microscopic origins of their effects on catalysis. Figure 5-1 shows the structure of the metal-free EcoRI-DNA complex. EcoRI is a 62 kDa homodimeric protein, which contains a large relatively rigid main domain and a smaller arm region. The arm regions are disordered in the free protein but become ordered and enfold the DNA in the specific complex. Crystal structures of the post-cleavage (Mn^{2+} added in the co-crystals of EcoRI protein and DNA) complexes are also available (*145, 146*). The homodimeric-protein DNA complex contains two identical Mg^{2+} binding sites. Biochemical data and molecular dynamics simulations (*147*) have revealed that Mg^{2+} coordinates to Glu111, Asp91, Ala112 and a scissile phosphate group of the DNA backbone. This work allows a model of DNA catalysis whereby a neighboring phosphate

serves to orient the attacking nucleophilic water. At the same time Mg^{2+} polarizes the scissile phosphate group, which facilitates a nucleophilic attack to assist in the cleavage of DNA (*147*).

In this work, we exploit the paramagnetic properties of Cu^{2+} to understand the catalytic consequences of Cu^{2+} versus Mg^{2+} coordination. We employ continuous wave (CW) ESR, in combination with pulsed ESR methodology to assess information about Cu^{2+} coordination. Specifically, we use CW-ESR and Electron Spin Echo Envelope Modulation (ESEEM) to probe the interaction of the Cu^{2+} electron spin with surrounding nuclei. These experiments establish that the two coppers ions are coordinated to EcoRI histidines. The DEER technique, on the other hand, is used to obtain Cu^{2+}-based distance constraints in order to identify which histidine residue coordinates to Cu^{2+}.

The measurement of Cu^{2+}-based distances using DEER is not a trivial task. There are only a few reports on Cu^{2+}-based DEER experiments (*50, 52, 53, 116*). The earlier reports were notable in demonstrating the feasibility of Double Electron Electron Resonance and Double Quantum Coherence experiments on Cu^{2+} containing samples (*52, 116, 117*). Recent works (*51, 53, 54*) point out that it is necessary to account for the effects of partial excitation of the Cu^{2+} ESR spectrum. In this work DEER data are collected at many magnetic fields and resonance offsets (*50, 53*), to probe the effects of the partial Cu^{2+} spectrum excitation. The molecular model developed in Chapter 3 is then utilized to analyze these experimental data to extract distance information (*50, 53*).

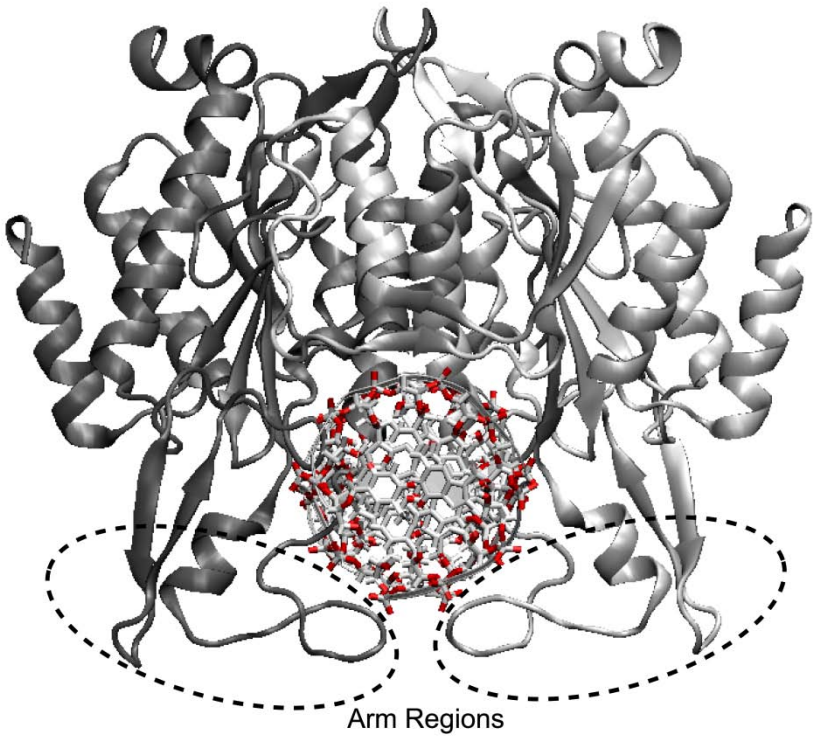

Figure 5-1. Crystal structure of the EcoRI-DNA specific complex. Monomers are shown in silver and grey. The arm regions of the EcoRI are highlighted by the circles, enfolding the specific DNA sequence. Coordinates are from a highly refined version of PDB entry 1CKQ (cf. reference 146).

5.3 MATERIALS AND METHODS

EcoRI specific complex preparation: The Cu^{2+} stock solution was prepared by dissolving the isotopically enriched $^{63}CuCl_2$ (purchased from Cambridge Isotope Laboratories, Inc.) into 30 mM N-ethylmorpholine (NEM) buffer, in a pH of 7.4. A 22 base-pair 32P end-labeled DNA substrate containing the cognate site GAATTC with the sequence of GGGCGGGCGAATTCGCGGCGC was used. The solution of wild-type EcoRI in the presence of the specific DNA site was then prepared in 30 mM NEM buffer with the same pH value. A 2:1 Cu^{2+}-to-protein molar ratio mixture was then prepared with a final concentration of 380 μM and an effective sample volume of ~110 μL. This sample will be referred to as "EcoRI specific complex".

S180C-EcoRI specific complex preparation: Mutation S180C was constructed, and the EcoRI was spin labeled with the methanethiosulfonate spin label (MTSSL), as previously described (*49*). A 22 base-pair 32P end-labeled DNA substrate containing the cognate site GAATTC with the sequence of GGGCGGGCGAATTCGCGGCGC was used. The solution of S180C mutant EcoRI in the presence of specific DNA site was then prepared in 30 mM NEM buffer with a pH of 7.4. A 2:1 Cu^{2+}-to-protein molar ratio mixture was prepared with a final concentration of ~180 μM and the effective sample volume was ~70 μL. This sample will be referred to as the "S180C-EcoRI specific complex". Both samples were stored at -80°C and flash-frozen before each experiment.

ESR experiments: All of the pulsed ESR experiments were performed on a Bruker Elexsys 580 spectrometer at 20 K. CW-ESR and ESEEM experiments were performed with a MS3 resonator. DEER experiments were performed with a MD5 resonator.

The three-pulse ESEEM signal were collected by recording the stimulated electron spin echo intensity as a function of T using the sequence: $(\pi/2)$-τ-$(\pi/2)$-T-$(\pi/2)$-τ-(stimulated echo), on the EcoRI specific complex. The duration of the $(\pi/2)$ pulses was 16 ns. The interpulse delay τ was fixed at 200 ns. The time interval T was incremented from 400 ns with a step size of 16 ns, for a total of 1024 points. A four step phase cycle was employed to eliminate unwanted signals (*101*).

DEER experiments were performed on S180C -EcoRI specific complex with the pulse sequence: $(\pi/2)_{\upsilon 1}$-τ_1-$(\pi)_{\upsilon 1}$-T-$(\pi)_{\upsilon 2}$-τ_2-$(\pi)_{\upsilon 1}$-τ_1-echo. The pulse duration of the $(\pi/2)_{\upsilon 1}$, $(\pi)_{\upsilon 1}$ and $(\pi)_{\upsilon 2}$ pulse was adjusted to be 24 ns, 48 ns and 44 ns, respectively. Interval T was incremented from 136 ns with a stepsize of 16 ns, for a total of 256 points. Proton modulation was averaged by adding traces at four different τ_1 values, starting at 200 ns and incrementing by 18 ns (*2*). Interval τ_2 was adjusted to make $(\tau+\tau_2)$ =2200 ns. A two-step phase cycling (+x,-x) is carried out on the first $(\pi/2)$ pulse.

The main frequency, υ_1, was fixed at ~9.7 GHz in the DEER experiments. The experimental magnetic field, B_0, was chosen to be lower than the maximum of the nitroxide spectrum, B_{max}, so that the magnetic field difference, $(B_{max}-B_0)$, matched the frequency offset, $\Delta\upsilon$. The pump frequency, υ_2, was set to be $\Delta\upsilon$ lower than the main frequency, so that the pump pulse excite only the nitroxide electron spins. DEER signal at four different frequency offsets, 100 MHz, 266 MHz, 408 MHz and 548 MHz were collected.

The Cu^{2+}-based DEER experiments were also performed on the wt-EcoRI specific complex, with same pulse sequence, stepsize, number of points and phase. Under a frequency offset of 100 MHz, DEER signal at four different magnetic fields, 3342 G, 3290 G, 3240 G, 3190 G and 3090

G were collected. DEER signal were also collected for different frequency offsets, of 200 MHz, 280 MHz, 392 MHz and 500 MHz.

5.4 RESULTS AND DISCUSSION

CW-ESR spectrum shows two Cu^{2+} components: Cu^{2+} was mixed with the EcoRI specific complex in a 2:1 Cu^{2+}-to-protein ratio. Figure 5-2a shows the CW-ESR spectrum from this sample. The CW-ESR spectrum exhibits two separate components with $g_{\parallel} = 2.289$, $A_{\parallel} = 163\ G$ and $g_{\parallel} = 2.228$, $A_{\parallel} = 143\ G$ (cf. Figure 5-2a). CW-ESR simulations are shown in Figure 5-2a. The best fit is obtained when the ratio of the two components is ~1:1 The $A_{\parallel}$ values are within the range of type-II Cu^{2+} complexes (*121*), which indicates that both Cu^{2+} components have four equatorial ligands and two axial ligands. According to the established Peisach-Blumberg plot (*121*), the first component ($g_{\parallel} = 2.289$, $A_{\parallel} = 163\ G$) has either a 2N2O or a 3N1O binding mode in the equatorial plane. The second component does not belong to any established binding mode. The low $A_{\parallel}$ and $g_{\parallel}$ values of the second component may be caused by an irregular symmetry of the Cu^{2+} coordination (*148*).

ESEEM determines that Cu^{2+} is coordinated to a histidine: Figure 5-2b shows the three-pulse ESEEM spectrum obtained at a magnetic field of 3369 G, which corresponds to the $g_{\perp}$ region of the Cu^{2+} ESR spectrum. Peaks at 0.6 MHz, 1.0 MHz and 1.6 MHz are characteristic of the histidine coordination and are due to the interaction of Cu^{2+} unpaired electron with a remote ^{14}N of a histidine imidazole ring (*118, 149-152*). These peaks arise from transitions that involve the nuclear quadrupolar interaction of the ^{14}N spin. Two broad peaks at 3.8 MHz and 4.5 MHz are also resolved. These two peaks are assigned to the double quantum transition of

remote ^{14}N nuclei. The peak at 14.8 MHz is due to hyperfine interaction between the Cu^{2+} electron spins and remote protons. Protons that contribute to this peak may come from either the solvent or the protein. ESEEM results indicate that Cu^{2+} is coordinated to a histidine residue of EcoRI. There are five histidines in each subunit of EcoRI at positions 31, 114, 147, 162 and 225. In order to identify which histidine binds to Cu^{2+}, we decided to measure the distance between the two Cu^{2+} centers (one in each subunit of EcoRI).

Cu^{2+}-Cu^{2+} distance rules out His31 and His147: Figure 5-3a shows the DEER signal collected on the Cu^{2+} bound EcoRI specific complex at several magnetic fields. Such magnetic field dependent data are important for the case of Cu^{2+} DEER. The duration of the microwave pulses used in the DEER experiments are generally in the 10's of nanoseconds. This can lead to the excitation of those Cu^{2+} electron spins whose interspin vectors are appropriately oriented with respect to the main magnetic field (*99*). Such orientational selectivity makes the direct inversion of the DEER data to obtain distances problematic. The proper procedure is to perform DEER experiments at different magnetic fields. Alternatively the data may be collected at different resonance offsets – i.e. for different separations in the frequencies of the pump pulse versus the probe pulse in this double resonance experiment (*1*). The field and/or resonance offset variation of the DEER signal is used to obtain information about Cu^{2+}-Cu^{2+} distance as well as the relative orientation of the two Cu^{2+} centers (*50, 53*). For these reasons, we collected the DEER signal at 3342 G (the $g_{\perp}$ region), 3290 G, 3240 G, 3190 G and 3090 G (the $g_{\parallel}$ region) with a fixed resonance offset of 100 MHz.

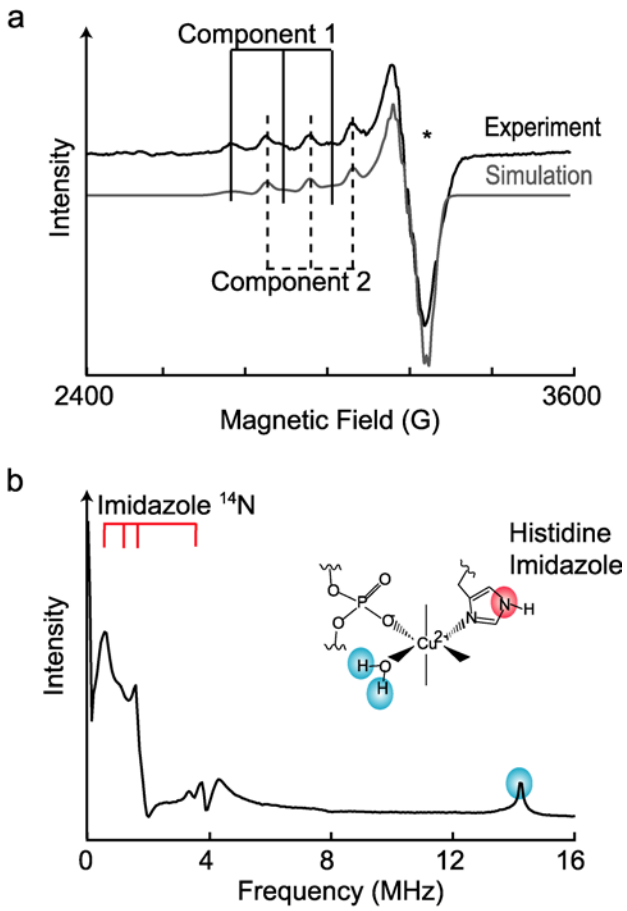

Figure 5-2. (a) The CW-ESR spectrum of Cu^{2+} bound EcoRI specific complex at 80 K. Two components are detected in the spectrum, as labeled by vertical bars named "Component 1" and "Component 2". The spectrum was simulated and shown by the grey line. The line width applied was ~15 G for the first component and ~60 G for the second component. The relative ratio of the two components is ~1:1. Position "*" illustrates the magnetic field where the ESEEM spectrum in (b) was collected. (b) Three-pulse ESEEM spectrum at 20 K. The sharp peaks at 0-2 MHz, as indicated by the red bars, are assigned to the imidazole ^{14}N from a histidine residue. The broad peaks at ~3.8 MHz and 4.5 MHz are preliminarily assigned to the double quantum transition of the ^{14}N nuclei. The peak at ~ 14 MHz, as labeled by blue, is assigned to the proton ESEEM peak. (Inset) The Cu^{2+} coordination derived from the ESEEM results. The remote nuclei that contribute to the ESEEM signal are highlighted with the corresponding colors.

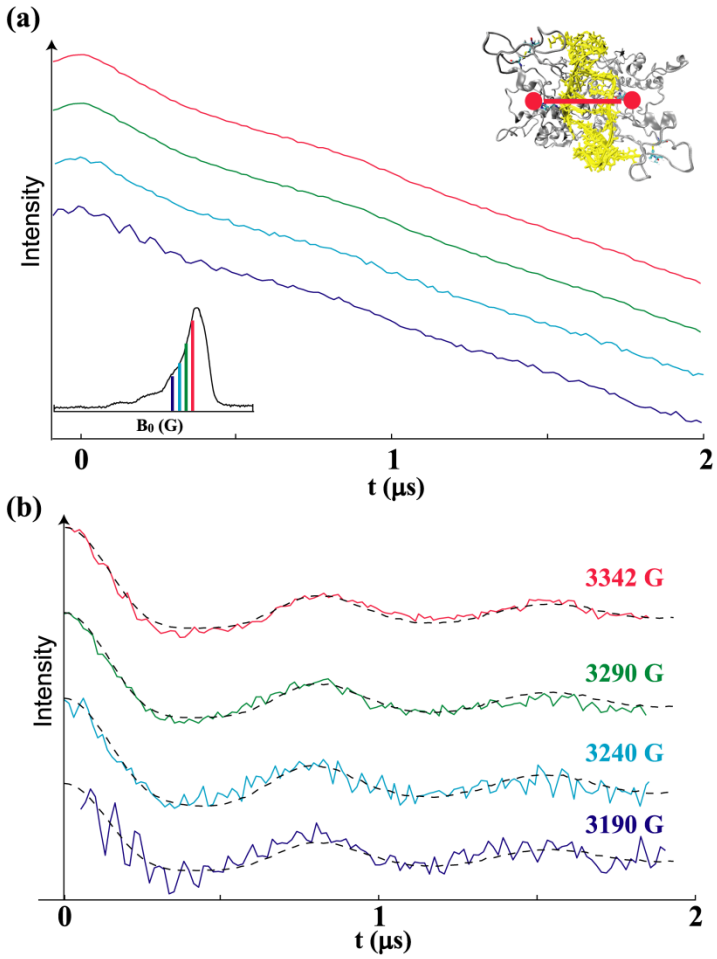

Figure 5-3. (a) The unprocessed DEER data on Cu^{2+} bound EcoRI specific complex at four different magnetic fields, at 20 K. The relative positions of these magnetic fields are color coded on the field-swept echo detected spectrum shown in the left inset. (right inset) Illustration of the Cu^{2+}-Cu^{2+} distance measured in the DEER experiment. (b) Baseline corrected DEER signal at four different magnetic fields. A distinct modulation appears at ~500 ns and lasts for more than 2 modulation periods for every data set. The fast modulation at 3240 G, 3190 G and 3090 G is due to the proton ESEEM effect. The dashed lines represent the fit from the optimized parameters based on the model shown in Figure 5-4a.

An intramolecular dipolar modulation can be clearly observed by a visual inspection of the unprocessed signal in each data set. The modulation depth was determined to be ~1-2%, depending on the magnetic field and resonance offset. The low modulation depth is consistent with theoretical calculations under our experimental conditions (*1*). The background signal, which is due to the intermolecular dipolar interaction, was corrected with a stretched exponential function. After baseline correction, we observed a clean intramolecular dipolar modulation lasting over 2 periods from each data set. These data are shown in Figure 5-3b. No significant magnetic field or resonance offset dependence of the baseline corrected signal was observed at the $g_{\perp}$ region. The modulation period of the data collected at the $g_{\parallel}$ region, i.e. at 3090 G, deviated from the other data sets by ~60 ns, showing weak orientational selectivity.

To obtain the Cu^{2+}-Cu^{2+} distance from the DEER signal, the simple molecular model and the fitting procedure developed in Chapter 3 were applied to this complex (cf. Figure 5-4a). The optimized parameters were determined to be R=35 Å. Best fit were for orientational angles of (χ, γ, η)= (30°, 90, 0º). The distribution width of each angle was 10º (we obtained similar results for σ from 5° to 15°). The specificity of this parameter set was also confirmed using the method shown in Chapter 3 (cf. Appendix A). The simulated signal using the optimized parameter set are shown in Figure 5-3b dotted lines. The Cu^{2+}-Cu^{2+} distance distribution was obtained from the optimized parameter set and shown in the inset to Figure 5-4a. The most probable Cu^{2+}-Cu^{2+} distance is 35 Å with a standard deviation of ~1 Å. Biochemical experiments suggest that only EcoRI dimers exist in solution in the presence of the specific DNA sites (*145*). Therefore, the distance measured can be assigned to Cu^{2+} bound to the same histidine in each subunit of the dimeric complex, or to Cu^{2+} bound to any two histidines in the complex. Table 5-1 shows distances between any two histidine residues in the EcoRI homodimer based on the crystal

strcuture of the metal-free EcoRI-DNA complex (*145, 146*). According to the DEER results, only six histidine pairs are possible to provide the measured Cu^{2+}-Cu^{2+} distance (shown by bold type in Table 5-1).

Table 5-1. Distances between histidines in EcoRI homodimer. Inter-subunit histidine-histidine distances are underlined. Cases (A) to (F) are possible histidines pairs that match experimental DEER data.

Intra-subunit / Inter-subunit	H31	H114	H147	H162	H225
H31	68 Å	22 Å	**35 Å (D)**	27 Å	50 Å
H114	48 Å	**30 Å (A)**	18 Å	25 Å	**39 Å (E)**
H147	40 Å	21 Å	7 Å	20 Å	22 Å
H162	55 Å	40 Å	22 Å	**32 Å (B)**	**26 Å (F)**
H225	43 Å	40 Å	25 Å	18 Å	**30 Å (C)**

Cu^{2+}-S180C distance shows that His114 coordinates to Cu^{2+}: In order to determine the histidines that coordinate copper ions, we decided to measure Cu^{2+}-nitroxide distances. Residue S180 was mutated to a cysteine, and the mutated EcoRI was spin labeled with the methanethiosulfonate spin label (MTSSL) as described by Stone *et. al.* (*49*). Their work also showed that the S180C mutation caused minimal perturbation to the protein structure and that the S180C spin labeled EcoRI was functionally active (*49*). The S180C spin labeled EcoRI complex was then mixed with Cu^{2+} in a 2:1 Cu^{2+}-to-protein ratio.

To selectively measure the Cu^{2+}-S180C distances, DEER signal were collected on this sample, with the pump pulse applied to the nitroxide ESR spectrum and the observer pulses applied to the Cu^{2+} ESR spectrum. To investigate the internal orientational effects, we collected

DEER data at frequency offsets of 100 MHz, 266 MHz, 408 MHz and 548 MHz, as shown in Figure 5-5a. The positions of the pump and probe pulses are shown in the inset to Figure 5-5a. For all the data sets, the modulation depth in the raw data was between ~5-10 %. This is consistent with theoretical calculations (*1*). The baselines for these data sets were corrected by using a stretched exponential function and the results are shown in Figure 5-5b. As shown in Figure 5-5b, two clear modulation periods are observed, indicating a bimodal distribution of Cu^{2+}-S180C distances.

To extract the distance information from the experimental data, the molecular model and the data analysis procedure developed in Chapter 3 was applied (*51*). The parameters in the model were optimized by fitting to the experimental data sets and the results are provided in Appendix A. The simulated DEER signal with four different frequency offsets using the optimal parameters are shown in Figure 5-5b, dotted lines. The distance distribution is shown in the inset to Figure 5-5b. The analysis of the DEER data yields a bimodal distance distribution function, with the most probable distances at 22 Å and 42 Å and the standard deviations of 2 Å and 3 Å, respectively.

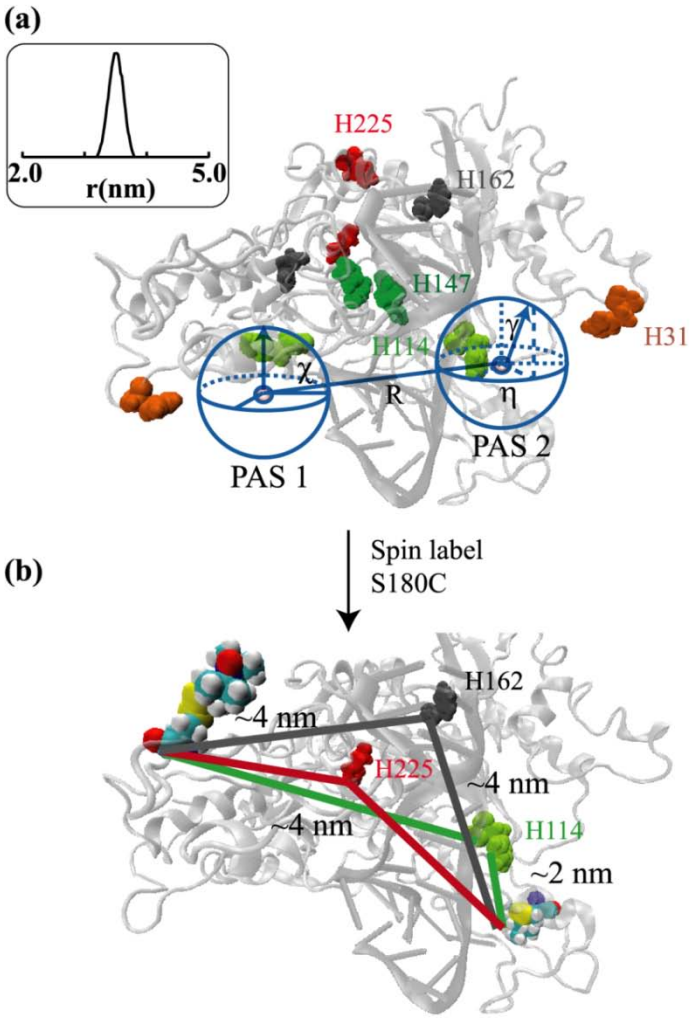

Figure 5-4. (a) Five histidine residues in each EcoRI monomer are highlighted by space-filling models using the corresponding colors. The molecular model used in the DEER simulation is also illustrated in the model, with variables defined. (Inset) The Cu^{2+}-Cu^{2+} distance distribution extracted from the molecular model. (b) Illustration of the triangulation procedure. H114 is ~ 20 Å away from the spin labeled S180C within the same monomer and ~ 40 Å away from the S180C in the other monomer (case (A). The corresponding distances are ~ 40 Å for H162 and H225 (cases (B) and (C)). Cases (D), (E) and (F) are not shown.

Table 5-2 shows the intra-subunit and inter-subunit histidine-S180 distances on the basis of the crystal structure of the metal-free EcoRI-DNA complex. Cases (B), (C), (D) and (F) are inconsistent with the experimental ~ 22 Å distance and are therefore excluded. Cases (A) and (E) contain this ~ 22 Å distance. However, our distance distribution function obtained from DEER data (cf. Figure 5-5b) shows that the relative ratio of the shorter distances (~22 Å) versus the longer distances (~42 Å) is ~ 1:1. This is consistent only with case (A) since if case (E) is true, one anticipates this ratio to be ~1:3. Therefore, the ESEEM and DEER results together provides strong evidence that H114 binds to Cu^{2+}.

Table 5-2. His-S180 distances for cases (A) to (F) in Table 5-1.

	Intra-subunit	Inter-subunit
(A) H114-S180	20 Å	40 Å
(B) H162-S180	40 Å	40 Å
(C) H225-S180	40 Å	40 Å
(D) H31-S180; H147-S180	33 Å, 29 Å	53 Å, 35 Å
(E) H114-S180; H225-S180	20 Å, 40 Å	40 Å, 52 Å
(F) H162-S180; H225-S180	36 Å, 40 Å	46 Å, 52 Å

Using Cu^{2+} as a probe, the ESR data reveal the existence of a second metal ion binding site (His114) in addition to that previously identified for Mg^{2+} (*147*). In support of a role for His114 in binding Cu^{2+}, work in the Jen-Jacobson's lab has shown that the mutant H114Y-DNA complex binds with 1600-fold lower affinity (apparent K_d, Cu^{2+} ~8 mM) than the wt-DNA complex (K_d, Cu^{2+} ~5 μM). Additionally, they observed a 1600-fold enhancement of the Mg^{2+} (0.5 mM)-catalyzed rate in the presence of a saturating concentration of Cu^{2+}. These studies thus

raise the question of whether EcoRI can also bind two Mg^{2+} ions during its normal cleavage reaction and, if so, whether the second Mg^{2+} is necessary or only accelerates catalysis.

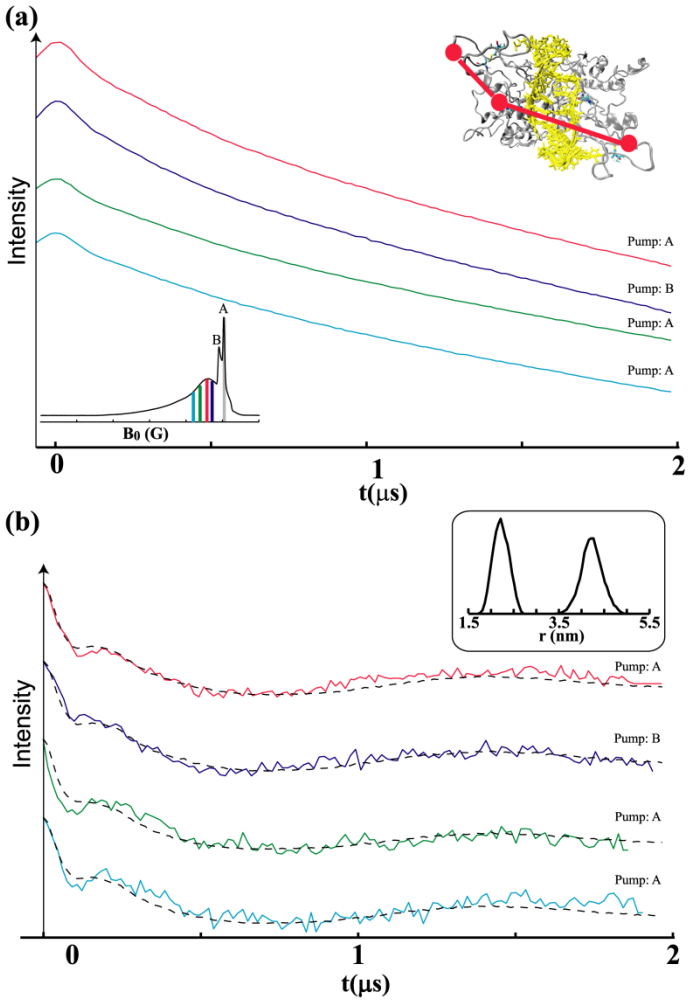

Figure 5-5. (a) The unprocessed DEER data on Cu^{2+} bound S180C-EcoRI complex at four different resonance offsets, at 20 K. The observer frequency was applied as color coded in the Cu^{2+} ESR spectrum (left inset). The pump pulse frequency was applied to two positions in the nitroxide ESR spectrum, depending on the resonance offset. (right inset) Illustration of the Cu^{2+}-S180C distance measured in the DEER experiment. (b) Baseline corrected DEER signal at four different resonance offsets. Two modulations were observed in all the data sets. The dashed lines represent the fit from the optimized parameters based on the molecular model shown in Figure 5-4a. (Inset) The bimodal distance distribution extracted from the molecular model. This result indicates that H114 binds to Cu^{2+}.

5.5 SUMMARY

We determine that Cu^{2+} is coordinated to histidine 114 of EcoRI, by using ESR spectroscopy. Specifically, CW-ESR experiment shows two Cu^{2+} components in EcoRI. The three pulse ESEEM experiments revealed that Cu^{2+} is coordinated to one histidine residue of EcoRI. To identify the Cu^{2+} binding histidine, DEER experiments were performed to measure several Cu^{2+}-based distances. A triangulation procedure based on distance constraints obtained by DEER experiments indicated that histidine 114 coordinated to Cu^{2+}. The data is novel because it reveals a second metal ion binding site in EcoRI, which has traditionally been classified as a one-metal endonuclease. Biochemical results show dramatic increase in the catalytic rate of Mg^{2+} in the presence of Cu^{2+} ions. These results raise the question of whether EcoRI can also bind two Mg^{2+} ions during its normal cleavage reaction and, if so, whether the second Mg^{2+} is necessary or only accelerates catalysis.

5.6 ACKNOWLEDGMENT

The research was supported by an NSF grant (MCB 0842956).

6.0 SUMMARY

In this thesis, the experimental procedures and data analysis routines for Cu^{2+}-based DEER measurements are established and applied to the EcoRI-DNA complex.

First, we demonstrated the possibility of Cu^{2+}-Cu^{2+} distance measurement using DEER. We presented DEER spectra of a Cu^{2+} bound proline-based peptide at four magnetic fields, at X-band. We found that the spectra do not vary appreciably with magnetic field. A molecular model was developed to analyze these DEER data. We obtained a Cu^{2+}- Cu^{2+} distance that was consistent with an earlier work. The field-independence was rationalized by the combination of two possible effects. First, the flexibility of the model peptide washed out the orientational selectivity of the Cu^{2+}-DEER spectra. Second, the Cu^{2+} g-tensor in this model peptide is in a specific orientation with respect to the interspin vector. This seems to be a stringent requirement.

To probe the origin of the field-independence of the Cu^{2+} DEER data, we performed DEER measurements on a bis-Cu^{2+}-labeled peptide and a Cu^{2+}-nitroxide labeled peptide, at several external magnetic fields and resonance offsets. Subtle but detectable orientational effects were observed from the DEER spectra of both peptides at X-band. To analyze these data, we improved the molecular model by including a distribution in the relative g-tensor orientation of the two spin centers. Using the improved model, a 30 Å mean Cu^{2+}-Cu^{2+} distance and a 27 Å mean Cu^{2+}-nitroxide distance were determined. The relative orientation of spin centers was also determined from the molecular model for both peptides. We showed that the orientational

selectivity was effectively reduced when the relative orientation of the two spin g-tensors displayed a flexibility of ~5-10º.

The orientational selectivity analysis requires high-quality data. We presented optimal experimental conditions and ESR parameters. The optimal experimental temperature is ~20 K, and the preferable sample concentration is in the range 0.1 -1.5 mM. The optimal observer π pulse length is ~20 to 48 ns and the power of the pump pulse needs to be maximized (16 ns in our case). For a Cu^{2+}-Cu^{2+} DEER measurement, the frequency offset is ~100 MHz. For a Cu^{2+}-nitroxide DEER measurement, the frequency offset is often varied in the range 100 to 500 MHz. For both cases, the pump pulse is applied at a magnetic field with a higher intensity than the observer pulses to maintain the maximum modulation depth. In addition, we showed the effects of multiple coupled spins in a Cu^{2+}-based sample on the modulation depth of DEER signal.

We applied the developed methodology to the EcoRI-DNA complex to understand the metal ion reactivity in the DNA cleavage. Three pulse ESEEM experiments revealed that Cu^{2+} was coordinated to one histidine residue of EcoRI. To identify the Cu^{2+} binding histidine, DEER experiments were performed to measure several Cu^{2+}-based distances. A triangulation procedure based on distance constraints obtained by DEER experiments indicated that histidine 114 coordinated to Cu^{2+}. The data is novel because it reveals a second metal ion binding site in EcoRI, which has traditionally been classified as a one-metal endonuclease. Biochemical results showed dramatic increase in the catalytic rate of Mg^{2+} in the presence of Cu^{2+} ions. These results raise the question of whether EcoRI can also bind two Mg^{2+} ions during its normal cleavage reaction and, if so, whether the second Mg^{2+} is necessary or only accelerates catalysis.

APPENDIX A

Data analysis for Cu^{2+} bound EcoRI-DNA complex: The procedure to optimize the variables in the model was described in our previous work (*51*) and shown in Chapter 3 of this thesis. Using this procedure, for the Cu^{2+}- Cu^{2+} DEER data shown in Figure 5-3b, we determined that the optimized fitting parameters that can fit all of the experimental data sets were R=35 Å, ΔR=1 Å, (χ, γ, η)= (30°, 90, 0°), $\sigma_\chi = \sigma_\gamma = \sigma_\eta$ =5° to 15°. The specificity of the optimized angles, χ=30°, γ=90°, η=0°, and σ=5°-15° was further examined by investigating the change of the average χ^2 values upon changing the angular parameters. Representative fittings are shown in Figures A-1 to A-3. Our results showed that the χ angle played the most important role. Figure A-1 shows the fitting of the time domain traces for three experimental data sets, by scanning χ values from 0° to 90°, using γ=90° and η=0°. The χ^2 values are listed near each data set. Both a visual inspection and the χ^2 values show that the best χ value occurs at 30°, with the corresponding χ^2 values of 0.489, 0.593, and 0.922 for the three experimental data sets. When the χ value deviated from 30°, the χ^2 value increased substantially, meaning that the best fit occurs at χ=30°. Similarly, in Figures A-2 and A-3, we show the effects of γ and η on the fitting of the experimental data. The changes in χ^2 values by changing the γ and η angles were not as significant as changing the χ values (cf. listed χ^2 values in Figures A-2 and A-3). However, different γ and η angles still provided different fits to the experimental data. For instance, as shown in Figure A-2, γ=60° can also provide good fits to experimental data sets, with the

corresponding χ^2 values of 0.503, 0.652 and 0.933, respectively. However, the average χ^2 is the lowest at γ=90°. Similarly, as shown in Figure A-3, the differences in the χ^2 using different η angles are relatively small. The average χ^2 value with η=0° is the lowest, making η=0° the best fit.

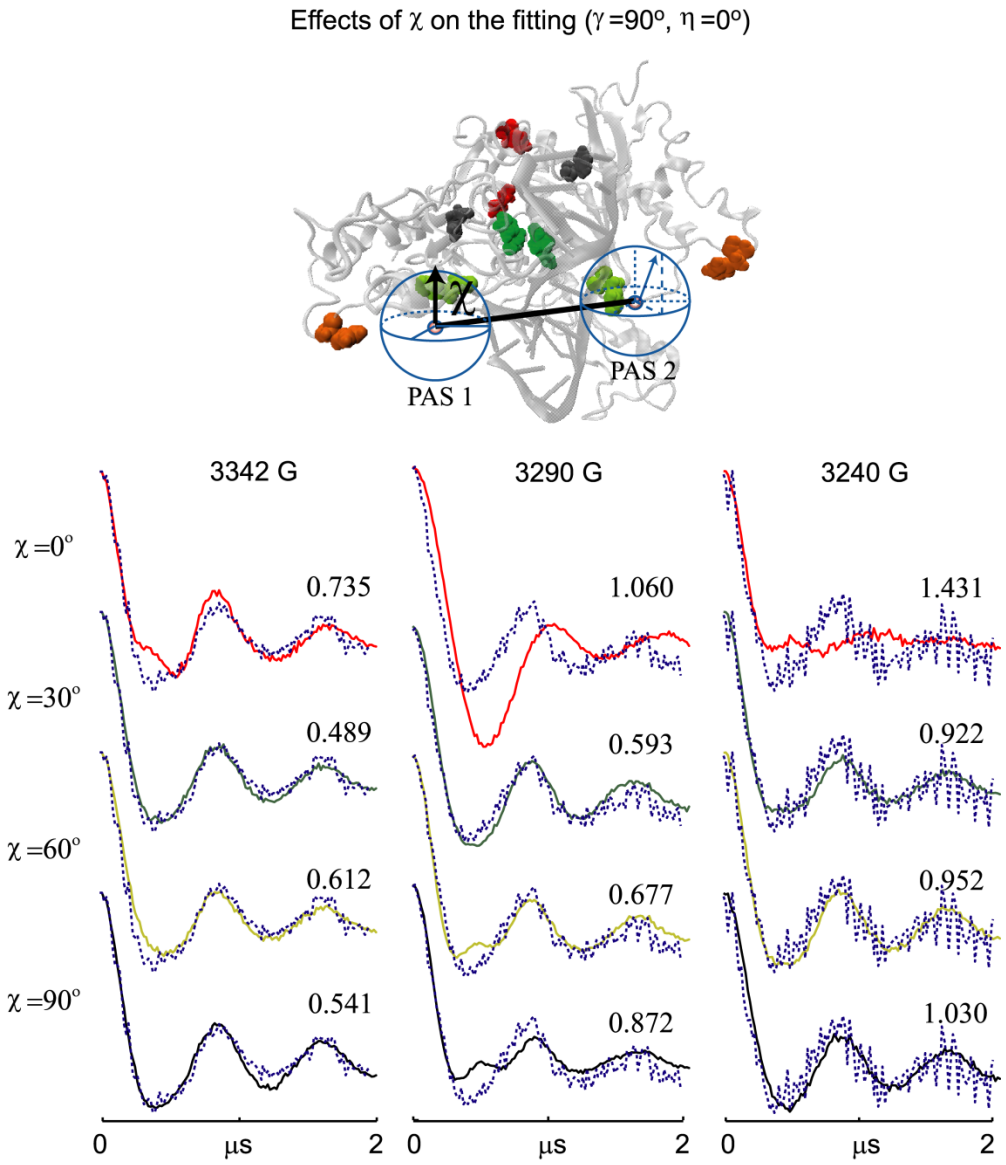

Figure A-1. Effects of the χ angle on the fitting of the three experimental data sets. The simulated DEER signal using the corresponding angles are shown in solid curves and the experimental data are shown in dotted curves. The corresponding χ^2 values are listed near the curves.

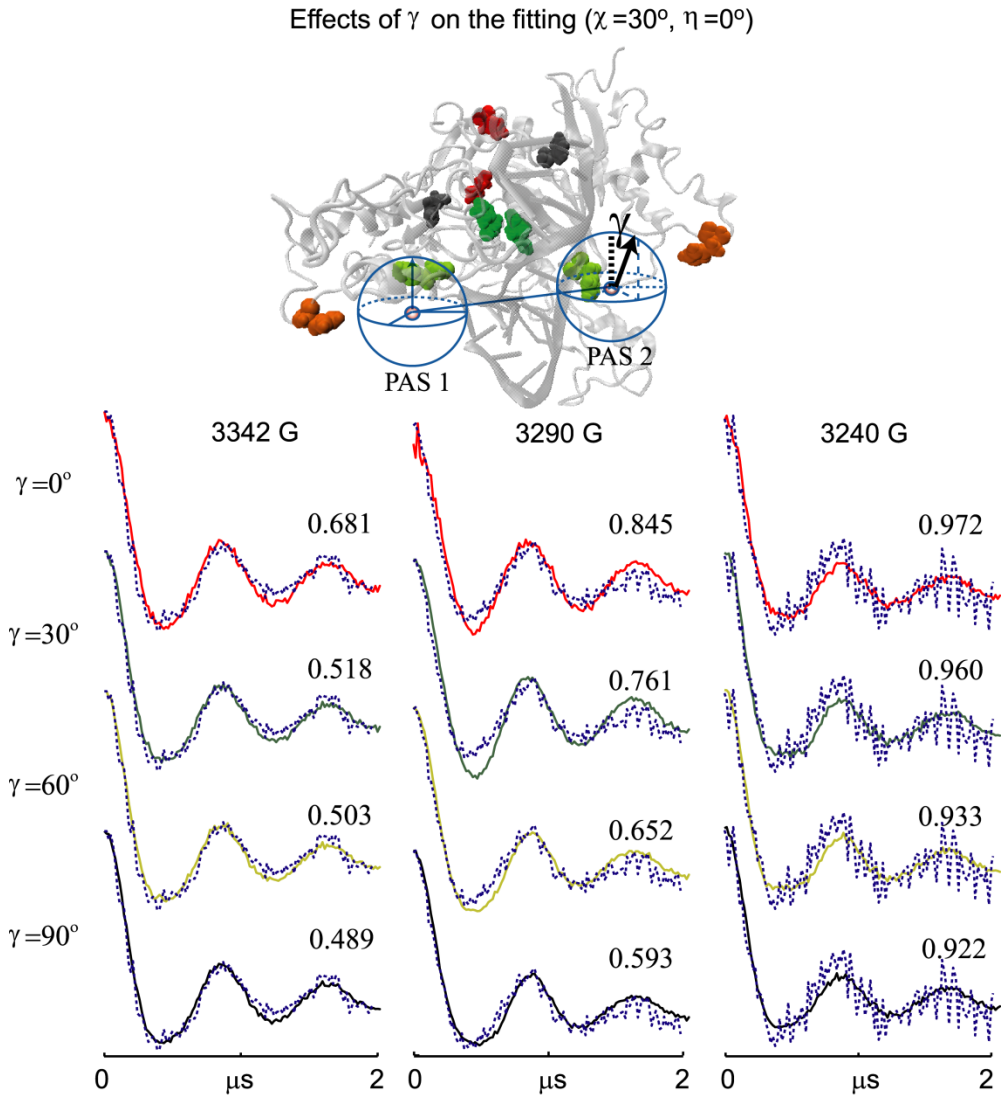

Figure A-2. Effects of the γ angle on the fitting of the three experimental data sets. The simulated DEER signal using the corresponding angles are shown in solid curves and the experimental data are shown in dotted curves. The corresponding χ^2 values are listed near the curves.

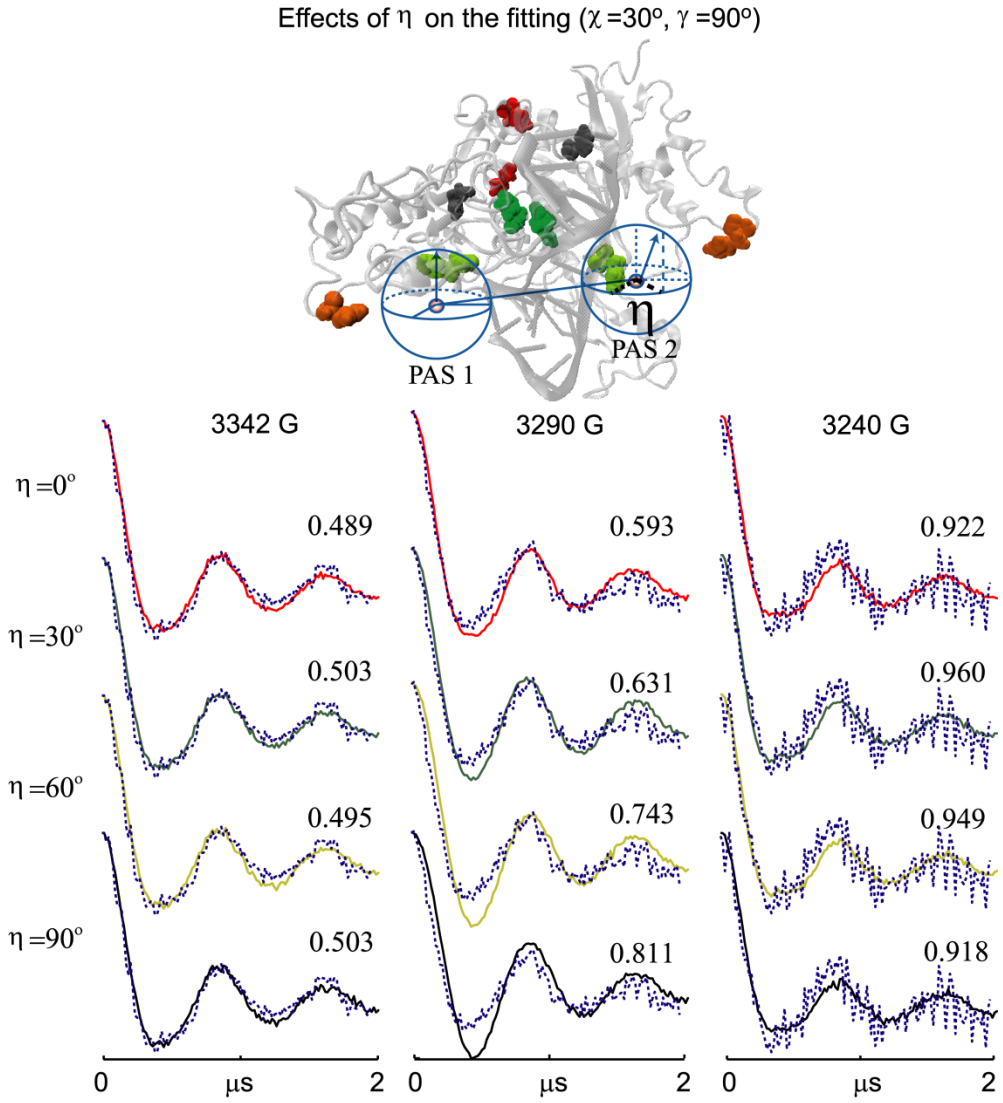

Figure A-3. Effects of the η angle on the fitting of the three experimental data sets. The simulated DEER signal using the corresponding angles are shown in solid curves and the experimental data are shown in dotted curves. The corresponding χ^2 values are listed near the curves.

Data analysis for Cu^{2+} bound S180C-EcoRI-DNA complex: The details of the fitting parameters and fitting procedures are described in our previous work (*51*). The angles describing the relative orientation of the Cu^{2+} and the nitroxide g-tensors are (χ_1, γ_1, η_1) = (30º, 0º, 0º) for the case where Cu^{2+} and the nitroxide spin label are within the same monomer of EcoRI. The angles corresponding to Cu^{2+} and the nitroxide spin label located on a different monomers of EcoRI are (χ_2, γ_2, η_2) = (30º, 60º, 30º). The specificity of these angles was investigated by using the same procedure as shown for the case of Cu^{2+}-Cu^{2+} DEER data. Figure A-4 shows the fitting of the time domain traces for three experimental data sets, by scanning χ_1 values from 0° to 90°, using γ_1=0° and η_1=0°. The χ^2 values are listed near each fitting curve. Both a visual inspection and the χ^2 values show that the best χ_1 value occurs at 30°, with corresponding χ^2 values of 0.184, 0.413, and 0.881 for the three experimental data sets. When the χ value deviated from 30°, the χ^2 value increased substantially. Interestingly, the best fit to the experimental data at 448 MHz occurs at χ_1=0º. However, the average χ^2 value is the lowest for the case of χ_1=30º, providing the best fit to all of the experimental data sets. Similarly, the effects of γ_1 and η_1 on the fitting of the experimental data are shown in Figures A-5 to A-6. As shown in Figure A-5, γ_1=30° can provide a good fit to experimental data set with 100 MHz frequency offset, and γ_1=0° can provide a good fit to experimental data set with 448 MHz frequency offset. However, the average χ^2 value is the lowest for the case of γ_1=0º, providing the best fit to all of the experimental data sets. In addition, as shown in Figure A-6, η_1=90° can also provide a good fit to experimental data set with 448 MHz frequency offset. However, the average χ^2 value is the lowest for the case of η_1=0º, providing the best fit to all of the experimental data sets. Similar findings can be obtained for the angles of (χ_2, γ_2, η_2) (data not shown).

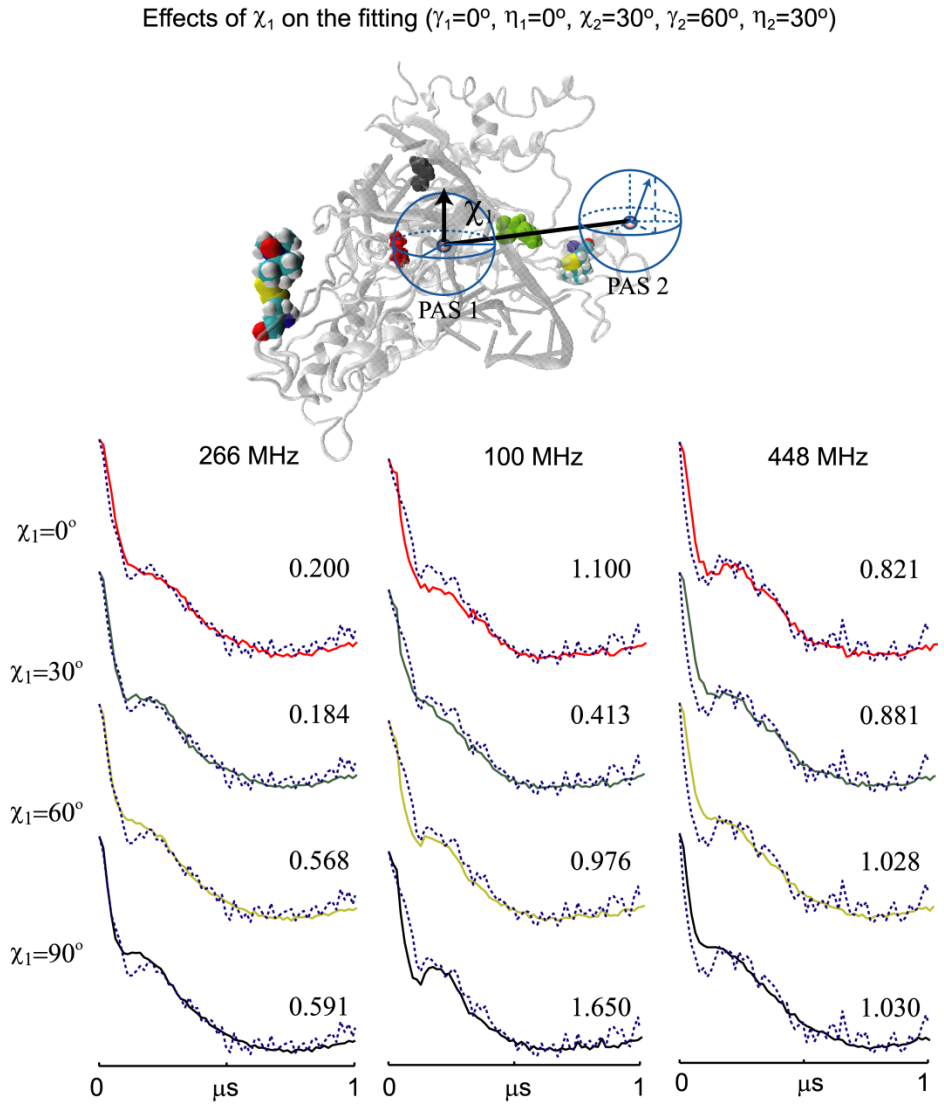

Figure A-4. Effects of the χ_1 angle on the fitting of the three experimental data sets. The simulated DEER signal using the corresponding angles are shown in solid curves and the experimental data are shown in dotted curves. The corresponding χ^2 values are listed near the curves.

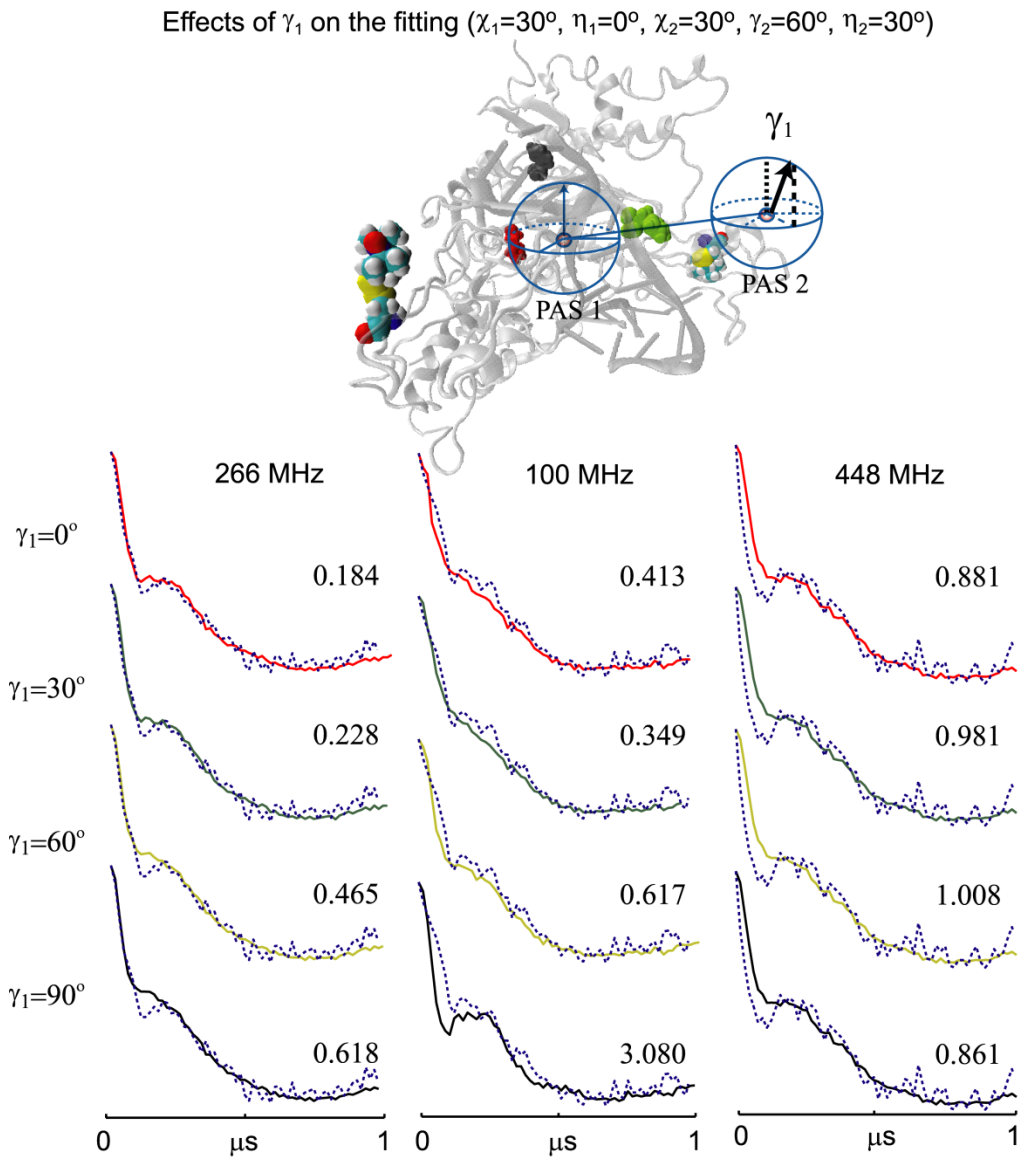

Figure A-5. Effects of the γ_1 angle on the fitting of the three experimental data sets. The simulated DEER signal using the corresponding angles are shown in solid curves and the experimental data are shown in dotted curves. The corresponding χ^2 values are listed near the curves.

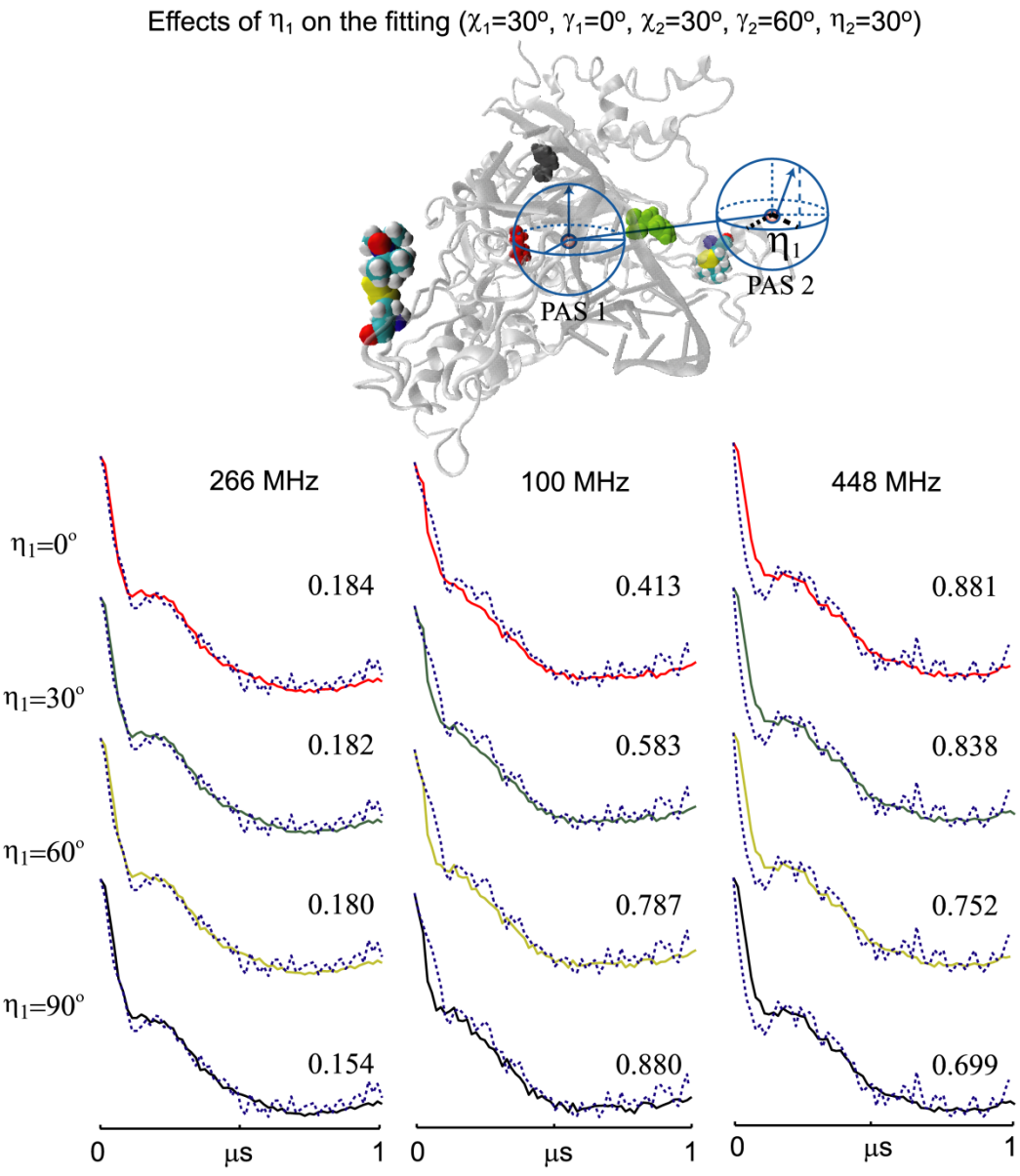

Figure A-6. Effects of the η_1 angle on the fitting of the three experimental data sets. The simulated DEER signal using the corresponding angles are shown in solid curves and the experimental data are shown in dotted curves. The corresponding χ^2 values are listed near the curves.

BIBLIOGRAPHY

1. Milov, A. D., Ponomarev, A. B., and Tsvetkov, Y. D. (1984) Electron-electron double resonance in electron spin echo: model biradical systems and the sensitized photolysis of decalin, *Chem. Phys. Lett. 110*, 67-72.

2. Larson, R. G., and Singel, D. J. (1993) Double electron-electron resonance spin-echo modulation spectroscopic measurement of electron-spin pair separations in orientationally disordered solids, *J. Chem. Phys. 98*, 5134-5146.

3. Altenbach, C., Greenhalgh, D., Khorana, H., and Hubbell, W. (1994) A collision gradient method to determine the immersion depth of nitroxides in lipid bilayers: Application to spin labeled mutants of bacteriorhodopsin, *Proc. Natl. Acad. Sci. U.S.A. 91*, 1667-1671.

4. Hubbell, W. L., Cafiso, D. S., and Altenbach, C. (2000) Identifying conformational changes with site-directed spin labeling, *Nat. Struct. Biol. 7*, 735-739.

5. Jeschke, G., Chechik, V., Ionita, P., Godt, A., Zimmermann, H., Banham, J., Timmel, C. R., Hilger, D., and Jung, H. (2006) DeerAnalysis2006 - a Comprehensive Software Package for Analyzing Pulsed ELDOR Data, *Appl. Magn. Res. 30*, 473-498.

6. Chiang, Y.-W., Borbat, P., and Freed, J. H. (2005) The determination of pair distance distributions by pulsed ESR using Tikhonov regularization, *J. Magn. Reson. 172*, 279.

7. Elsässer, C., Brecht, M., and Bittl, R. (2002) Pulsed electron-electron double resonance on multinuclear metal clusters: Assignment of spin projection factors based on the dipolar interaction, *J. Am. Chem. Soc. 124*, 12606-11611.

8. Amsterdam, I. M. C. v., Ubbink, M., Canters, G. W., and Huber, M. (2003) Measurement of a Cu-Cu Distance of 26 Å by a Pulsed EPR Method *Angew. Chem. Int. Ed. 42*, 62-64.

9. Bennati, M., Robblee, J. H., Mugnaini, V., Stubbe, J., Freed, J., and Borbat, P. (2005) EPR distance measurements support a model for long-range radical initiation in *E. coli* ribonucleotide reductase, *J. Am. Chem. Soc. 127*, 15014-15015.

10. Kawamori, A., Ono, T.-A., Ishii, A., Nakazawa, S., Hara, H., T. Tomo, Minagawa, J., Bittl, R., and Dzuba, S. A. (2005) The functional sites of chlorophylls in D1 and D2 subunits of Photosystem II identified by pulsed EPR, *Photosynth. Res. 84*, 187-192.

11. Astashkin, A. V., Seravalli, J., Mansoorabadi, S. O., Reed, G. H., and Ragsdale, S. W. (2006) Pulsed electron paramagnetic resonance experiments identify the paramagnetic intermediates in the pyruvate ferredoxin oxidoreductase catalytic cycle, *J. Am. Chem. Soc. 128*, 3888-3889.

12. Banham, J. E., Timmel, C. R., Abbott, R. J. M., Lea, S. M., and Jeschke, G. (2006) The characterization of weak protein-protein interactions: Evidence from DEER for the trimerization of a von Willebrand Factor A domain in solution, *Angew. Chem. Int. Ed. 45*, 1058-1061.

13. Fajer, P. G., Gyimesi, M., Málnási-Csizmadia, A., Bagshaw, C. R., Sen, K. I., and Song, L. (2007) Myosin cleft closure by double electron–electron resonance and dipolar EPR, *J. Phys: Condens. Matter. 19*, 1-10.

14. Denysenkov, V. P., Biglino, D., Lubitz, W., Prisner, T. F., and Bennati, M. (2008) Structure of the Tyrosyl Biradical in Mouse R2 Ribonucleotide Reductase from High-Field PELDOR, *Angew. Chem. Int. Ed. 47*, 1224-1227.

15. Klein, J. C., Burr, A. R., Svensson, B., Kennedy, D. J., Allingham, J., Titus, M. A., Rayment, I., and Thomas, D. D. (2008) Actin-binding cleft closure in myosin II probed by site-directed spin labeling and pulsed EPR, *Proc. Natl. Acad. Sci. U.S.A. 105*, 12867–12872.

16. Swanson, M. A., Kathirvelu, V., Majtan, T., Frerman, F. E., Eaton, G. R., and Eaton, S. S. (2009) DEER Distance Measurement Between a Spin Label and a Native FAD Semiquinone in Electron Transfer Flavoprotein, *J. Am. Chem. Soc. 131*, 15978–15979.

17. Kear, J. L., Blackburn, M. E., Veloro, A. M., Dunn, B. M., and Fanucci, G. E. (2009) Subtype Polymorphisms Among HIV-1 Protease Variants Confer Altered Flap Conformations and Flexibility, *J. Am. Chem. Soc. 131*, 14650–14651.

18. Ghimire, H., McCarrick, R. M., Budil, D. E., and Lorigan, G. A. (2009) Significantly Improved Sensitivity of Q-Band PELDOR/DEER Experiments Relative to X-Band Is Observed in Measuring the Intercoil Distance of a Leucine Zipper Motif Peptide (GCN4-LZ), *Biochemistry 48*, 5782-5784.

19. Galiano, L., Blackburn, M. E., Veloro, A. M., Bonora, M., and Fanucci, G. E. (2009) Solute Effects on Spin Labels at an Aqueous-Exposed Site in the Flap Region of HIV-1 Protease, *J. Phys. Chem. B 113*, 1673–1680.

20. Galiano, L., Ding, F., Veloro, A. M., Blackburn, M. E., Simmerling, C., and Fanucci, G. E. (2009) Drug Pressure Selected Mutations in HIV-1 Protease Alter Flap Conformations, *J. Am. Chem. Soc. 131*, 430–431.

21. Schiemann, O., Piton, N., Mu, Y., Stock, G., Engels, J. W., and Prisner, T. F. (2004) A PELDOR-based nanometer distance ruler for oligonucleotides, *J. Am. Chem. Soc. 126*, 5722-5729.

22. Ward, R., Keeble, D. J., El-Mkami, H., and Norman, D. G. (2007) Distance Determination in Heterogeneous DNA Model Systems by Pulsed EPR, *ChemBioChem 8*, 1957-1864.

23. Schiemann, O., Piton, N., Plackmeyer, J., Bode, B. E., Prisner, T. F., and Engels, J. W. (2007) Spin labeling of oligonucleotides with the nitroxide TPA and use of PELDOR, a pulse EPR method, to measure intramolecular distances, *Nat. Protoc. 2*, 904-923.

24. Qin, P. Z., Haworth, I. S., Cai, Q., Kusnetzow, A. K., Grant, G. P. G., Price, E. A., Sowa, G. Z., Popova, A., Herreros, B., and He, H. (2007) Measuring nanometer distances in nucleic acids using a sequence-independent nitroxide probe, *Nat. Protoc. 2*, 2354-2365.

25. Sicoli, G., Mathis, G., Delalande, O., Boulard, Y., Gasparutto, D., and Gambarelli, S. (2008) Double Electron-Electron Resonance (DEER): A Convenient Method To Probe DNA Conformational Changes, *Angew. Chem. Int. Ed. 47*, 735-737.

26. Kuznetsov, N. A., Milov, A. D., Koval, V. V., Samoilova, R. I., Grishin, Y. A., Knorre, D. G., Tsvetkov, Y. D., Fedorova, O. S., and Dzuba, S. A. (2009) PELDOR study of conformations of double-spin-labeled single- and double-stranded DNA with non-nucleotide inserts, *Phys. Chem. Chem. Phys. 11*, 6826 - 6832.

27. Milov, A. D., Maryasov, A. G., Tsvetkov, Y. D., and Raap, J. (1999) Pulsed ELDOR in spin-labeled polypeptides, *Chem. Phys. Lett. 303*, 135-143.

28. Pannier, M., Schöps, M., Schädler, V., Wiesner, U., Jeschke, G., and Spiess, H. W. (2001) Characterization of Ionic Clusters in Different Ionically Functionalized Diblock Copolymers by CW EPR and Four-Pulse Double Electron−Electron Resonance, *Macromolecules 34*, 5555-5560.

29. Pornsuwan, S., Bird, G., Schafmeister, C., and Saxena, S. (2006) Flexibility and lengths of bis-peptide nanostructures by electron spin resonance, *J. Am. Chem. Soc. 128*, 3876-3877.

30. Bode, B. E., Margraf, D., Plackmeyer, J., Dürner, G., Prisner, T. F., and Schiemann, O. (2007) Counting the Monomers in Nanometer-Sized Oligomers by Pulsed Electron-Electron Double Resonance, *J. Am. Chem. Soc. 129*, 6736-6745.

31. Margraf, D., Bode, B. E., Marko, A., Schiemann, O., and Prisner, T. F. (2008) Conformational flexibility of nitroxide biradicals determined by X-band PELDOR experiments, *Mol. Phys. 105*, 2153–2160.

32. Lovett, J. E., Hoffmann, M., Cnossen, A., Shutter, A. T. J., Hogben, H. J., Warren, J. E., Pascu, S. I., Kay, C. W. M., Timmel, C. R., and Anderson, H. L. (2009) Probing Flexibility in Porphyrin-Based Molecular Wires Using Double Electron Electron Resonance, *J. Am. Chem. Soc. 131*, 13852–13859.

33. Gordon-Grossman, M., Gofman, Y., Zimmermann, H., Frydman, V., Shai, Y., Ben-Tal, N., and Goldfarb, D. (2009) A Combined Pulse EPR and Monte Carlo Simulation Study Provides Molecular Insight on Peptide-Membrane Interactions, *J. Phys. Chem. B 113*, 12687–12695.

34. Gulla, S. V., Sharma, G., Borbat, P., Freed, J. H., Ghimire, H., Benedikt, M. R., Holt, N. L., Lorigan, G. A., Rege, K., Mavroidis, C., and Budil, D. E. (2009) Molecular-Scale Force Measurement in a Coiled-Coil Peptide Dimer by Electron Spin Resonance, *J. Am. Chem. Soc. 131*, 5374–5375.

35. Park, S.-Y., Borbat, P. P., Gonzalez-Bonet, G., Bhatnagar, J., Pollard, A. M., Freed, J. H., Bilwes, A. M., and Crane, B. R. (2006) Reconstruction of the chemotaxis receptor–kinase assembly, *Nat. Struct. Biol. 13*, 400-407.

36. Borovykh, I. V., Ceola, S., Gajula, P., Gast, P., Steinhoff, H.-J. r., and Huber, M. (2006) Distance between a native cofactor and a spin label in the reaction centre of Rhodobacter sphaeroides by a two-frequency pulsed electron paramagnetic resonance method and molecular dynamics simulations, *J. Magn. Reson. 180* 178–185.

37. Hilger, D., Polyhach, Y., Padan, E., Jung, H., and Jeschke, G. (2007) High-Resolution Structure of a Na+/H+ Antiporter Dimer Obtained by Pulsed Electron Paramagnetic Resonance Distance Measurements, *Biophys. J. 93*, 3675-3683.

38. Milov, A. D., Tsvetkov, Y. D., Gorbunov, E. Y., Mustaeva, L. G., Ovchinnikova, T. V., Handgraaf, J.-W., and Raap, J. (2007) Solvent Effects on the Secondary Structure of the Membrane-Active Zervamicin Determined by PELDOR Spectroscopy, *Chemistry & Biodiversity 4*, 1243-1255.

39. Vamvouka, M., Cieslak, J., Eps, N. V., Hubbell, W., and Gross, A. (2008) The structure of the lipid-embedded potassium channel voltage sensor determined by double-electron–electron resonance spectroscopy, *Protein Sci. 17*, 506–517.

40. Upadhyay, A. K., Borbat, P. P., Wang, J., Freed, J. H., and Edmondson, D. E. (2008) Determination of the Oligomeric States of Human and Rat Monoamine Oxidases in the Outer Mitochondrial Membrane and Octyl â-D-Glucopyranoside Micelles Using Pulsed Dipolar Electron Spin Resonance Spectroscopy, *Biochemistry 47*, 1554-1566.

41. Kim, M., Xu, Q., Murray, D., and Cafiso, D. S. (2008) Solutes Alter the Conformation of the Ligand Binding Loops in Outer Membrane Transporters, *Biochemistry 47*, 670-679.

42. Altenbach, C., Kusnetzow, A. K., Ernst, O. P., Hofmann, K. P., and Hubbell, W. L. (2008) High-resolution distance mapping in rhodopsin reveals the pattern of helix movement due to activation, *Proc. Natl. Acad. Sci. U.S.A. 105*, 7439-7444.

43. Zou, P., Bortolus, M., and Mchaourab, H. S. (2009) Conformational Cycle of the ABC Transporter MsbA in Liposomes: Detailed Analysis Using Double Electron–Electron Resonance Spectroscopy, *J. Mol. Biol. 393*, 586–597.

44. Meyer, S., Böhme, S., Krüger, A., Steinhoff, H.-J., Klare, J. P., and Wittinghofer, A. (2009) Kissing G Domains of MnmE Monitored by X-Ray Crystallography and Pulse Electron Paramagnetic Resonance Spectroscopy, *PLoS Biology 7*, 1-15.

45. Herrick, D. Z., Kuo, W., Huang, H., Schwieters, C. D., Ellena, J. F., and Cafiso, D. S. (2009) Solution and Membrane-Bound Conformations of the Tandem C2A and C2B Domains of Synaptotagmin 1: Evidence for Bilayer Bridging, *J. Mol. Biol. 390*, 913-923.

46. Hagelueken, G., Ingledew, W. J., Huang, H., Petrovic-Stojanovska, B., Whitfield, C., ElMkami, H., Schiemann, O., and Naismith, J. H. (2009) PELDOR Spectroscopy Distance Fingerprinting of the Octameric Outer-Membrane Protein Wza from Escherichia coli, *Angew. Chem. Int. Ed. 48*, 2904 –2906.

47. Dockter, C., Volkov, A., Bauer, C., Polyhach, Y., Joly-Lopez, Z., Jeschke, G., and Paulsen, H. (2009) Refolding of the integral membrane protein light-harvesting complex II monitored by pulse EPR, *Proc. Natl. Acad. Sci. U.S.A. 106*, 18485–18490.

48. Sen, K. I., Logan, T. M., and Fajer, P. G. (2007) Protein Dynamics and Monomer-Monomer Interactions in AntR Activation by Electron Paramagnetic Resonance and Double Electron-Electron Resonance, *Biochemistry 46*, 11639-11649.

49. Stone, K. M., Townsend, J. E., Sarver, J., Sapienza, P. J., Saxena, S., and Jen-Jacobson, L. (2008) Electron Spin Resonance Shows Common Structural Features for Different Classes of EcoRI-DNA Complexes, *Angew. Chem. Int. Ed. 47*, 1-4.

50. Yang, Z., Becker, J., and Saxena, S. (2007) On Cu(II)-Cu(II) distance measurements using pulsed electron electron double resonance, *J. Magn. Reson. 188*, 337-343.

51. Yang, Z., Kise, D., and Saxena, S. (2010) An approach towards the measurement of nanometer range distances based on Cu^{2+} ions and ESR, *J. Phys. Chem. B 114* 6165–6174.

52. Narr, E., Godt, A., and Jeschke, G. (2002) Selective measurements of a nitroxide-nitroxide separation of 5 nm and a nitroxide-copper separation of 2.5 nm in a terpyridine based copper(II) complex by pulse EPR spectroscopy, *Angew. Chem. Intl. Ed. 41*, 3907-3910.

53. Bode, B. E., Plackmeyer, J., Prisner, T. F., and Schiemann, O. (2008) PELDOR Measurements on a Nitroxide-Labeled Cu(II) Porphyrin: Orientation Selection, Spin-Density Distribution, and Conformational Flexibility, *J. Phys. Chem. A 112*, 5064-5073.

54. Lovett, J. E., Bowen, A. M., Timmel, C. R., Jones, M. W., Dilworth, J. R., Caprotti, D., Bell, S. G., Wong, L. L., and Harmer, J. (2009) Structural information from orientationally selective DEER spectroscopy, *Phys. Chem. Chem. Phys. 11*, 6840-6848.

55. Kay, C. W. M., Mkami, H. E., Cammack, R., and Evans, R. W. (2007) Pulsed ELDOR Determination of the Intramolecular Distance between the Metal Binding Sites in Dicupric Human Serum Transferrin and Lactoferrin, *J. Am. Chem. Soc. 129*, 4868-4869.

56. Milikisyants, S., Scarpelli, F., Finiguerra, M. G., Ubbink, M., and Huber, M. (2009) A pulsed EPR method to determine distances between paramagnetic centers with strong spectral anisotropy and radicals: The dead-time free RIDME sequence, *J. Magn. Reson. 201*, 48-56.

57. Roessler, M. M., King, M. S., Robinson, A. J., Armstrong, F. A., Harmer, J., and Hirst, J. (2010) Direct assignment of EPR spectra to structurally defined iron-sulfur clusters in complex I by double electron–electron resonance, *Proc. Natl. Acad. Sci. U.S.A. 107*, 1930–1935.

58. Altenbach, C., Flitsch, S. L., Khorana, H. G., and Hubbell, W. L. (1989) Structural studies of transmembrane proteins. 2. Spin labeling of bacteriorhodopsin mutants at unique cysteines, *Biochemistry 28*, 7806-7812.

59. Cornish, V., Benson, D., Altenbach, C., Hideg, K., Hubbell, W., and Schultz, P. (1994) Site-specific incorporation of biophysical probes into proteins, *Proc. Natl. Acad. Sci. U.S.A. 91*, 2910-2914.

60. Hubbell, W., Gross, A., Langen, R., and Lietzow, M. (1998) Recent advances in site-directed spin labeling of proteins, *Curr. Opin. Struct. Biol. 8*, 649-656.

61. Yang, K., Farrens, D., Altenbach, C., Farahbakhsh, Z., Hubbell, W., and Khorana, H. (1996) Structure and function in rhodopsin. Cysteines 65 and 316 are in proximity in a rhodopsin mutant as indicated by disulfide formation and interactions between attached spin labels, *Biochemistry 35*, 14040-14046.

62. Shin, Y.-K., Levinthal, C., Levinthal, F., and Hubbell, W. (1993) Colicin E1 binding to membranes: Time-resolved studies of spin-labeled mutants, *Science 259*, 960-963.

63. Farrens, D. L., Altenbach, C., Yang, K., Hubbell, W., and Khorana, H. (1996) Requirement of rigid-body motion of transmembrane helices for light activation of rhodopsin, *Science 274*, 768-770.

64. Mchaourab, H. S., Lietzow, M., Hideg, K., and Hubbell, W. (1996) Motion of spin-labeled side chains in T4 lysozyme. Correlation with protein structure and dynamics, *Biochemistry 35*, 7692-7704.

65. Todd, A. P., Cong, J., Levinthal, F., Levinthal, C., and Hubbell, W. L. (1989) Site-Directed Mutagenesis of Colicin E1 Provides Specific Attachment Sites for Spin Labels Whose Spectra are Sensitive to Local Conformation, *Proteins 6*, 294-305.

66. Mchaourab, H. S., Oh, K. J., Fang, C. J., and Hubbell, W. L. (1997) Conformation of T4 lysozyme in solution. Hinge-bending motion and the substrate-induced conformational transition studied by site-directed spin labeling, *Biochemistry 36*, 307-316.

67. Mollaaghababa, R., Steinhoff, H., Hubbell, W., and Khorana, H. (2000) Time-resolved site-directed spin-labeling studies of bacteriorhodopsin: Loop-specific conformational changes in M, *Biochemistry 39*, 1120-1127.

68. Perozo, E., Cortes, D. M., Sompornpisut, P., Kloda, A., and Martinac, B. (2002) Open channel structure of MscL and the gating mechanism of mechanosensitive channels, *Nature 418*, 942-948.

69. Liu, Y.-S., Sompornpisut, P., and Perozo, E. (2001) Structure of the KcsA channel intracellular gate in the open state, *Nat. Struc. Bio. 8*, 883-887.

70. Ottemann, K. A., Thorgeirsson, T. E., Kolodziej, A. F., Shin, Y.-K., and Jr., D. E. K. (1998) Direct measurement of small ligand-induced conformational changes in the aspartate chemoreceptor using EPR, *Biochemistry 37*, 7062.

71. Fanucci, G., Lee, J., and Cafiso, D. (2003) Membrane mimetic environments alter the conformation of the outer membrane protein BtuB, *J. Am. Chem. Soc. 125*, 13932-13933.

72. Qin, P., Hideg, K., Feigon, J., and Hubbell, W. (2003) Monitoring RNA base structure and dynamics using site-directed spin labeling, *Biochemistry 42*, 6772-6783.

73. Qin, P., Z., J. F., and Hubbell, W. L. (2005) Site-directed Spin Labeling Studies Reveal Solution Conformational Changes in a GAAA Tetraloop Receptor upon Mg^{2+}-dependent Docking of a GAAA Tetraloop, *J. Mol. Biol. 351*, 1-8.

74. Grant, G. P. G., and Qin, P. Z. (2007) A facile method for attaching nitroxide spin labels at the 5' terminus of nucleic acids, *Nucleic Acids Research 35*, 1-8.

75. Jeschke, G. (2002) Determination of the nanostructure of polymer materials by Electron Paramagnetic Resonance spectroscopy, *Macromolecul. Rapid Commun. 23*, 227-246.

76. Schweiger, A., and Jeschke, G. (2001) *Principles of Pulse Electron Paramagnetic Resonance*, Oxford University Press.

77. Eaton, S., More, K., Sawant, B., and Eaton, G. (1983) Use of the half-field transition to determine the interspin distance and the orientation of the interspin vector in systems with two unpaired electrons, *J. Am. Chem. Soc 105*, 6560-6567.

78. Eaton, S., and Eaton, G. (1982) Measurement of spin-spin distances from the intensity of the EPR half-field transition, *J. Am. Chem. Soc 104*, 5002-5003.

79. Bloembergen, N., Purcell, E. M., and Pound, R. V. (1948) Relaxation Effects in Nuclear Magnetic Resonance Absorption, *Phys. Rev. 73*, 679-712.

80. Bloembergen, N. (1949) On the interaction of nuclear spins in a crystalline lattice, *Physica 15*, 386-426.

81. Bloembergen, N., Shapiro, S., Pershan, P. S., and Artman, J. O. (1959) Cross-relaxation in spin system, *Phys. Rev. 114*, 445-459.

82. Kulikov, A. V., and Likhtenshtein, G. I. (1977) The use of spin relaxation phenomena in the investigation of the structure of model and biological systems by the method of spin labels, *Adv. Mol. Relax. and Interact. Proc. 10*, 47-69.

83. Kulikov, A. V., and Likhtenshtein, G. I. (1974) Use of saturation curves for evaluating distances in biological objects by the method of double spin labels, *Biofizika 19*, 420-424.

84. Kulikov, A. V. (1976) Determination of the distance between the spins of the spin-label and paramagnetic center in spin-labeled proteins from the saturation curve parameters of EPR spectra of the labels at 77 K, *Mol. Biol. (Moscow) 10*, 132-141.

85. Saxena, S., and Freed, J. (1997) Theory of double quantum two-dimensional electron spin resonance with application to distance measurements, *J. Chem. Phys. 107*, 1317.

86. Borbat, P. P., and Freed, J. H. (1999) Multiple-quantum ESR and distance measurements, *Chem. Phys. Lett. 313*, 145-154.

87. Larsen, R. G., and Singel, D. J. (1993) Double electron-electron resonance spin-echo modulation: Spectroscopic measurement of electron spin pair separations in orientationally disordered solids, *Journal of Chemical Physics 98*, 5134-5146.

88. Borbat, P. P., Mchourab, H. S., and Freed, J. H. (2002) Protein Structure determination using long-distance constraints from double-quantum coherence ESR: Study of T4 Lysozyme, *J. Am. Chem. Soc. 124*, 5304-5314.

89. Saxena, S., and Freed, J. (1996) Double quantum two-dimensional Fourier transform electron spin resonance: distance measurements, *Chem. Phys. Lett. 251*, 102-110.

90. Saxena, S., and Freed, J. H. (1997) Theory of Double Quantum Two Dimensional Electron Spin Resonance with application to distance measurements, *J. Chem. Phys. 107*, 1317-1340.

91. Pake, G. E. (1948) Nuclear resonance absorption in hydrated crystals: fine structure of the proton line, *Journal of Chemical Physics 16*, 327.

92. Jeschke, G., Panek, G., Godt, A., Bender, A., and Paulsen, H. (2004) Data analysis procedures for pulse ELDOR measurements of broad distance distributions *Applied Magnetic Resonance 26*, 223-244.

93. Chiang, Y.-W., Borbat, P. P., and Freed, J. H. (2005) Maximum entropy: A complement to Tikhonov regularization for determination of pair distance distributions by pulsed ESR, *Journal of Magnetic Resonance 177*, 184-196.

94. Jeschke, G., Chechik, V., Ionita, P., Godt, A., Zimmermann, H., Banham, J., Timmel, C. R., Hilger, D., and Jung, H. (2006) DeerAnalysis2006 - a comprehensive software package for analyzing pulsed ELDOR data, *Applied Magnetic Resonance 30*, 473-498.

95. Miick, S. M., and Millhauser, G. L. (1994) Measuring Heisenberg Exchange between spin-labeled peptides using 2D ELDOR, *J. Magn. Reson., Ser. B 104*, 81.

96. Costa-Filho, A., Shimoyama, Y., and Freed, J. (2003) A 2D-ELDOR study of the liquid ordered phase in multilamellar vesicle membranes, *Biophys. J. 84*, 2619-2633.

97. I. B.-Mascher, L. E. W. LaConte, J. E. Baker, and D. D. Thomas. (1999) Myosin Light-chain domain rotates upon muscle activation but not ATP hydrolysis, *Biochemistry 38*, 12607.

98. Neese, F. (2001) Prediction of electron paramagnetic resonance g values using coupled perturbed Hartree–Fock and Kohn–Sham theory, *J. Chem. Phys. 115*, 11080-11096.

99. Maryasov, A. G., Y.D.Tsvetkov, and J.Raap. (1998) Weakly Coupled Radical Pairs in Solids:ELDOR in ESE Structure Studies, *Appl.Magn.Reson. 14*, 101-113.

100. Milov, A. D., Maryasov, A. G., and Tsvetkov, Y. D. (1998) Pulsed electron double resonance (PELDOR) and its applications in free-radicals research, *Appl. Magn. Reson. 15*, 107-143.

101. Pannier, M., Veit, S., Godt, A., Jeschke, G., and Spiess, H. W. (2000) Dead-time free measurement of dipole-dipole interactions between electron spins, *J. Magn. Reson. 142*, 331.

102. Borbat, P. P., Costa-Filho, A. J., Earle, K. A., Moscicki, J. K., and Freed, J. H. (2001) Electron spin resonance in studies of membranes and proteins, *Science 291*, 266-269.

103. Zhou, Y., Bowler, B. E., Lynch, K., Eaton, S. S., and Eaton, G. R. (2000) Interspin distances in spin-labeled Metmyoglobin variants determined by Saturation Recovery EPR, *Biophys. J. 79*, 1039-1052.

104. Borbat, P., Mchaorab, H., and Freed, J. (2002) Protein structure determination using long-distance constraints from double-quantum coherence ESR: Study of T4 lysozyme, *J. Am. Chem. Soc 124*, 5304-5314.

105. Bennati, M., Weber, A., Antonic, J., Perlstein, D. L., Robblee, J., and Stubbe, J. (2003) Pulsed ELDOR spectroscopy measures the distance between the two tyrosyl radicals in the R2 subunit of the E. coli Ribonucleotide Reductase, *J. Am. Chem. Soc. 125*, 14988-14989.

106. Jeschke, G., Wegener, C., Nietschke, M., Jung, H., and Steinhoff, H.-J. (2004) Interresidual distance determination by four-pulse Double Electron-Electron Resonance in an integral membrane protein: The Na^+/proline transporter PutP of *Escherichia coli*, *Biophys. J. 86*, 2551-2557.

107. Swamy, M. J., Ciani, L., Ge, M., Smith, A. K., Holowka, D., B. Baird, and Freed, J. H. (2006) Coexisting domains in the plasma membranes of live cells characterized by spin-label ESR spectroscopy, *Biophys. J. 90*, 4452-4465.

108. Aihara, T., Ueki, S., Nakamura, M., and Arata, T. (2006) Calcium-dependent movement of troponin I between troponin C and actin as revealed by spin-labeling EPR, *Biochem. Biophys. Res. Commun. 340*, 462-468.

109. Xu, Q., Ellena, J. F., Kim, M., and Cafiso, D. S. (2006) Substrate-dependent unfolding of the energy coupling motif of a membrane transport protein determined by double electron–electron resonance, *Biochemistry 45*, 10847-10854.

110. Schiemann, O., Weber, A., Edwards, T., Prisner, T., and Sigurdsson, S. (2003) Nanometer distance measurements on RNA using PELDOR, *J. Am. Chem. Soc. 125*, 3434-3435.

111. Borbat, P. P., Davis, J. H., Butcher, S. E., and Freed, J. H. (2004) Measurement of Large Distances in Biomolecules Using Double-Quantum Filtered Refocused Electron Spin-Echoes, *J. Am. Chem. Soc. 126*, 7746-7747.

112. Piton, N., Schiemann, O., Mu, Y., Stock, G., Prisner, T., and J. Engels. (2005) Synthesis of spin-labeled RNAs for long range distance measurements by PELDOR, *Nucleotides Nucleic Acids 24*, 771-775.

113. Godt, A., Schulte, M., Zimmermann, H., and Jeschke, G. (2006) How Flexible Are Poly(para-phenyleneethynylene)s?, *Angew. Chem. Int. Ed. 45*, 7560-7564.

114. Denysenkov, V. P., Prisner, T. F., Stubbe, J., and Bennati, M. (2006) High-field pulsed electron–electron double resonance spectroscopy to determine the orientation of the tyrosyl radicals in ribonucleotide reductase, *Proc. Natl. Acad. Sci. U.S.A. 103*, 13386–13390.

115. Polyhach, Y., Godt, A., Bauer, C., and G. Jeschke. (2007) Spin pair geometry revealed by high-field DEER in the presence of conformational distributions, *J. Magn. Reson. 185* 118–129.

116. vanAmsterdam, I. M. C., Ubbink, M., Canters, G. W., and Huber, M. (2003) Measurement of a Cu^{2+}-Cu^{2+} distance of 26 Angstroms by a pulsed EPR method, *Angew. Chem. Intl. Ed. 42*, 62-64.

117. Becker, J., and Saxena, S. (2005) Double quantum coherence electron spin resonance on coupled Cu(II)-Cu(II) electron spins, *Chem. Phys. Lett. 414*, 248.

118. Burns, C., Aronoff-Spencer, E., Dunham, C., Lario, P., Avdievich, N., Antholine, W., Olmstead, M., Vrielink, A., Gerfen, G., Peisach, J., Scott, W., and Millhauser, G. (2002) Molecular features of the copper binding sites in the octarepeat domain of the prion protein, *Biochemistry 41*, 3991-4001.

119. Aronoff-Spencer, E., Burns, C. S., Avdievich, N. I., Gerfen, G. J., Peisach, J., Antholine, W. E., Ball, H. L., Cohen, F. E., Prusiner, S. B., and Millhauser, G. L. (2000) Identification of the Cu(II) Binding Sites in the N-Terminal Domain of the Prion Protein by EPR and CD Spectroscopy, *Biochemistry 39*, 13760-13771.

120. Jeschke, G., Pannier, M., Godt, A., and Spiess, H. (2000) Dipolar spectroscopy and spin alignment in electron paramagnetic resonance, *Chem. Phys. Lett. 331*, 243-252.

121. Peisach, J., and Blumberg, W. E. (1974) Structural implications derived from the analysis of Electron Paramagnetic Resonance spectra of natural and artificial copper proteins, *Archives of Biochem and Biophys 165*, 691-708.

122. Poole, C. P. (1983) *Electron Spin Resonance: A Comprehensive Treatise on Experimental Technique.*, John Wiley&Sons, Inc, Toronto.

123. Milov, A. D., Tsvetkov, Y. D., Formaggio, F., Crisma, M., Toniolo, C., and Raap, J. (2001) The secondary structure of a membrane-modifying peptide in a supramolecular assembly studied by PELDOR and CW-ESR spectroscopies, *J. Am. Chem. Soc. 123*, 3784-3789.

124. Wong, C. G., Bottiglieri, T., and Snead, O. C., 3rd. (2003) GABA, gamma-hydroxybutyric acid, and neurological disease, *Ann Neurol 54 Suppl 6*, S3-12.

125. Berliner, L. J., Eaton, S. S., and Eaton, G. R. (2000) *Biological Magnetic Resonance*, Vol. 19, Kluwer Academic/Plenum Publisher, New York.

126. Pake, G. E. (1948) Nuclear resonance absorption in hydrated crystals: Fine structure of the proton line, *J. Chem. Phys. 16*, 327-326.

127. Milov, A. D., Ponomerev, A. B., and Tsvetkov, Y. D. (1984) Electron electron double resonance in electron spin-echo model biradical systems and the sensitezed photolysis of decalin, *Chem. Phys. Lett. 110*, 67.

128. Martin, R. E., Pannier, M., Diederich, F., Gramlich, V., Hubrich, M., and Spiess, H. W. (1998) Determination of end-to-end distances in a series of TEMPO diradicals of up to 2.8 nm length with a new four-pulse double electron electron resonance experiment, *Angew. Chem. Int. Ed. 37*, 2834-2837.

129. Endeward, B., Butterwick, J. A., MacKinnon, R., and Prisner, T. F. (2009) Pulsed Electron-Electron Double-Resonance Determination of Spin-Label Distances and Orientations on the Tetrameric Potassium Ion Channel KcsA, *J. Am. Chem. Soc. 131*, 15246-15250.

130. Gnanakaran, S., Hochstrasser, R. M., and Gacia, A. E. (2004) Nature of structural inhomogeneities on folding a helix and their influence on spectral measurements, *Proc. Natl. Acad. Sci. U.S.A. 101,* 9229-9234.

131. Schuler, B., Lipman, E. A., Steinbach, P. J., Kumke, M., and Eaton, W. A. (2005) Polyproline and the "spectroscopic ruler" revisited with single-molecule fluorescence, *Proc. Natl. Acad. Sci. U.S.A. 102,* 2754-2759.

132. Jun, S., Becker, J., Yonkunas, M., Coalson, R., and Saxena, S. (2006) Unfolding of alanine-based peptides using electron spin resonance distance measurements, *Biochemistry 45,* 11666-11673.

133. Ernst, R. R., Bodenhausen, G., and Wokaun, A. (1987) *Principles of Nuclear Magnetic Resonance in One and Two Dimensions*, Oxford.

134. Ames, W. M., and Larsen, S. C. (2009) Insight into the copper coordination environment in the prion protein through density functional theory calculations of EPR parameters, *J. Biol. Inorg. Chem. 14,* 14547–14557.

135. Pornsuwan, S., Schafmeister, C. E., and Saxena, S. (2008) Analysis of the Dynamical Flexibility of Bis-peptide Nanostructures, *J. Phys. Chem. C 112,* 1377-1384.

136. Millhauser, G. L. (2004) Copper binding in the Prion protein, *Acc. Chem. Res. 37,* 79-85.

137. Godt, A., Franzen, C., Veit, S., Enkelmann, V., Pannier, M., and Jeschke, G. (2000) EPR Probes with well-defined, long distances between two or three unpaired electrons, *J. Org. Chem 65,* 7575-7582.

138. Yang, Z., Ji, M., Mehta, P., Jen-Jacobson, L., and Saxena, S. (2010) Insights on copper coordination and reactivity of restriction endonuclease EcoRI by ESR spectroscopy and modeling, *in preparation for submission to Proc. Natl. Acad. Sci. U.S.A.*

139. Milov, A. D., Tsvetkov, Y. D., Formaggio, F., Crisma, M., Toniolo, C., and Raap, J. (2000) Self-Assembling properties of membrane-modifying peptides studied by PELDOR and CW-ESR spectroscopies, *J. Am. Chem. Soc. 122,* 3843-3848.

140. Lesser, D. R., Kurpiewski, M. R., and Jen-Jacobson, L. (1990) The energetic basis of specificity in the Eco RI endonuclease--DNA interaction, *Science 250,* 776-786.

141. Sapienza, P. J., Torre, C. A. d., IV, W. H. M., Jana, S. V., and Jen-Jacobson, L. (2005) Thermodynamic and Kinetic Basis for the Relaxed DNA Sequence Specificity of "Promiscuous" Mutant EcoRI Endonucleases, *Journal of Molecular Biology 348,* 307-324.

142. Hsu, M.-T., and Berg, P. (1978) Altering the specificity of restriction endonuclease: effect of replacing Mg^{2+} with Mn^{2+}, *Biochemistry 17*, 131-138.

143. Thielking, V., Alves, J., Fliess, A., Maass, G., and Pingoud, A. (1990) Accuracy of the EcoRI restriction endonuclease: binding and cleavage studies with oligodeoxynucleotide substrates containing degenerate recognition sequences, *Biochemistry 29*, 4682-4691.

144. Woodhead, J. L., Bhave, N., and Malcolm, A. D. B. (1981) Cation Dependence of Restriction Endonuclease EcoRI activity, *Eur. J. Biochem. 115*, 293-296.

145. Grigorescu, A., Horvath, M., Wilkosz, P., Chandrasekhar, K., and Rosenberg, J. (2004) *Restriction Endonucleases*, Springer-Verlag.

146. Kim, Y. C., Grable, J. C., Love, R., Greene, P. J., and Rosenberg, J. M. (1990) Refinement of Eco RI endonuclease crystal structure: a revised protein chain tracing, *Science 249*, 1307-1309.

147. Kurpiewski, M. R., Engler, L. E., Wozniak, L. A., Kobylanska, A., Koziolkiewicz, M., Stec, W. J., and Jen-Jacobson, L. (2004) Mechanisms of Coupling between DNA Recognition Specificity and Catalysis in EcoRI Endonuclease, *Structure 12*, 1775-1788.

148. Lu, J., Bender, C. J., McCracken, J., Peisach, J., Severns, J. C., and McMillin, D. R. (1992) Pulsed EPR studies of the type 2 copper binding site in the mercury derivative of laccase, *Biochemistry 31*, 6265-6272.

149. Jiang, F., McCracken, J., and Peisach, J. (1990) Nuclear quadrupole interactions in copper(II)-diethylenetriamine-substituted imidazole complexes and in copper(II) proteins, *J. Am. Chem. Soc. 112*, 9035-9044.

150. Huffman, D. L., Huyett, J., Outten, F. W., Doan, P. E., Finney, L. A., Hoffman, B. M., and O'Halloran, T. V. (2002) Spectroscopy of Cu(II)-PcoC and the Multicopper Oxidase Function of PcoA, Two Essential Components of Escherichia coli pco Copper Resistance Operon, *Biochemistry 41*, 10046 - 10055.

151. Mims, W. B., and Peisach, J. (1978) The nuclear modulation effect in electron spin echoes for complexes of Cu^{2+} and imidazole with ^{14}N and ^{15}N, *J. Chem Phys. 69*, 4921-4930.

152. Flanagan, H. L., and Singel, D. J. (1987) Analysis of ^{14}N ESEEM patterns of randomly oriented solids, *J. Chem Phys. 87*, 5606-5616.